Eindhoven University of Technology

MASTER

Experimental investigation of CO_2 Two-Phase heat transfer characteristics and prediction of CO_2 dryout vapor quality

Özdemir, Merve Zeynep

Award date:
2012

Link to publication

Eindhoven, August 2012

Experimental Investigation Of

CO$_2$ Two-Phase Heat Transfer Characteristics

And Prediction Of CO$_2$ Dryout Vapor Quality

Merve Zeynep Ozdemir

Report Number WET 2012.08.

Supervisors:

Graduation Professor TU/e : prof. dr. ir. A. A. van Steenhoven
Graduation Supervisor TU/e : dr.ir. A.J.H. Frijns
ASML Research: ir. Sjoerd Donders
National Aerospace Laboratory (NLR) : dr.ir. Henk Jan van Gerner

ACKNOWLEDGEMENTS

I would like to express my sincere appreciation to Professor Anton van Steenhoven and my supervisor Dr. Ir. Arjan Frijns for their guidance and direction during all phases of my master thesis project.

I am thankful to my supervisors Sjoerd Donders from ASML Research and Henk Jan van Gerner from NLR (National Aerospace Laboratory of the Netherlands) for their support and encouragement throughout my study. Thanks to them, I have gained a solid background related to the practical issues of experimental study and learned how to manage the time; how to approach to urgent problems; how to interpret the outcomes of the work in simple but in an elegant way. Their productive collaboration shaped the results of this thesis.

I would like to thank to all ASML Research members that have been involved in this project. Especially, Niek Roset for his assistance and patience with my frequent questions related to the test set-up; Martijn Verdonck for his help related to channel drawings and roughness measurements in the cleanroom; Victoria Voronina helping out with the flow visualization study and sharing the critics of measurement results; Rob de Kater and Slawek Leszczynski for their quick responses and repairs during the brazing failure of the channels; Sander Tromp for spending time with tricky Matlab problems and offering inspiration and good humor.

I owe more than I can ever manage to pay back to my family for their love, understanding and confidence. My graduate work would not have been possible without their support and I am forever grateful to them.

" I often say that when you can measure what you are speaking about, and express it in numbers, you know something about it; but when you cannot measure it, when you cannot express it in numbers, your knowledge is a meagre and unsatisfactory kind; it may be the beginning of knowledge, but you have scarcely in your thoughts advanced to the state of Science, whatever the matter may be."

Lord Kelvin (1824-1907)

This page is intentionally left blank.

ABSTRACT

High power demands and miniaturization of electronic devices require effective heat removal from the power electronics. Therefore, it is essential to develop new high heat flux cooling technologies in order to meet challenging heat dissipation requirements. One possible solution is to make use of the high heat transfer performance of two-phase heat transfer with a suitable refrigerant. Preliminary analyses show that choosing CO_2 as a refrigerant has more advantage over other refrigerants but also presents a challenge in terms of predicting its two-phase heat transfer characteristics.

In the present study, the cooling performance of CO_2 is investigated experimentally as a function of heat flux, mass flux, channel diameter and vapor quality. The test database includes around 2100 heat transfer coefficient measurement points at the following test conditions: hydraulic diameters from 0.5 mm to 1.5 mm; mass fluxes from 200 to 1700 kg/m^{2}s, heat fluxes from 40 to 200 kW/m^{2}K and a saturation temperature of 22 °C. Dryout vapor quality, the maximum vapor quality that can be reached before the dramatic drop of two-phase heat transfer coefficient, is estimated at each test condition. Then, available two-phase heat transfer coefficient and dryout vapor quality correlations are applied to the test results and statistical analyses have been performed. The experimental results show that CO_2 two-phase heat transfer coefficient is dominated by nucleate boiling heat transfer mechanism and strongly depends on the heat flux before dryout vapor quality at the test conditions. Furthermore, a new dryout quality prediction correlation is developed based on the results of statistical analysis. In addition, two-phase CO_2 flow patterns have been studied with flow visualization at 45 adiabatic test conditions since CO_2 flow boiling heat transfer mechanisms are closely related to two-phase flow patterns. The flow visualization results have been compared to CO_2 two-phase flow pattern map of Cheng et al. [L. Cheng, G. Ribatski, J.R. Thome] and a new intermittent to annular flow transition line is found on the CO_2 flow pattern map.

The outcomes of this thesis will be used for the design of future micro- evaporator in the actuator cooling system of ASML Next Generation Lithography Machines.

Keywords: CO_2 two-phase flow, micro-scale evaporation, dryout prediction, pressure drop, flow patterns

This page is intentionally left blank.

NOMENCLATURE

Symbol	Description	Unit
A	Cross sectional area	m^2
Bo	Boiling number	
Bd	Bond number	
c_p	Specific heat	J/kgK
D	Diameter	m
E	Convective enhancement factor	
ϵ	Void fraction	
f	Friction factor	
Fr	Froude number	
g	Gravity acceleration	m/s^2
G	Mass flux	kg/m^2s
H	Height of the microchannel	m
h	Heat transfer coefficient	W/m^2K
h_{lv}	Heat of evaporation	J/kg
j	Superficial Velocity	m/s
k	Thermal conductivity	W/mK
L_h	Length of the heated test channel	m
$\dot{m}$	Mass flow rate	kg/s
M	Molecular weight (of CO_2)	kg/mol
MAE	Mean absolute error	
MRE	Mean relative error	
Nu	Nusselt number	
P	Pressure	N/m^2
P_r	Reduced pressure	$P_{sat}/P_{critical}$
Pr	Prandtl number	

q	Heat flux	W/m^2
Q	Heating power	W
Q	Volumetric flow rate	m^3/s
Re	Reynolds number	
Ra	Rayleigh number	
R^2	Coefficient of determination	
S	Distance from thermistors to channel bottom wall	m
T	Temperature	K
U	Uncertainty	
We	Weber number	
W	Width of the microchannel	m
x	Vapor mass fraction	
z	Coordinate in the flow direction	

Greek Letters

α	Thermal diffusivity	m^{2}s
β	Thermal expansion coefficient	1/K
ε	Emissivity of the channel surface	
v	Kinematic viscosity	m^2/s
μ	Dynamic viscosity	N/m^{2}s
ρ	Density	Kg/m^3
Ψ	Barnett number	
θ	Angle	Radian
σ	Surface tension	N/m
σ	Stefan -Boltzmann constant	$5.67*10^{-8}$ W/m^{2}K^4
Δ	Change in associated property	

Subscripts

amb	Ambient
crit	Critical
di	Dryout inception
eq	Equivalent

f	Fluid
h	Hydraulic
H	Homogeneous
in	Inlet
l	Liquid
lo	Liquid phase flowing alone
ls	Superficial liquid phase
nb	Nucleate boiling
n	Interim number of thermistors
pred	Predicted
s	Superficial
strat	Stratified
surr	Surroundings
sat	Saturation
ts	Thermistor
tp	Two-phase
v	Vapour

This page is intentionally left blank.

TABLE OF CONTENTS

This page is intentionally left blank.

LIST OF FIGURES

1   INTRODUCTION

1.1   Background of CO$_2$ Flow Boiling in Microchannels

Carbon dioxide has been used as a refrigerant mainly in the electronic cooling, automotive and residential air conditioning, heat pump applications, marine systems and food industry for over 130 years [1]. It has gained a considerable attention as an alternative refrigerant to the conventional refrigerants due to its favorable thermophysical properties in terms of heat transfer, being no-flammable and non-toxic in terms of environmental and personal safety. CO$_2$ is freely available in nature with a zero ozone depletion potential which makes it safe, economical and cost effective natural refrigerant.

The usage of CO$_2$ in microchannel heat exchangers has been increased in recent years due to the advantageous of microchannel evaporators such as having reduced size, higher efficiency and being capable of handling high operating pressures. Microchannel heat exchanger design requires the prediction of the heat transfer coefficients, pressure drop and dryout vapor quality under the conditions of interest. However, the heat transfer coefficients of CO$_2$ two-phase flow in small channels cannot be properly predicted using existing correlations. One of the reasons of this issue is that the available two-phase heat transfer correlations are limited within their database ranges. Once they are extended to different operating conditions, deviations from the reality become more pronounced especially in microscale. Secondly, the thermophysical and transport properties of CO$_2$ are quite different from the other conventional refrigerants at the same evaporation temperatures. High vapor density, low surface tension, low vapor viscosity and high reduced pressure of CO$_2$ drastically influence on its boiling characteristics that will be addressed in the further sections. For that reason, application of the general heat transfer prediction methods to CO$_2$ two-phase heat transfer results in the order of difference in magnitude and does not capture the heat transfer coefficient trends correctly. Therefore, heat transfer characteristics of CO$_2$ should be considered separately other than the conventional refrigerants.

One of the major challenges of the heat exchanger design is to predict the dryout vapor quality where the two-phase heat transfer coefficient drops drastically. Occurrence of dryout significantly lowers the performance of the heat exchangers. Moreover, evaporators must operate within safe working limits of temperature so that overheating of the wall of the channels and subsequent failure of the evaporator due to melting of the soldering can be avoided. Hence, selection of the operating conditions and the optimal design of the heat exchangers are required to avoid the dryout occurrence. From literature review, it can be found that the dryout of CO$_2$ flow boiling data at high temperatures and high heat fluxes is very limited. Therefore, dryout quality predictions do not provide accurate predictions at high saturation temperatures and wider range of heat flux and mass flux conditions.

1.2 ASML Application of CO_2 Flow Boiling

In lithography machines, there is a part called wafer stage which carries the silicon wafer through the system for measurement and the imaging of the chip patterns. An ASML dual wafer stage system carries two wafers through the system in parallel, one stage measures one wafer while the other carries another wafer that was measured earlier under the lens to image the patterns in a scanning motion. In Figure 1.1, a drawing of the TWINSCAN dual wafer stage is represented [2].
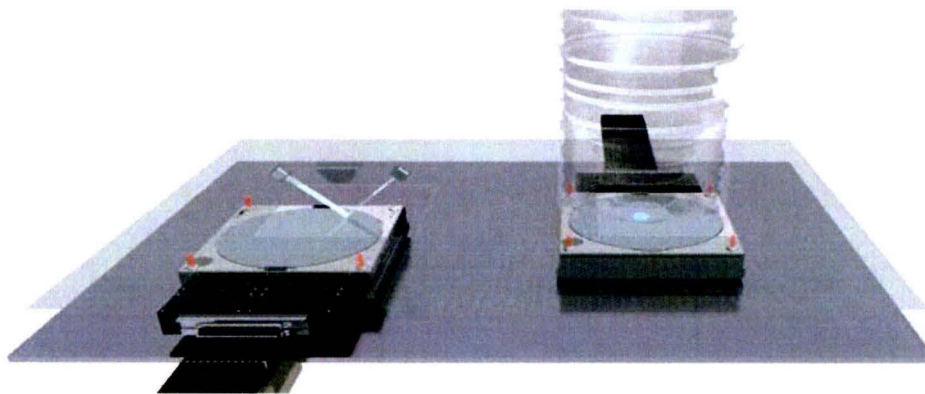
Figure 1.1 TWINSCAN Wafer Stage

In order to have a higher productivity, wafer stages are required to be capable of operating at higher speeds. This means more powerful actuators are needed. In general, an actuator coil contains numerous windings of a wire and a magnetic device. The magnetic device can include one or more permanent magnets. As an electric current is passed through the actuator coil, an electromagnetic field is established, which interacts with a magnetic field produced from the magnetic device to cause a force to be exerted on the actuator coil. This force causes the actuator coil to move. The movement of an actuator coil can be controlled by adjusting the electric current flowing through the actuator coil. In order to increase the force, the electric current must also be increased. However, as the current is increased, the operating temperature of the actuator coil also raises in the form of electrical energy dissipating as heat within the actuator coil. This heat dissipation adversely affects the performance of the coil. For that reason, heat removal is an important issue in terms of reducing the undesired effects on the actuator performance.

In the current actuators of ASML, heat removal is achieved with externally cooled single phase water. Heat is transferred from actuator coil to cooling plate via conduction and then heat is removed by

convection inside of the channels. Between cooling plate and actuators, there are several layers as shown in Figure 1.2. The potting materials are used to enhance mechanical strength, provide electrical insulation and adapt the thermal expansion differences between the coil and the cooling plate. Kapton is used for electrical insulation and glue attaches the cooling plate to the coil.
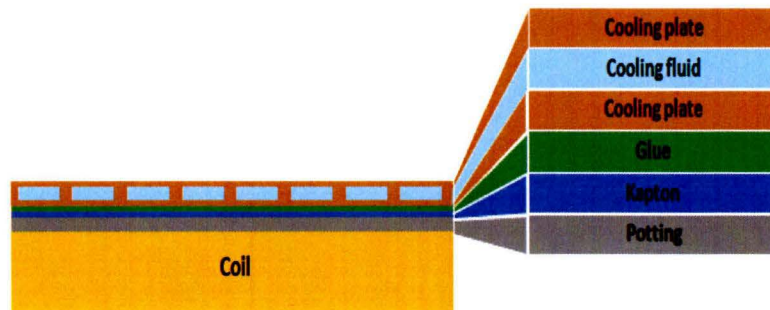
Figure 1.2 Schematic of Coil and Cooling Channels with Layers

In the Next Generation Wafer Stage, heat sources generate around 50 kW power. In the current water cooling system single phase mechanically pumped fluid loop is used as a continuous cooling system. However, a two-phase mechanically pumped fluid loop requires a lower mass fluid flow and gives a higher heat transfer coefficient. Therefore two-phase mechanically pumped fluid loop will be applied as a next generation wafer stage cooling system.

At the early stages of the project, the cooling fluid of Next Generation Wafer Stage is chosen such a way that minimum pressure drop and high heat transfer coefficient can be achieved among the available refrigerants. Geometry influence, high temperature stability and low mass flow rate are taken into account during the selection. Ammonia (R717), carbon dioxide (R744) and Di-Methyl Ether (DME) (R-E170) are considered to be final candidates. Although ammonia has low pressure drop and high typical heat transfer, it has the drawback of having pressure and temperature fluctuations in the parallel cooling channels and the leak of ammonia in the system can damage the entire machine. In addition, ammonia is a toxic gas under ambient conditions and releases of ammonia danger the human safety. DME is considered to be a low pressure (5.4 bar) alternative for ammonia and CO_2 in case high pressure components are not available. Despite the fact that CO_2 has relatively high mass flow and relatively high pressure (60 bar), it is chosen as the cooling fluid with the advantage of having high heat transfer coefficient and highest temperature stability, being non-toxic and non-flammable. The calculations and details of the cooling fluid decision can be found in the report of H.J. van Gerner (See Ref. [2]) The machine operate at 22°C in order to obtain the accurate imaging and positioning, therefore phase change of CO_2 takes place at 22°C. Due to size of the actuators that are desired to be cooled in the ASML machine, the cooling is achieved with small size channels with an estimated range from 0.5 to 1.5 mm hydraulic diameters.

 Preliminary test results of a small range of ASML applications showed that the heat transfer correlations differed with more than two orders of magnitude between the models and all models have different behaviors along the vapor mass fraction axis. The main reason of mismatch between those models and

ASML case is attributed to the fact that the model's ranges of applicability do not support range of ASML parameters. Therefore, it is first required to have the test results within a broad range of ASML parameters and investigate the CO_2 two-phase heat transfer characteristics within that range.

1.3   Thermophysical Properties of CO_2

Boiling heat transfer characteristics of CO_2 are related tightly with its thermophysical properties. This section focuses on the effects of CO_2 thermophysical properties on the heat transfer mechanism and comparison of those properties with the other common refrigerants such as R134a, R22, R410a, and R717.

CO_2 has higher reduced pressure than the other refrigerants at the same evaporation temperature since its critical temperature is 31.1 °C [3]. As a consequence, its properties such as surface tension, liquid to vapor density ratio, liquid viscosity and vapor thermal conductivity are significantly different than conventional refrigerants. For example, at the same temperature, the surface tension, the liquid viscosity and the density ratio of liquid to vapor of CO_2 are the smallest among other refrigerants such as R22, R134a, and R410A as seen in Figure 1.3-Figure 1.4 [3]. Its low surface tension makes easier the break-up of liquid film and enhances nucleate boiling requiring less superheat to initiate bubble formation. As the saturation temperature becomes higher, surface tension decreases more and nucleate boiling is enhanced more. The surface tension of the refrigerants decreases with temperature and becomes zero at the critical point.
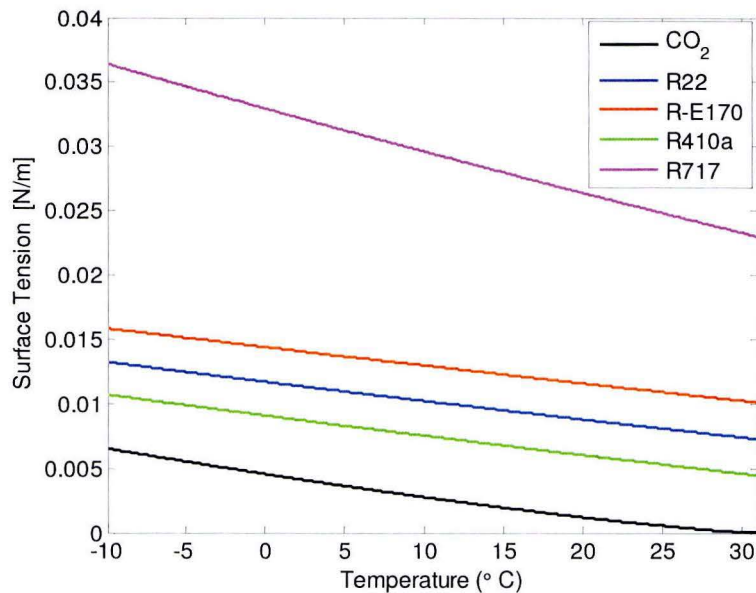
Figure 1.3 Variation of Surface Tension with Temperature for Different Refrigerants

4

Liquid to vapor density ratio is important for the flow pattern estimation thus the heat transfer coefficient. Smaller density ratio of liquid to vapor cause a smaller change in velocity and this results in lower two-phase Reynolds number for a certain mass flow rate during the boiling process. Since two-phase Reynolds number has an influence on flow pattern transitions, it can be said that liquid to vapor density ratio has a indirect effect on two-phase flow patterns. In addition, the distribution of the flow inside the tube is more homogeneous compared to other refrigerants at the same saturation temperature. Furthermore, liquid to vapor density ratio plays a role in some dryout prediction equations such that decrease in the density ratio of liquid to vapor yields earlier occurrence of dryout. Associated equations will be addressed in Table 7.1 of Chapter 7.
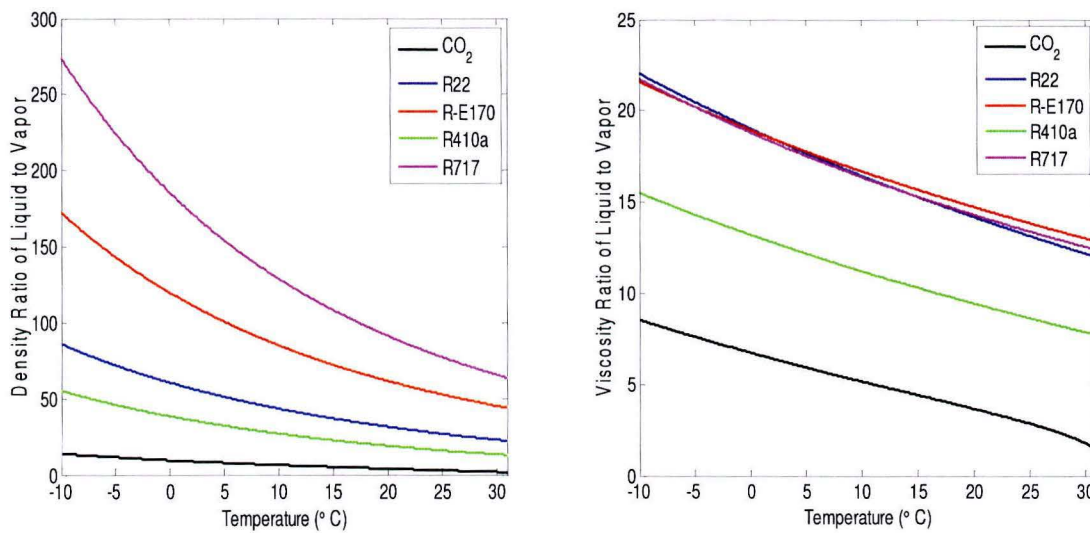
Figure 1.4 Variation of Liquid to Vapor Density Ratio and Liquid to Vapor Viscosity Ratio with Temperature for Different Refrigerants

Lower viscosity ratio of liquid to vapor leads to smaller pressure losses than other refrigerants and low liquid viscosity results in higher Reynolds number which helps to enhance the convective boiling contribution of CO_2 compared to other refrigerants at the same saturation temperature. Related equations can be seen in Table 6.1 of Chapter 6.

Some physical properties of CO_2 at 22°C that are found in NIST REFPROP [3] are listed below:

Table 1.1 Thermophysical Properties of CO_2 at 22 °C

P_{sat} [bar]	P_r	σ [N/m]	μ_l/μ_v	ρ_l/ρ_v	$c_{p,l}$ [J/kg K]	$c_{p,v}$ [J/kg K]	h_{lv} [J/kg]	k_l [W/mK]	k_v [W/mK]
59.82	0.81	0.00095	3.34	3.58	4793.9	5431.6	141260	0.0832	0.0372

The flow pattern map transitions numbers as explained in Chapter 5 mainly based on the non-dimensional numbers. Non-dimensional numbers such as Reynolds number, Weber number, etc.

correlate the main thermodynamic properties of CO_2 that are shown in Table 1.1. For that reason, the thermophysical properties of CO_2 will be addressed in the following chapters when the heat transfer and dryout behaviors and two-phase flow pattern transitions are explained.

All in all, the specific objectives of this thesis can be summarized as

- Estimation of the heat flux, mass flux and channel diameter parameters for ASML application,
- Measurement of the heat transfer coefficients and pressure drops within ASML operating conditions range,
- Evaluation of the heat transfer coefficient results and investigate the effects of mass flux, heat flux, channel diameter on CO_2 flow boiling behavior,
- Observing the flow patterns of CO_2 and relate them to CO_2 flow pattern map,
- Finding the dryout correlation for CO_2 flow boiling within the database range.

Those issues listed above can be found in detail within the following chapters. The outline of the thesis consists of a brief introduction, literature review of CO_2 dryout prediction, experimental test set-up, test results and analysis of flow visualization and heat transfer coefficients, a new dryout correlation development, conclusions and future work, respectively.

2 STATE OF THE ART OF CO_2 FLOW BOILING DRYOUT QUALITY PREDICTION

Dryout inception quality is an important parameter in the design of the evaporators since two-phase heat transfer coefficient drops dramatically when the dryout starts. In terms of physical mechanism, dryout condition represents the breaking of the continuous liquid contact with the heated surface in a flow channel from moderate to high vapor qualities. When the dryout starts, it follows the gradual decrease of liquid fraction due to evaporation or boiling of the liquid film. Dryout inception is controlled by heat flux, mass flux, saturation temperature and channel geometries. When a prediction correlation is developed, it is reasonable to use dimensionless numbers rather than to use these parameters directly. However, there is not a single general dryout prediction formula valid for CO_2 flow boiling. The available studies include limited databases under different test conditions. In this chapter, a literature review that includes CO_2 dryout inception correlations is presented and discussed.

2.1 CO_2 Dryout Quality Prediction by Hihara and Tanaka (2000)

Hihara and Tanaka [4] performed experiments on boiling heat transfer of CO_2 in a 1 mm horizontal stainless steel tube at an evaporating temperature of 15 °C and mass velocities from 360 to 1440 kg/m^2. The channels were electrically heated by direct current. They observed that the dryout vapor quality decreased with increasing the mass velocity. However, they did not discuss the dryout of CO_2 in detail and they did not propose any correlations.

2.2 CO_2 Dryout Quality Prediction by Yun and Kim (2003)

Yun and Kim [5] predicted critical quality for saturated flow boiling of CO_2 at 0, 5 and 10°C, heat flux between 7.2 and 48.1 kW/m^2 and mass flux of 500-3000 kg/m^{2}s. They used 0.98 mm and 2 mm horizontal tube diameters and heat is applied by direct current.

For their 2 mm data, they discovered an increase of the dryout vapor quality with increasing mass velocity after a certain value of mass flux (G), called transition mass velocity. Before transition mass velocity dryout quality decreases with increasing mass velocity and after transition mass velocity dryout vapor quality is inversely proportional to mass velocity. For their 0.98 mm channel, they only observed the increase of the dryout vapor quality with mass velocity. They attributed the increase of the dryout vapor quality with mass velocity to the intense deposition of liquid droplets onto the liquid film layer and dryout patch regions.

They developed a physical model to predict the critical vapor quality of CO_2. Two entrainment mechanisms, interface deformation and bubble bursting, were considered with the liquid film thickness

as the critical physical parameter. A liquid film thickness less than the critical liquid film thickness obtained according to the method of Fujita and Ueda [6], is the film thickness criterion for the onset of dryout. The variation of the liquid film flow along the heated tube is calculated by integrating the continuity equation, based on the entry conditions, a given rate of evaporation and analytical correlations for the entrainment and deposition of droplets. The dryout is then identified where the liquid film flow is zero. According to their results [5], this method is quite complex and critical qualities were poorly predicted due to the intense deposition of liquid droplets at relatively high mass fluxes.

2.3 CO_2 Dryout Quality Prediction by Pettersen et al. (2004)

Pettersen et al. [7] experimentally investigated the dryout of CO_2 in a hydraulic diameter of 0.79 mm. heat transfer and pressure drop measurements were conducted at temperatures 0-25 °C, mass flux of 190-570 kg/m^2s, and heat flux of 5-20 kW/m^2. The dryout inception is estimated using water dryout data scaled to CO_2 by the method of Ahmad [8], even though the range of the tube diameter, scaling parameter and tube inlet conditions were out of limit of applicability. The method of Ahmad is a fluid-to fluid scaling model based on dimensional analysis. The similarity criteria allows to convert operating conditions of CO_2 boiling to those of water vapor. The parameter ψ must have the same value for the two fluids:

$$\psi = \frac{GD}{\mu_l}\left(\sqrt{\frac{Y}{\rho_l}\frac{\mu_l}{D}}\right)^{2/3}$$

(2.1)

Where

$$Y = \left|\frac{\partial(\rho_l/\rho_g)}{\partial p}\right|_{\text{sat}}$$

(2.2)

Ψ is called Barnett number. Property data for water should be evaluated at a saturation pressure giving the same density ratio as for the fluid concerned, in this case CO_2, and the heat flux need to be scaled so that the Boiling number is the same for both fluids.

$$\text{Bo} = \frac{q}{h_{lv}G}$$

(2.3)

After scaling of the Barnett number and Boiling number, the correlation given by Levitan and Lantsman [9] is used for water dryout predictions.

$$x_{\text{critical}} = \left[0.24 + 1.57\left(\frac{p_{\text{sat}}}{98}\right) - 2.04\left(\frac{p_{\text{sat}}}{98}\right)^2 + 0.68\left(\frac{p_{\text{sat}}}{98}\right)^3\right]\left(\frac{G}{1000}\right)^{-0.5}$$

(2.4)

Once the equivalent pressure and mass velocity of water vapor is replaced with CO_2 equivalent pressure and mass velocity, CO_2 critical vapor quality is obtained.

This procedure can be summarized as follows:

- The density ratio between the liquid and vapor phase of CO_2 in the saturated state ρ_l/ρ_v is calculated.

- Then the saturation pressure of water that corresponds to $\left(\frac{\rho_l}{\rho_v}\right)_{water} = \left(\frac{\rho_l}{\rho_v}\right)_{CO_2}$ is found. $\left(\frac{\rho_l}{\rho_v}\right)_{CO_2}$ can be obtained from a third order or higher polynomial relationship between saturation pressure and liquid to vapor density ratio.

- The equivalent thermophysical properties of water vapor at the saturation pressure are obtained.

- The equivalent mass velocity of water vapor is calculated from $\psi_{CO_2} = \psi_{water}$

- The equivalent heat flux of water vapor is calculated from $Bo_{CO_2} = Bo_{water}$

- Equivalent pressure and mass velocity of water vapor is replaced in Equation 2.4 to find the critical vapor quality.

2.4 CO$_2$ Dryout Quality Prediction by Yoon et al. (2004)

Yoon et al. [10] obtained an empirical correlation to predict the dryout vapor quality by fitting their experimental results with dimensionless numbers. Their experiments were conducted in a stainless steel tube with the inner diameter of 7.53 mm at saturation temperatures of -4 to 20 °C, heat fluxes of 12 to 20 kW/m^2 and mass fluxes of 200 to 530 kg/m^{2}s.

The original correlation given in the paper of them [10] was later on corrected by the author [11]. It is found that the mistyped formulation is used by some researchers without knowing the correct form. However, the mistyping of the dryout prediction formula results in large differences when evaluating the experimental data. The corrected version is given by:

$$x_{dryout} = 0.0012 Re_{lo}^{2.79} (1000 Bo)^{0.06} Bd^{-4.76} \tag{2.5}$$

Reynolds number is calculated assuming all flow as a liquid flow and given as:

$$Re_{lo} = \frac{G D_h}{\mu_l} \tag{2.6}$$

$$Bd = \frac{(\rho_L - \rho_v) g D_h^2}{\sigma} \tag{2.7}$$

The mass flux, heat flux and saturation temperature are considered to determine the critical quality at the top of the tube. Instead of using heat flux, mass flux and saturation pressure in the correlation, non-dimensional numbers of Reynolds number, Boiling and Bond numbers are used to represent those parameters. Reynolds number includes the effect of mass flux, boiling number reflects the effect of heat

9

flux and Bond number reflects the effect of surface tension contribution. According to Yoon et al. [10], the influence of saturation temperature is substantially included in the above dimensionless numbers since thermophysical properties such as viscosity and surface tension are strongly dependent on the saturation temperature.

2.5 CO_2 Dryout Quality Prediction by Jeong and Park (2007)

Jeong and Park [12] studied evaporative heat transfer of CO_2 in a smooth horizontal multichannel microtube with a diameter of 0.8 mm. The channels are heated electrically by direct current. The tested heat flux is between 12-18 kW/m^2. They did the experiments at 5 °C and 10 °C saturation temperatures and for mass velocities varying from 400 to 800 $kg/m^2 s$. They correlated the dryout vapor quality based on Yoon et al.`s [11] formulation for CO_2 flow in macrochannels. They observed the decrease of dryout with increasing mass velocity. The correlation is given as

$$x_{\text{dryout}} = 6.2 \text{Re}_{\text{lo}}^{-0.5} \text{Bo}^{-0.2} \text{Bd}^{-0.45}$$

(2.8)

They observed that the dryout vapor quality decreases when the mass velocity increases.

2.6 CO_2 Dryout Quality Prediction by Tang et al. (2008)

Tang et al. [13] investigated the flow boiling of CO_2 at saturation temperatures of 1-15 °C, mass fluxes of 100-600 $kg/m^2 s$ and the heat fluxes of 1.67-8.33 kW/m^2. They tested 0.6 m long extruded aluminum tube with 8 flow channels with 1.7 mm inner diameter with 0.16 mm micro-fins.

They used the same method of Yoon et al. [10] to predict the dryout quality. However, they found out that critical vapor quality depends also on the liquid/vapor density and viscosity ratio within their experimental range. They proposed the following equation by non-linear fitting:

$$x_{\text{dryout}} = 1.297 \text{Re}_{\text{l}}^{-0.242} \text{Bo}^{-0.107} \text{Bd}^{0.00095} \left(\frac{\rho_v}{\rho_l}\right)^{0.000090} \left(\frac{\mu_l}{\mu_v}\right)^{1.122}$$

(2.9)

2.7 CO_2 Dryout Quality Prediction by Cheng et al. (2008)

Cheng et al. [14] provided following dryout prediction formulation for CO_2

$$x_{di} = 0.58\exp\left[0.52 - 0.236We_v^{0.17}Fr_{v,Mori}^{0.17}\left(\frac{\rho_v}{\rho_l}\right)^{0.25}\left(\frac{q}{q_{crit}}\right)^{0.27}\right]$$ (2.10)

The vapor Weber number (We_v) and the vapor Froude number ($Fr_{v,Mori}$) defined by Mori et al. [15] are calculated as

$$We_v = \frac{G^2 D_{eq}}{\rho_v \sigma}$$ (2.11)

$$Fr_{v,Mori} = \frac{G^2}{\rho_v(\rho_l - \rho_v)gD_{eq}}$$ (2.12)

and the critical heat flux q_{crit} is calculated with the Kutateladze [16] correlation as

$$q_{crit} = 0.131\rho_v^{0.5}h_{lv}[g\sigma(\rho_l - \rho_v)]^{0.25}$$ (2.13)

The equivalent diameter is given as:

$$D_{eq} = \sqrt{\frac{4A}{\pi}}$$ (2.14)

This equation is also used when the flow pattern map is being developed in Chapter 5. The validity range of this equation is given as tube diameters from 0.6 to 10 mm, mass velocities from 50 to 1500 kg/m²s, heat fluxes from 1.8 to 46 kW/m² and saturation temperatures from -28 to 25 °C (reduced pressures from 0.21 to 0.87).

2.8 CO_2 Dryout Quality Prediction by Ducoulombier et al. (2011)

Ducoulombier et al. [17] studied the flow boiling of CO_2 in a single stainless steel tube microchannel with an inner diameter of 0.529 mm for three temperatures (-10, -5 and 0 °C), with the mass fluxes from 200 to 1200 kg/m²s and the heat flux varying from 10 to 30 kW/m². Their investigation covered the qualities from zero to the dryout inception quality. They observed that depending on the heat flux and saturation temperature, two opposite trends are seen such that either dryout inception quality diminishes as the mass flux increases or dryout inception quality increases with the mass flux. They used Cheng et al.'s

[14] correlation for the first scenario where the drop of the dryout inception quality is seen as the mass flux increases. This behavior is observed at a temperature of 0 °C and heat flux of 30 kW/m^2. They used the following correlation depending on the boiling number and the reduced pressure by fitting the experimental data:

$$x_{di} = 1 - 338\text{Bo}^{0.703} P_r^{1.43} \tag{2.15}$$

This trend is observed at low temperature of -10 °C or minimal heat flux of 10 kW/ m^2. The summary of the results are shown in Figure 2.1
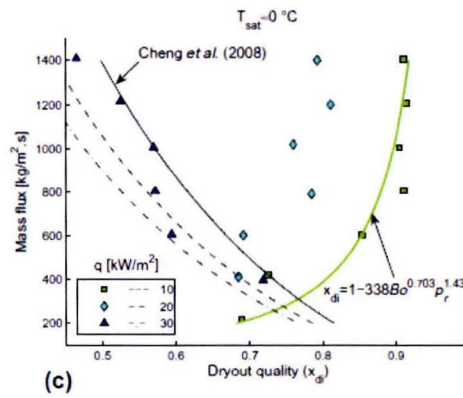
Figure 2.1 Influence of the mass flux on the dryout inception quality for various heat fluxes at T$_{sat}$=0°C

2.9   CO$_2$ Dryout Quality Prediction by Mastrullo et al. (2012)

Mastrullo et al. [18] studied CO$_2$ flow annular to dryout transition in a horizontal tube of 6 mm, between the reduced pressured of 0.57 to 0.64, mass velocities between 150 and 500 kg/m^{2}s, and heat fluxes between the 5 and 20 kW/m^2. According to them, liquid Reynolds number and liquid only Weber number play an important role in the transitions from slug to intermittent and intermittent to annular transitions. In particular, liquid Reynolds number accounts for the inertia to dissipative forces ratio which can be considered a measure of liquid turbulence that can contribute to break up of the interface during intermittent flow; liquid only Weber number shows the inertia to surface tension ratio is related to the amplitude of the liquid waves which can block the passages of the vapor phase during slug flow [18]. They included the reduced pressure to account the effects of variation of saturation properties. All the equations are listed below:

$$\text{Re}_l = \frac{G(1-x)D_{eq}}{\mu_l} \tag{2.16}$$

$$We_{lo} = \frac{G^2 D_{eq}}{\rho_l \sigma} \tag{2.17}$$

$$P_r = \frac{P(T_{sat})}{P_c} \tag{2.18}$$

$$Re_{l,pred} = a_0 We_{lo}^{a_1} P_r^{a_2} \tag{2.19}$$

They introduced Boiling number in order to account for the heat flux effect and added Boiling number into the Equation 2.19.

$$Re_{l,pred} = c_0 Bo^{c_1} We_{lo}^{c_2} P_r^{c_3} \tag{2.20}$$

The Equation 2.16 is combined with the Equation 2.19 in order to explicitly see the dependency of the transition line on mass velocity and vapor quality. The result can be expressed as:

$$x_{pred} = 1 - \left(c_0 q^{c_1} G^{(2c_2-c_1-1)} D_{eq}^{(c_2-1)} \frac{\mu_l}{(h_{lv}^{c_1})(\rho_l \sigma)^{c_2}} P_r^{c_3} \right) \tag{2.21}$$

Then the regression coefficients and adjusted coefficients of determination, $\overline{R}^2$, are found and a statistical analysis is performed to evaluate the results. They also investigate the effect of reduced pressure by expressing the non dimensional term $\frac{\mu_l}{(h_{lv}^{c_1})(\rho_l \sigma)^{c_2}}$ as a function of the reduced pressure.

That dimensional group is well expressed by a second order polynomial regression such that:

$$\frac{\mu_l}{(h_{lv}^{c_1})(\rho_l \sigma)^{c_2}} = d_0 + d_1 P_r + d_2 P_r^2 \quad \forall P_r \in [P_{r,min} - P_{r,max}] \tag{2.22}$$

Then the Equation 2.21 can be written as

$$x_{pred} = 1 - \left(c_0 q^{c_1} G^{(2c_2-c_1-1)} D_{eq}^{(c_2-1)} (d_0 + d_1 P_r + d_2 P_r^2) P_r^{c_3} \right) \tag{2.23}$$

Those coefficients are given as 20.82, 0.273, 1.252, -0.721 for c_0, c_1, c_2, c_3, respectively [18].

In conclusion, three approaches are presented in literature in the absence of general correlations:

- Similarity criteria based on empirical data for the dryout of water which leads to values for non-water fluids.
- Dryout phenomenological models through the solving of governing equations of two-phase annular flow with entrainment, deposition and vaporization.
- Development of a correlation for the critical vapor fraction from experimental data based on operating conditions.

These correlations are used to predict the dryout quality at the test conditions and they are discussed in Chapter 7.

This page is intentionally left blank.

3 EXPERIMENTAL SET-UP AND METHODOLOGY

3.1 Experimental Set-Up

Two-phase heat transfer coefficients were determined with a variation of mass, flux, heat flux, hydraulic diameter at 22 °C saturation temperature. The experimental apparatus allows measuring simultaneously the local heat transfer coefficients and pressure gradients during flow boiling. Schematic diagram of the experimental set-up is shown in Figure 3.1 . The refrigerant loop consists of a gear pump, a preheater, a brazed plate evaporator and a tube in tube condenser. Before starting the measurements, preliminary tests have been lead to check the calibration of the test set-up. First of all, all the sensors used for experimental tests have been calibrated. All the samples are pressure tested due to safety reasons after they are brazed and bolted. They could stand 140 bars pressure tests and found to be safe to install into the set-up. The entire mechanically pumped fluid loop is enclosed in a plexiglas box. Insulation is added to pipings, evaporator and preheater to minimize the heat flow rate dispersed to surroundings.
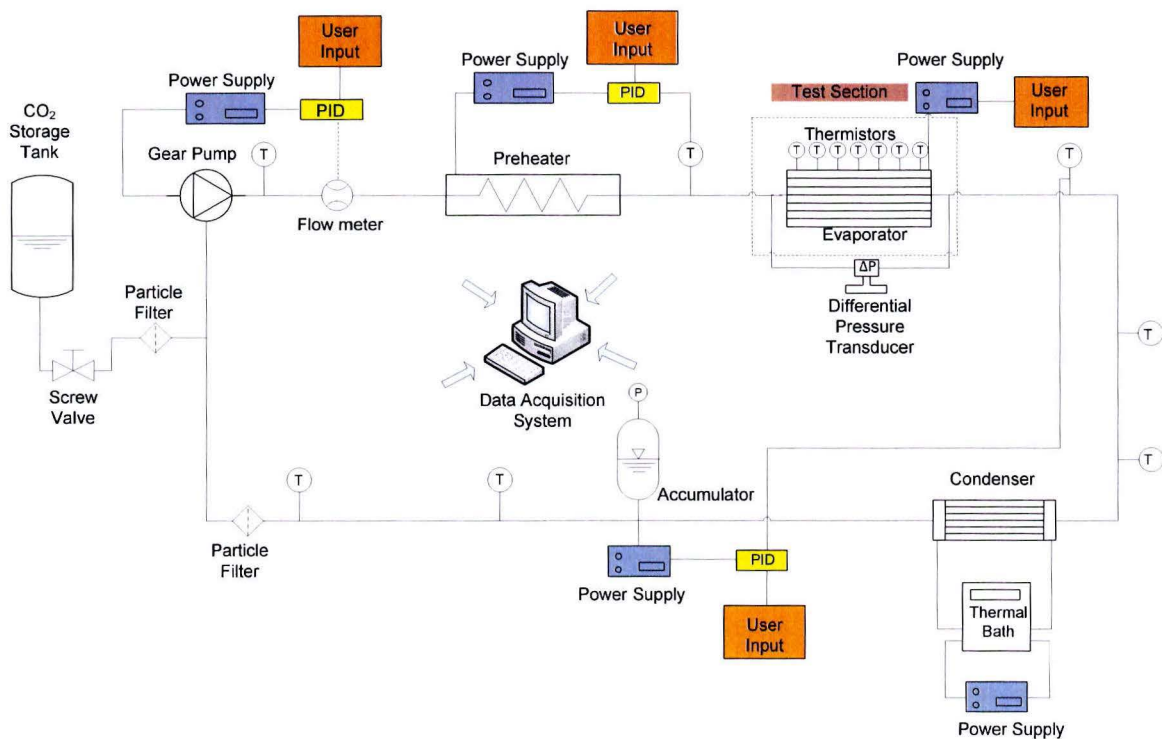
Figure 3.1 Schematic Diagram of the Test Set-up

First, the test loop is to be filled with correct amount of CO_2. Once the system is filled, the liquid CO_2 firstly flows through pump. The speed of the pump is determined by a user set point mass flow rate input. The refrigerant mass flow rate is measured by a Bronkhorst Cori-flow type flow meter that is

inserted downstream of the pump. A control loop is included in order to control the mass flow rate. The accuracy of the flow meter is ±0.2 % of the range of scale. After the flow meter, the fluid flows through the preheater. The subcooled liquid CO_2 is preheated to slightly lower temperature than 22 °C (mostly 21.5 °C) to prevent early evaporation before the entrance of test section, or partly evaporated to a certain qualities depending on the desired operating conditions. The preheater brings the refrigerant to a desired vapor quality or saturation temperature by means of electrical Joule heating by a power supply with an accuracy of ±0.2% range of the scale. The required power is estimated from mass flow rate, inlet refrigerant temperature before preheater and inlet saturation temperature before evaporator, thermophysical properties of CO_2 and desired vapor quality before evaporator. After the prehater, saturated CO_2 or partly evaporated CO_2 passes through the evaporator and leaves as vapor phase or mostly up to 0.9 vapor quality. A cartridge heater that is capable of 200 Watts is used to induce Joule heating to the evaporator. The temperature and pressure at the exit of the evaporator are used to monitor the instant changes in the saturation conditions and to verify if the flow is in two-phase. The length of the heated region is chosen to be 100 mm to have the same size of the cartridge heater length to ensure uniform heating throughout the channel. The total length of the heated section is divided into 10 intervals with 10 mm separate distance to determine the qualities at the determined points. The drawings of the tested channels are attached to Section 10.6 of Appendix. A side picture of the test block geometry is shown in Figure 3.2. Although the tested channels are single channel geometries, a two-channels geometry is shown in Figure 3.2 due to lack of the availability of the single channel geometry since it was brazed with the top cover of the microchannels.
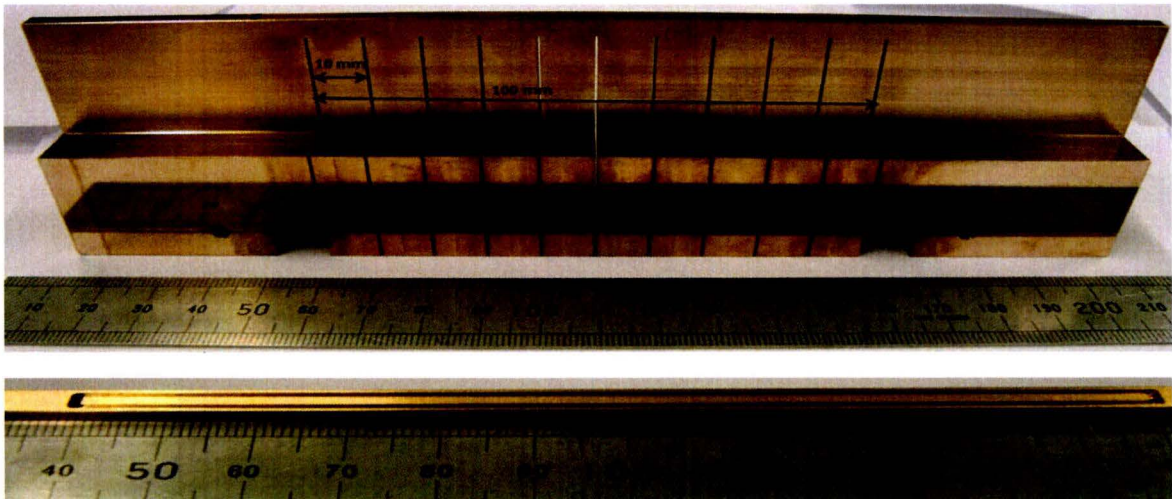
Figure 3.2 Tested Microchannel Geometry

The test section is instrumented with thermistors, embedded in the slots of the channel sample to measure the wall temperature of microchannels. NTC temperature sensors have an accuracy of ±0.04 K. They are calibrated by finding the offset and slope of the calibration equation. The junctions of the thermistors installed on the bottom part of the microchannels are electrically insulated by a very thin

Kapton tape. Once the wall temperatures are measured at the bottom side of the channel, the channel wall temperature is estimated with 1D heat conduction analysis. After the evaporator, the two-phase fluid passes through the condenser and turns into the liquid phase. Thermal bath of the water tank is set to a certain temperature to take the energy away from the two-phase CO_2. Exit temperature of the condenser comes out depending on the total mass flow rate, heat input to condenser and the temperature of the thermal bath. T type thermocouples with a calibrated accuracy of ±0.1K were used to measure refrigerant temperature at the several locations in the loop, for example before and after the preheater, at the inlet section of the evaporator and some locations at exit of the evaporator to monitor the two-phase CO_2 temperature.

The accumulator is used to adjust the saturation pressure in the evaporator by controlling saturation temperature. The saturation temperature is set to 22 °C with an accuracy of ±0.5 °C. When the pressure control is achieved so does the temperature control.

The condenser and the evaporator operate roughly at the same pressure. Two-phase pressure drop due to the evaporation of CO_2 is very low compared to driving pressure drop to pump CO_2 in the loop and this helps to avoid flow rate instabilities in the test loop. The absolute pressure of the CO_2 was determined by a pressure transducer with an uncertainty of ±0.25 % of the reading. Pressure drop along the test section is measured by differential pressure transducer with an accuracy of ±0.1% of the reading.

The measured parameters are acquired, analyzed and stored. National Instruments data acquisition system is used with the LabView software. The experimental data is obtained by real time measurement and analyzed using a data reduction program written in Matlab. All information about the test conditions and data are displayed on the monitor during the test. The system is allowed to come to steady state before any data is recorded. The data collection time takes around 2 minutes at each run. In summary, mainly five measuring parameters are determined that will be explained in Section 4:

> ➢ The outer wall temperatures of the test section and refrigerant fluid (CO_2) inlet and outlet temperatures at the test section,
> ➢ The mass flow rate of the refrigerant to calculate the mass flux through the test section,
> ➢ The power applied to test section to calculate the heat flux applied to the test section,
> ➢ The absolute pressure during tests to know the saturation temperature across the test section,
> ➢ The pressure drop to calculate the local saturation temperature at each measurement point.

This page is intentionally left blank.

4 DATA REDUCTION AND UNCERTAINTY ANALYSIS

All the test conditions of this study are shown in Table 4.1.The following subsections describe the thermal loss assessment, uncertainty analysis and data reduction methods used in the evaluation of two-phase heat transfer coefficients.

Table 4.1 Test Conditions

Hydraulic Channel Diameter (mm)	Heat Fluxes (kW/m^2)	Mass Fluxes (kg/m^2 s)
1.5 mm	20	200,300
	40	200,300,400,700,1000,1200
	75	300,400,500,600,700,900,1000,1200,1500,1700
	90	200,300,500,700,1000,1200,1500,1700
	130	300,500,700,900,1100,1200,1300,1500,1700
	148	400,500,700,900,1200,1500,1700
	200	600,700,1000,1200,1300,1500,1700,2000
0.5mm	80	1200
	100	500,700,1000,1200,1500,1700
	130	700,900,1100,1300,1500,1700
	150	500,700,900,1200,1500,1700
	185	800,1000,1200,1300,1500,1700
	225	1000,1200,1500,1700
	260	1200,1500,1700
	365	1500,1700

Before measuring the two-phase heat transfer coefficients, thermal conductivity of the copper is estimated since the channel sample is not purely made of copper. The conductivity tests are done such a way that several Joule powers are applied to channel block and temperature at certain locations are measured after steady state condition is reached. The net heat flux is estimated by subtracting the heat losses from applied power and then dividing the net heat power to heat flux area. The heat flux area is

the cross sectional area of upper side of the test block. Heat loss estimations can be found in Section 4.1.

$$q_{\text{net}} = \frac{Q - Q_{\text{loss}}}{A}$$
(4.1)

Conductivity is estimated from Fourier`s law of heat conduction

$$k = \frac{q_{\text{net}}\Delta x}{\Delta T}$$
(4.2)

Where Δx is the distance between temperature measurement locations at the middle of the test block and ΔT is the temperature difference of thermistor locations. The schematic of conductivity measurement section is given in Figure 4.1. The detailed dimensions can be found in Section 10.6 of Appendix.
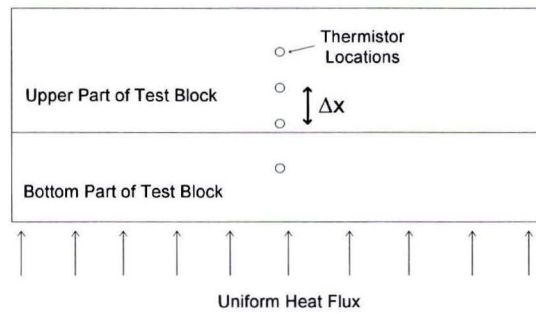
Figure 4.1 Schematic of Conductivity Measurement Section

Measurement summary of conductivity tests is shown in Table 4.2. The conductivity value is taken as 177 W/mK after these conductivity measurement tests.

Table 4.2 Thermal Conductivity Measurement Results

Net Heat Flux to The Measurement Section (kW/m^2)	Measured Thermal Conductivity (W/m^{2}K)
85.15	178.69
118.61	176.11
135.22	175.76

Channel heat flux takes into account the three sides of channel walls which is also validated by 2D finite element simulations. Actually, the heat flux distribution around the microchannels is not perfectly uniform due to channel geometry and one sided heating applied through the base of the channels.

20

Therefore, heat flux distribution is simulated for constant base heat flux. Comsol is used as a FEM tool. Since wall heat flux distribution is also heat transfer coefficient dependent, it is not constant along the channels walls. Total heat flux distribution of 100 kW/m^2 inside 0.5 mm square channel is performed to show non-uniform distribution visually. For initialization, a constant wall heat transfer coefficient is chosen from the experimental results of this study. Two-phase heat transfer coefficient of 90 kW/m^{2}K is estimated from experiments for the case of 100 kW/m^2 heat flux and 1200 kg/m^{2}s mass flux condition in 0.5 mm square channel, which can be seen in Figure 6.11. The boundary condition at the outer and inner channel walls are taken as isolated channel boundary and convection boundary condition, respectively. The drawing of the boundary conditions is given Figure 4.2. Once first results are obtained from Comsol, a second iteration is performed to obtain the heat flux distribution as realistic as possible. The convective heat transfer coefficient is obtained from first analysis result is taken as input for the second iteration. The heat flux is applied from the bottom side of the square channel. 1062 mesh elements are used and 2344 degree of freedoms are solved during the computation. The result of heat flux distribution is shown in Figure 4.3. It is clear that heat flux is concentrated on the bottom and side channel walls and the amount of heat flux reaching the top surface is low compared to the side and bottom heat flux distributions. Therefore, effective heat transfer area corresponds to three sides of square channel along the length of the single channel. Details of the analysis are given in Section 10.8 of Appendix.
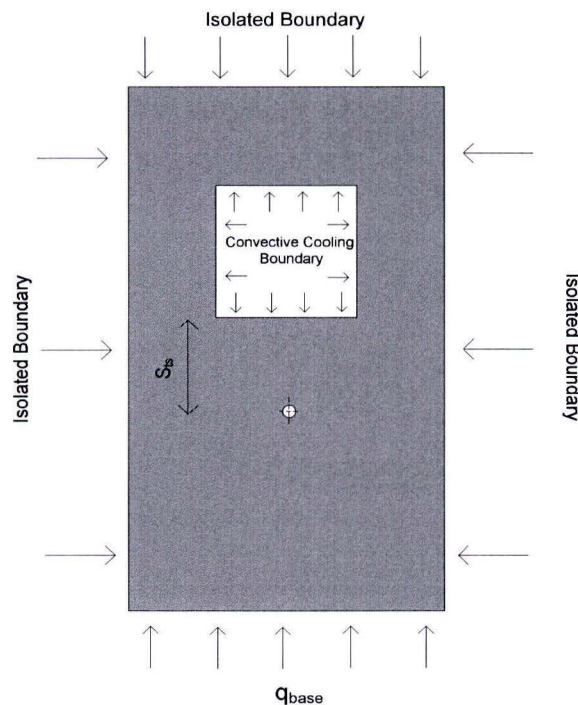
Figure 4.2 Boundary Conditions at Upper Part of Block Geometry for 2D Heat Flux Distribution

Surface: Total heat flux magnitude (kW/m^2)
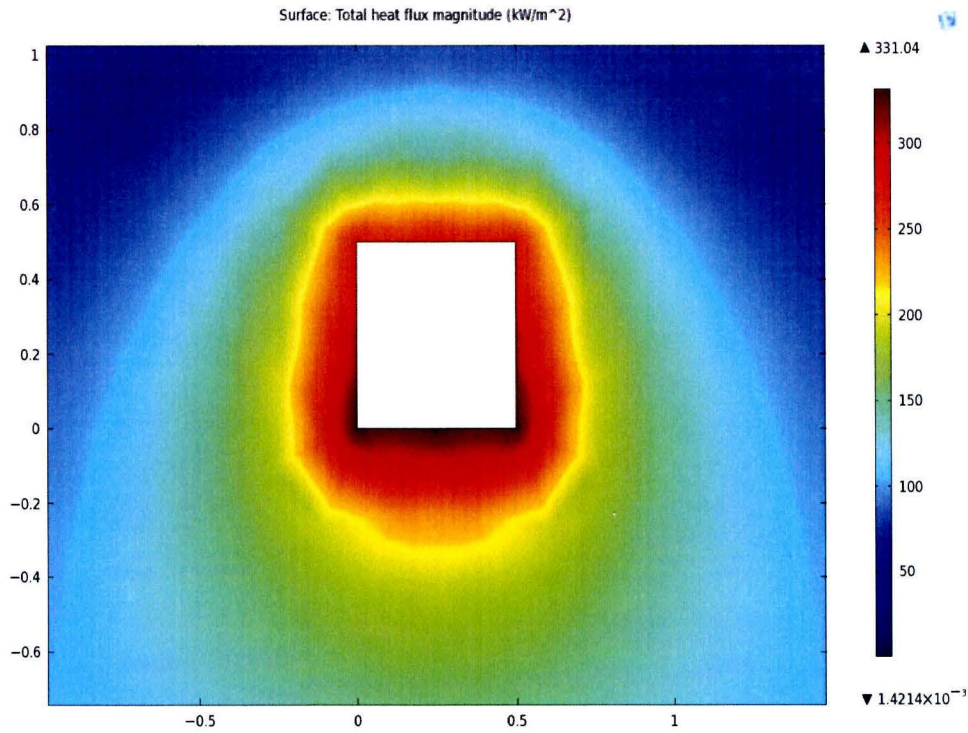
Figure 4.3 2D Heat Flux Distribution around The Microchannel Walls

The channel wall heat flux is calculated by taking into account the heat losses to outside environment. Heat loss estimation can be found in Section 4.1. The channel heat flux is given as

$$q_{wall} = \frac{Q - Q_{loss}}{A_{wall}} = \frac{V * I - Q_{loss}}{W + 2 * H} \tag{4.3}$$

The experimental heat transfer coefficient is determined by the ratio of the heat flux to the difference between the wall and the saturation temperature:

$$h = \frac{q_{wall}}{(T_{wall} - T_{sat})} \tag{4.4}$$

The wall temperature, T_{wall}, is calculated by 1D heat conduction equation from measured outer temperatures at the thermistor locations. T_{wall} is given as

$$T_{wall} = T_{ts} - \frac{q_{base}S_{ts}}{k} \tag{4.5}$$

where S_{ts} is the distance between thermistor location and channel wall, k is the measured thermal conductivity of test block and q_{base} is the heat flux on the surface area on the upper part of the channel where the thermistors are located. The distance S_{ts} is shown in Figure 4.2.

Saturation temperature (T_{sat}) is calculated from the measured evaporation pressure of CO_2. However, saturation temperature along the channel is not constant due to pressure drop of the CO_2 during the evaporation. When a heat flux is applied to the test section, the measured pressure drop is the sum of

22

the frictional and acceleration pressure drop for the horizontal microchannel. Total pressure drop measured between the inlet and exit of the channel is corrected for the extra tubings. That pressure drops in the tubing are estimated by two-phase Muller-Steinhagen and Heck pressure drop correlation [19]. However, it is still under-investigation to choose the best two-phase pressure drop model for predicting two-phase CO_2 pressure drops. For that reason, the accuracy of the tubing pressure drop estimation can be different if any other model has been used. But those differences can be encountered as minor errors since two-phase pressure drops in the tubings are small.

During the post processing of the experimental data, the total pressure drop is converted to corresponding saturation temperature drop at the each thermistor locations with an assumption of linear pressure drop between inlet and outlet of the channel. Then, the local saturation temperatures are taken as saturation temperature (T_{sat}) value. It is seen that the pressure drop can be up to 1 bar especially at high mass flow rates and early dryout conditions. This causes a significant change in the heat transfer coefficient value at those conditions due to reduction in the temperature difference between wall temperature and saturation temperature. Therefore, it is very important to check the pressure drop values at each experimental condition. Generally, pressure drops are around 0.5 -0.6 bars at the highest mass fluxes. Some experimental data can be found in Section 10.2.4 of Appendix.

Mass velocity (G) is defined as the mass flow rate ($\dot{m}$) per flow area (A), i.e., with respect to the total cross-sectional area of the channels.

$$G = \frac{\dot{m}}{A} \tag{4.6}$$

where A is the cross sectional area of the microchannel.

The vapor quality is defined as the ratio of the vapor mass flow rate to the total mass flow rate. Local vapor quality is calculated from an energy balance between the inlet of the preheater and the measured location. The energy balance equation is given in Equation 4.7 and derived vapor quality equation is given in Equation 4.8.

$$Q = \dot{m}\, \overline{c_{p,l}}\left(T_{sat}\left(p(z)\right) - T_{in}\right)\frac{L_h}{z} + \dot{m}\, h_{lv} x(z)\frac{L_h}{z} \tag{4.7}$$

$$x(z) = \frac{1}{h_{lv}}\left(\frac{z}{L_h}\frac{Q}{\dot{m}} - \overline{c_{p,l}}\left(T_{sat}\left(p(z)\right) - T_{in}\right)\right) \tag{4.8}$$

$$h_{lv} = h_{lv}\left(p(z)\right) \tag{4.9}$$

where z is the location along the microchannel, Q is the total power given to the test block by Joule heating, L_h is the total length of evaporator. The data reduction procedure has been implemented to a MATLAB script. All the thermo-physical and thermodynamic properties are obtained by NIST REFPROP [3]. Under uniform heat flux, wall temperatures should be independent of their lateral location across the width of the test section. The lateral uniformity of the wall temperatures is checked by arbitrarily inserting the thermistors in the sensor locations of channel block.

4.1 Heat Losses

Heat losses from the test sample are measured and also estimated theoretically. Although the test section is mostly insulated in order to minimize the losses, the top part of the test section is open to air and is not insulated in order not to disturb the temperature sensors. Heat losses are measured through a series of experiments in which there is no fluid in the test section. A certain amount of power is applied to test sample in order to bring it to a selected temperature. Then, the power required to maintain that temperature at the desired value is taken as the heat loss (Q_{loss}), which corresponds to the driving temperature difference between the test section and ambient air (ΔT_{amb}). The heat losses based on these tests produce a linear relationship between Q_{loss} and ΔT_{amb} as

$$Q_{loss} = C \times \Delta T_{amb} \qquad (4.10)$$

Where C is a constant dependent on the heat transfer coefficient and the heat transfer surface area that is in contact with ambient air. Heat losses at several temperature differences between ambient air and test block are shown in Figure 4.4 with a linear fitted line.
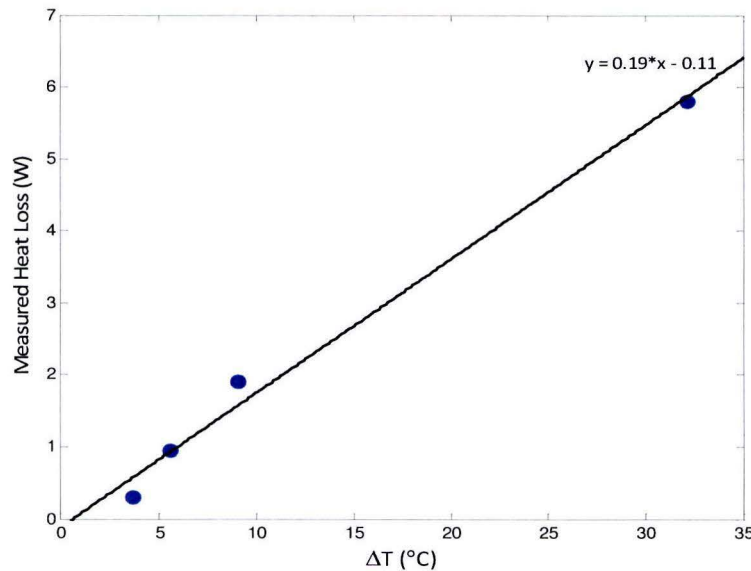
Figure 4.4 Measured Heat Losses at Several Temperature Differences

The estimated losses are extracted from the total power in the data reduction process of heat transfer calculations.

It is also possible to estimate heat losses the theoretically. There are three main sources of heat losses from the test section:

1) Heat losses by natural convection to the surrounding air

2) Heat loss due to conduction through the thermistor lead wires

3) Radiation heat losses to the ambient

The cross sectional area of the thermistors are very small (with a wire diameter of 100 μm), therefore heat loss due to conduction is neglected. The radiation heat loss and convection het losses are estimated as follows:

4.1.1   Convection Heat Loss Calculation

Natural convection losses are calculated by using the formula given by Incropera [20] for free convection on the vertical walls:

$$\mathrm{Nu_L} = 0.825 + \frac{0.387 * \mathrm{Ra_L}^{1/6}}{(1 + (0.492/\mathrm{Pr})^{9/16})^{8/27}} \tag{4.11}$$

Which is valid at $10^{-1} \leq \mathrm{Ra_L} \leq 10^{12}$. Rayleigh number is defined as

$$\mathrm{Ra_L} = \frac{g\beta(T_s - T_\infty)L^3}{\nu\alpha} \tag{4.12}$$

β is expansion coefficient ($1/T_{\mathrm{film}}$), ν is the kinematic viscosity, α is thermal diffusivity, T_∞ is quiescent temperature, T_s is the surface temperature. All fluid properties are calculated at film temperature, $T_{\mathrm{film}} = \frac{(T_s + T_\infty)}{2}$. Then, heat transfer coefficient is found from the relation

$$\mathrm{Nu_L} = \frac{hL}{k} \tag{4.13}$$

Where k is the thermal conductivity of the air at the given film temperature. The top part of the channel block is exposed to ambient air and not insulated to avoid the disturb thermistors on top part of the block. Therefore, heat loss due to free convection on the top part of the channel is estimated as convection heat loss.

4.1.2   Radiation Heat Loss Calculation

The heat transfer by radiation from the sample can be expressed by:

$$q = q"A = \varepsilon\sigma A(T_s{}^4 - T_{\mathrm{surr}}^4) \tag{4.14}$$

Where ε is the emissivity, σ is the Stefan-Boltzmann constant ($5.67*10^{-8}$ W/m^{2}K^4).

Theoretical heat loss calculation and measured heat losses agree with each other with a small difference and maximum heat loss from the test block is found to be less than 5% of the total power.

4.2   Uncertainty Analysis

The uncertainties of the experiments are analyzed with the RSS (Root-Sum-Square) method suggested by Moffat [21]. The average maximum uncertainty of the evaporation heat transfer coefficient is usually

found around ±15%, obtained by averaging uncertainties calculated under all test conditions. The derivations of uncertainties to calculate heat transfer coefficient uncertainty are shown below.

4.2.1 Principles of Uncertainty Analysis

When R is the function of independent variables $x_1, x_2, ..., x_n$ and $U_1, U_2, ..., U_n$ are defined as the uncertainty of each independent variable. The uncertainty of R can be calculated by Equation 4.15, at each test condition.

$$U_R = \left[\left(\frac{\partial R}{\partial x_1} U_1 \right)^2 + \left(\frac{\partial R}{\partial x_2} U_2 \right)^2 + \cdots + \left(\frac{\partial R}{\partial x_n} U_n \right)^2 \right]^{1/2} \qquad \textbf{(4.15)}$$

Each term of Equation 4.15 represents the contribution made by the uncertainty of one variable to the overall uncertainty in the result. This equation applies as long as

- Each of the measurement is independent
- Repeated observations of each measurement would display Gaussian distributions
- The uncertainty in each measurement is initially expressed with the same confidence (all uncertainty data are discussed based on a confidence level of 95%)

4.2.2 Fluid Property Regression

The refrigerant physical properties are calculated by applying linear regression to the third order polynomial of the temperature given by NIST REFPROP [3]. The general equation is

$$\phi = a_0 + a_1 T + a_2 T^2 + a_3 T^3 \qquad \textbf{(4.16)}$$

while the corresponding error is taken as follows:

$$U_\phi = a_1 + 2a_2 T + 3a_3 T^2 \qquad \textbf{(4.17)}$$

4.2.3 Uncertainty of Evaporating Temperature

The evaporating temperature (T_{sat}) is based on pressure measurement at the test section inlet and pressure difference across the test section. The uncertainty of the differential pressure measurement is negligible compared to the uncertainty in the absolute pressure measurement (See Table 4.4). Saturation temperature uncertainty is therefore calculated from the uncertainty in the absolute pressure measurement:

$$U_{T_{sat}} = \left(\frac{\partial T}{\partial p}\right)_{sat} U_{P_{sat}} \tag{4.18}$$

4.2.4 Uncertainty of the Refrigerant Mass Flux

The uncertainty in refrigerant mass flux is given by the mass flow meter uncertainty and the uncertainty in the microchannel average diameter, which are independent measurements. The mass flux equation is given by Equation 4.6. The resulting uncertainty in mass flux is calculated by Equation 4.20.

$$U_G = \left[\left(\frac{\partial G}{\partial \dot{m}} U_{\dot{m}}\right)^2 + \left(\frac{\partial G}{\partial A} U_A\right)^2\right]^{1/2} \tag{4.19}$$

$$U_G = \left[\left(\frac{1}{A} U_{\dot{m}}\right)^2 + \left(-\frac{\dot{m}}{A^2} U_A\right)^2\right]^{1/2} \tag{4.20}$$

4.2.5 Uncertainty of Wall Heat Flux

The uncertainty in wall heat flux depends on the measured voltage drop, current and wall heat flux area dimensions. The heat losses from the evaporator are estimated as mostly 3% of the total power and maximum uncertainty is 5% of the maximum heat power. Therefore, heat loss uncertainty part is neglected for simplicity during the derivation of the heat flux uncertainty.

The wall heat flux is calculated based on three sides of the square channels as explained previously and uncertainty associated with that heat flux is given as:

$$q_{\text{wall}} = \frac{V \times I}{3WH} \tag{4.21}$$

$$U_{q_{\text{wall}}} = \left[\left(\frac{\partial q_{\text{wall}}}{\partial \Delta V} U_{\Delta V}\right)^2 + \left(\frac{\partial q_{\text{wall}}}{\partial I} U_I\right)^2 + \left(\frac{\partial q_{\text{wall}}}{\partial W} U_W\right)^2 + \left(\frac{\partial q_{\text{wall}}}{\partial H} U_H\right)^2\right]^{1/2} \tag{4.22}$$

$$U_{q_{\text{wall}}} = \left[\left(\frac{I}{3WH} U_{\Delta V}\right)^2 + \left(\frac{\Delta V}{3WH} U_I\right)^2 + \left(-\frac{\Delta V * I}{3W^2 H} U_W\right)^2 + \left(-\frac{\Delta V * I}{3WH^2} U_H\right)^2\right]^{1/2} \tag{4.23}$$

4.2.6 Uncertainty of Vapor Quality at the Inlet of the Test Section

The vapor quality at the inlet of the test section is calculated based on enthalpy and saturation temperature of the fluid at the inlet of the test section.

$$x = x(h_{in}, T_{sat}) = \frac{h_{in} - h_f}{h_{lv}} \tag{4.24}$$

$$\frac{U_x}{x} = \sqrt{\left(\frac{\frac{1}{h_{lv}}U_{h_{in}}}{\frac{h_{in} - h_f}{h_{lv}}}\right)^2 + \left(\frac{-\frac{1}{h_{lv}}U_{h_f}}{\frac{h_{in} - h_f}{h_{lv}}}\right)^2 + \left(-\frac{1}{h_{lv}}U_{h_{lv}}\right)^2} \tag{4.25}$$

Equation 4.26, Equation 4.29 and Equation 4.30 show the uncertainties of enthalpy at the inlet of the test section, enthalpy of the refrigerant before preheater and enthalpy of heat of vaporization, respectively.

$$U_{h_{in}} = h_{in}\sqrt{\left(\frac{1}{h_f + \frac{q}{G}}\right)^2 (U_{h_f})^2 + \left(\frac{\frac{1}{G}}{h_f + \frac{q}{G}}\right)^2 U_q^2 + \left(\frac{-\frac{q}{G^2}}{h_f + \frac{q}{G}}\right)^2 U_G^2} \tag{4.26}$$

$$h_{in} = h_f + \frac{q}{G} \tag{4.27}$$

$$h_f = h(T_f) \tag{4.28}$$

$$U_{h_f} = \left(\frac{\partial h_f}{\partial T_f} U_{T_f}\right) \tag{4.29}$$

$$U_{h_{lv}} = \left(\frac{\partial h_{lv}}{\partial T_{sat}} U_{T_{sat}}\right) \tag{4.30}$$

Uncertainties in the U_{h_f}, $U_{h_{lv}}$ can be calculated by a polynomial regression as explained below:

$$h_f = a_0 + a_1 T_f + a_2 T_f^2 + a_3 T_f^3 \tag{4.31}$$

$$\frac{\partial h_f}{\partial T_f} = a_1 + 2a_2 T_f + 3a_3 T_f^2 \tag{4.32}$$

Similarly,

$$h_{lv} = a_0 + a_1 T_{sat} + a_2 T_{sat}^2 + a_3 T_{sat}^3 \tag{4.33}$$

$$\frac{\partial h_{lv}}{\partial T_{sat}} = a_1 + 2a_2 T_{sat} + 3a_3 T_{sat}^2 \tag{4.34}$$

The saturation temperatures are varied between 220 K and 300 K. Corresponding liquid enthalpy (h_f) and latent heat of evaporation (h_{lv}) are obtained by NIST REFPROP [3]. Those data range is fitted by a third order polynomial as explained above. Fluid temperature (T_f) should be taken in Kelvin.

$$h_f = -2607.8 + 30.083T_f - 0.1166T_f^2 + 0.0002T_f^3 \qquad (4.35)$$

$$\frac{\partial h_f}{\partial T_f} = 30.083 - 0.2332T_f + 0.0006T_f^2 \qquad (4.36)$$

$$h_{lv} = 6239.7 - 70.784T_{sat} + 0.2885T_{sat}^2 - 0.0004T_{sat}^3 \qquad (4.37)$$

$$\frac{\partial h_{lv}}{\partial T_{sat}} = -70.784 + 0.577T_{sat} - 0.0012T_{sat}^2 \qquad (4.38)$$

4.2.7 Uncertainty of the Vapor Quality Change between Inlet and Exit of the Evaporator

Vapor quality change between the inlet and exit of the evaporator is calculated subtracting the heat losses from the evaporator. It is given as:

$$\Delta x = \frac{Q_{evaporator}}{\dot{m}h_{lv}} \qquad (4.39)$$

The uncertainty of quality change along the evaporator test section is derived as:

$$U_{\Delta x} = \sqrt{\left(\frac{1}{\dot{m}h_{lv}}U_{Q_{evaporator}}\right)^2 + \left(\frac{-Q_{evaporator}}{h_{lv}\dot{m}^2}U_{\dot{m}}\right)^2 + \left(\frac{-Q_{evaporator}}{\dot{m}h_{lv}^2}U_{h_{lv}}\right)^2 + \left(\frac{qS_{ts}}{k^2}U_k\right)^2} \qquad (4.40)$$

4.2.8 Uncertainty of the Vapor Quality along the Evaporator

The uncertainties of the qualities between the inlet section and outlet section of the evaporator can be calculated assuming that the heat is proportionally distributed along the channel length of the evaporator. In other words, the uniform heat distribution is essential in order to find the interim vapor qualities. Uniform heat flux distribution is validated by measuring the temperature at the vertically aligned locations. Then, the temperature difference is found for each coupled sensors. All the temperature differences are found nearly the same providing the uniform heat flux distribution. The interim vapor qualities at the certain locations of the channel are given as:

$$x_n = x_{in} + \frac{L_n \Delta x}{L} \qquad (4.41)$$

Where index n is the interim number of the sensor locations and L is the total heated length of the channel. The sensor positions can be seen in Figure 3.2. The associated uncertainty is given as:

$$U_{x_n} = \sqrt{\left(U_{x_{in}}\right)^2 + \left(\frac{\Delta x}{L} U_{L_n}\right)^2 + \left(\frac{L_n}{L} U_{\Delta x}\right)^2 + \left(-\frac{L_n \Delta x}{L^2} U_L\right)^2}$$

(4.42)

The uncertainty of L_n is taken as ±0.1 mm.

4.2.9 Uncertainty of the Conductivity of the Block

The microchannel block is not purely copper and consists of some alloys. Therefore, the conductivity is unknown. The conductivity of the block is estimated by measuring the temperature of certain three locations along the same vertical alignment. Then, those temperatures are averaged to find the conductivity of the block. The maximum uncertainty that is calculated from the temperature measurements is taken as the uncertainty of the conductivity of the test block. The derivation is given as:

$$k = \frac{q \Delta H}{\Delta T}$$

(4.43)

Where ΔH is the distance between the temperature sensors and ΔT is the temperatures between the thermistors that are being considered.

$$U_k = \sqrt{\left(\frac{\Delta H}{\Delta T} U_q\right)^2 + \left(\frac{q}{\Delta T} U_{\Delta H}\right)^2 + \left(\frac{-q \Delta H}{(\Delta T)^2} U_{\Delta T}\right)^2}$$

(4.44)

4.2.10 Uncertainty of the Wall Temperature

The wall temperature is derived from the measured values of NTCs at the sensor locations of channel block assuming 1D heat conduction. The formula of this estimation is given as

$$T_{\text{wall}} = T_{\text{ts}} - \frac{q S_{\text{ts}}}{k}$$

(4.45)

where S_{ts} is the distance between sensor location and thermistors. The uncertainty of S_{ts} is given as ±0.1 mm within the diameter of the sensor position. The uncertainty is derived as follows:

$$U_{T_{\text{wall}}} = \sqrt{\left(U_{T_{\text{ts}}}\right)^2 + \left(\frac{-S_{\text{ts}}}{k} U_q\right)^2 + \left(\frac{-q}{k} U_{S_{\text{ts}}}\right)^2 + \left(\frac{q S_{\text{ts}}}{k^2} U_k\right)^2}$$

(4.46)

4.2.11 Uncertainty of the Heat Transfer Coefficient

The uncertainties of the heat transfer coefficients are defined by Equation 4.47. The estimated uncertainties of U_q, $U_{T_{sat}}$, $U_{T_{wall}}$ are inserted into Equation 4.47

$$\frac{U_h}{h} = \left[\left(\frac{1}{q} U_q \right)^2 + \left(-\frac{U_{T_{sat}}}{T_{wall} - T_{sat}} \right)^2 + \left(\frac{U_{T_{wall}}}{T_{wall} - T_{sat}} \right)^2 \right]^{1/2}$$ (4.47)

4.2.12 Uncertainty of Thermistors

Before starting the tests, all thermistors are calibrated and the maximum uncertainty of 40 mK from calibration results is used as the uncertainty value for all thermistors.

4.2.13 Uncertainty of Channel Dimensions and Heated Length

The uncertainties of the channel width, height and length are given for each sample as follows:

Table 4.3 Uncertainties of Channel Geometries

Dimensions	Sample 1	Sample 2
Channel Width (W)	1.5±0.04 mm	0.5±0.04 mm
Channel Height (H)	1.5±0.04 mm	0.5±0.04 mm
Channel Length (L)	100±0.52 mm	100±0.52 mm

The uncertainties of the measurement devices are given in Table 4.4.

Table 4.4 Uncertainties of the Measurement Equipments

Measurement Equipment	Uncertainty of the Measurement Equipment
Cori-Flow Meter	±0.2% of full scale
NTC Temperature Sensors	±0.04 K
Evaporator Power Supply	±0.2% Current Monitoring accuracy
Preheater Power Supply	±0.2% Voltage Monitoring accuracy
Thermocouples	±0.2 K
Absolute Pressure Sensor	±0.5% of full scale
Differential Pressure Sensor	±0.2% of full scale

One of the uncertainty analysis results is given in Figure 4.5. The contributions of uncertainties to error bars are summarized in Table 4.5. Generally, the uncertainties of heat transfer coefficient and vapor qualities are found around 15%-19% and 1%-3% (from inlet till exit of the channel), respectively. A separate study has been performed to estimate the individual uncertainty contributions of measurement parameter to heat transfer coefficient and vapor quality uncertainties. The detailed results are provided in Section 10.1 of Appendix. It is found that the most pronounced contribution is from the pressure sensor uncertainty to the heat transfer coefficient uncertainty and vapor quality uncertainty (11.07% and 0.58%, respectively). Uncertainties of mass flux, preheater and evaporator power supplies and channel length are insignificant compared to uncertainties of the pressure sensor.
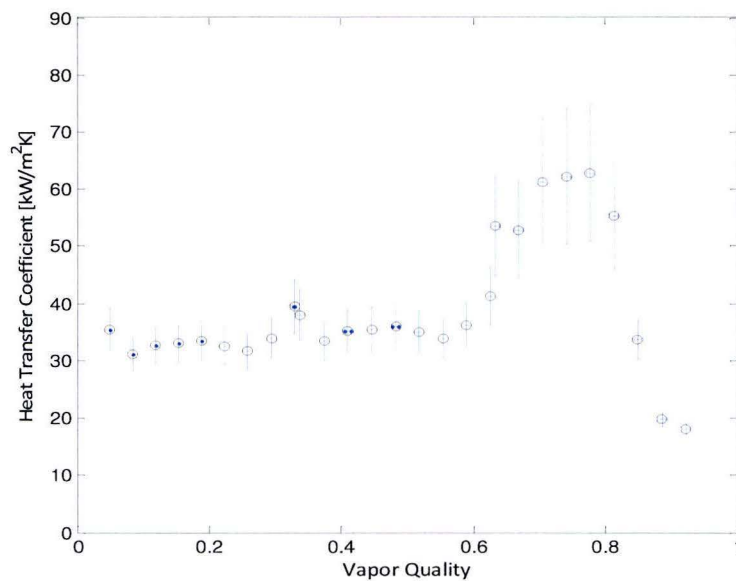
Figure 4.5 Uncertainty Analysis of q=75 kW/m^2, G=300 kg/m^{2}s, D_h=1.5 mm

Table 4.5 Experimental Measurement Uncertainties of Figure 4.5

Parameter	Uncertainty
Heat Flux (q)	2.73% of 75 kW/m^2
Mass Flux (G)	0.05% of 300 kg/m^{2}s
Wall Temperature (T_{wall})	Maximum uncertainty of 0.34% at 25.6 °C
Conductivity (k)	2.85% of 177 W/mK
Saturation Temperature (T_{sat})	0.95% of 22°C
Preheater Power ($P_{preheater}$)	0.28% of 33.9W
Evaporator Power ($P_{evaporator}$)	0.3% of 78.84W
Latent Heat of Vaporization (h_{lv})	0.84% of 139.76 kJ/kg
Channel Length (L_h)	0.52% of 100 mm
Vapor quality (x)	Maximum uncertainty of 1% at 0.92
Heat Transfer Coefficient (h)	Maximum uncertainty 19.1% at 63.2 kW/m^{2}K

This page is intentionally left blank.

5   CO$_2$ FLOW PATTERN MAP AND ADIABATIC FLOW VISUALIZATION

The goal of this chapter is to present the visualization of CO$_2$ two-phase flows in a 1.5 mm square channel. First, a brief review of flow patterns, flow regime maps and some literature studies of CO$_2$ two-phase flows are presented. In Section 5.2, experimental flow visualization results are explained and discussed.

Two-phase flow pattern maps can give useful information for analyzing heat transfer and pressure drop since heat transfer and pressure drop mechanisms are influenced by flow patterns. Before discussing the flow patterns, it is necessary to define flow structures. Some common flow pattern structures for horizontal tube configuration are shown in Figure 5.1.
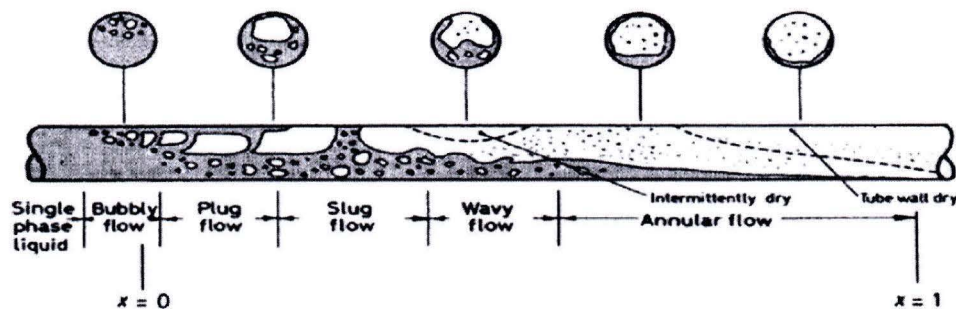
Figure 5.1 Schematic of flow patterns in horizontal two-phase flow during evaporation, Collier and Thome [22]

Bubbly flow is associated with a uniform distribution of small spherical bubbles within the liquid phase. Intermittent flow is characterized by the flow of liquid plugs separated by elongated gas bubbles often in the shape of slugs or bullets. In annular flow, a relatively thin liquid layer flows through the channel walls, while the vapor flows in the center of the channel, creating a vapor core which may also contain entrained droplets. At very high gas flow rates, the annular film is thinned by the shear force of vapor core until it is destroyed. This flow type is called mist flow where the liquid droplets flow in the gas flow.

CO$_2$ flow visualization studies have been conducted by Pettersen [23], Yun and Kim [24], Park and Hrnyak [25], and Mastrullo et al. [28]. Pettersen [23] visualized the flow patterns in a tube with a diameter of 0.98 mm at an evaporation temperature of 20 °C and a heat flux of 13 kW/m^2. He reported that intermittent and annular flow regimes were dominant at the test conditions and the flow pattern did not fit any available flow pattern structures. Yun and Kim [24] visualized the flow patterns at an evaporation temperature of 5.3 °C in rectangular channel with 2 mm height and 16 mm wide dimensions. Park and Hrnjak [25], observed the flow patterns in a 3.5 mm tube at evaporation temperatures of -15 °C and -30 °C, mass fluxes of 200 kg/m^{2}s and 400 kg/m^{2}s and heat fluxes from 5 kW/m^2 to 15 kW/m^2 for vapor qualities ranging from 0.1 to 0.8. They reported that flow patterns can be predicted by the flow pattern maps of Weisman et al. [26] and Wojtan et al. [27]. Mastrullo et al. [28]

identified the influence of reduced pressure on the flow map transitions of Cheng et al. [29] and proposed new versions of the transition equations of the flow pattern map according to their database.

5.1 CO$_2$ Flow Pattern Map

Cheng et al. [29] proposed the first flow pattern map that is only valid for CO$_2$. The general flow pattern map of Wojtan et al. [27] was modified by Cheng et al. [29] for two-phase flow of CO$_2$. Since the flow regime transitions and the heat transfer trends are intrinsically related to each other, Cheng et al. [29] developed the map using heat transfer data points collected from independent literature studies. In particular, starting from the experimental results of independent databases and observing the sharp drop of heat transfer coefficients with vapor quality, they fit the coefficients of the formulas presented in paper of Wojtan et al. [27] to CO$_2$ for the transitions from intermittent to annular flow and from annular flow to dryout. The updated flow pattern map is applicable to tube diameters from 0.6 to 10 mm, mass velocities from 50 to 1500 kg/m^{2}s, heat fluxes from 1.8 to 46 kW/m^2 and saturation temperatures from -28 to 25 °C (reduced pressures from 0.21 to 0.87). This flow pattern map is intended for both diabatic and adiabatic cases. The CO$_2$ flow pattern map consist of slug, bubbly, stratified, stratified wavy, intermittent, dryout, and mist flow regions. This flow pattern map is implemented with the corresponding heat transfer and pressure drop equations by Matlab. All the equations can be found in the original paper [29]. An example is shown in Figure 5.2-Figure 5.4 in order to clarify the relationship between flow pattern maps, heat transfer and pressure drop relations. The vertical dashed lines in the graphs delineate the flow pattern transition boundaries predicted by the map. In the intermittent flow regime, the heat transfer coefficient tends to be flat at low vapor qualities where nucleate boiling dominates without suppression. When the flow becomes annular, the boiling suppression becomes more pronounced with a slight reduction the heat transfer coefficient which is not pronounced in Figure 5.3. At the higher qualities of the flow regime, the onset of dryout is reached where heat transfer coefficient starts to drop sharply. End of the dryout region and beginning of the mist flow region is denoted by beginning of the slightly increasing but mostly flat line where main flow is vapor with liquid droplets.
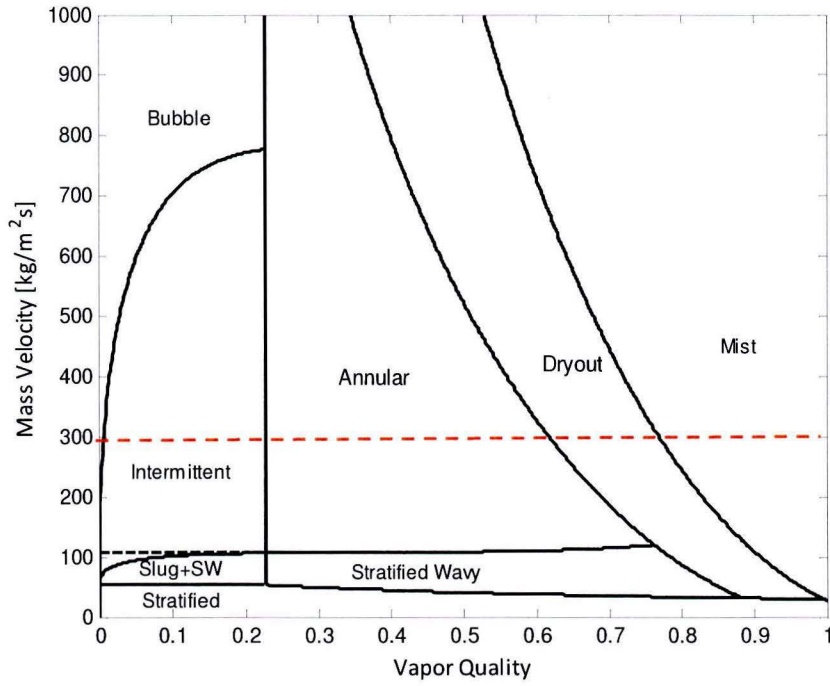
Figure 5.2. Flow Pattern Map of CO_2 by Cheng et al. [29] at q=20 kW/m^2, D_h=1.5 mm
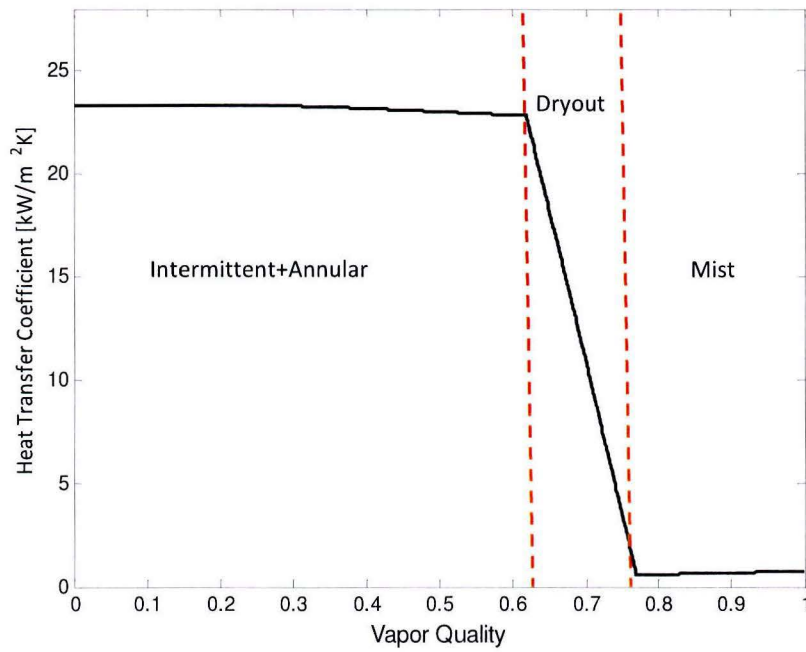
Figure 5.3. Heat Transfer Coefficient of CO_2 by Cheng et al. [29] at q=20 kW/m^2, G=300kg/m^{2}s, D_h=1.5mm
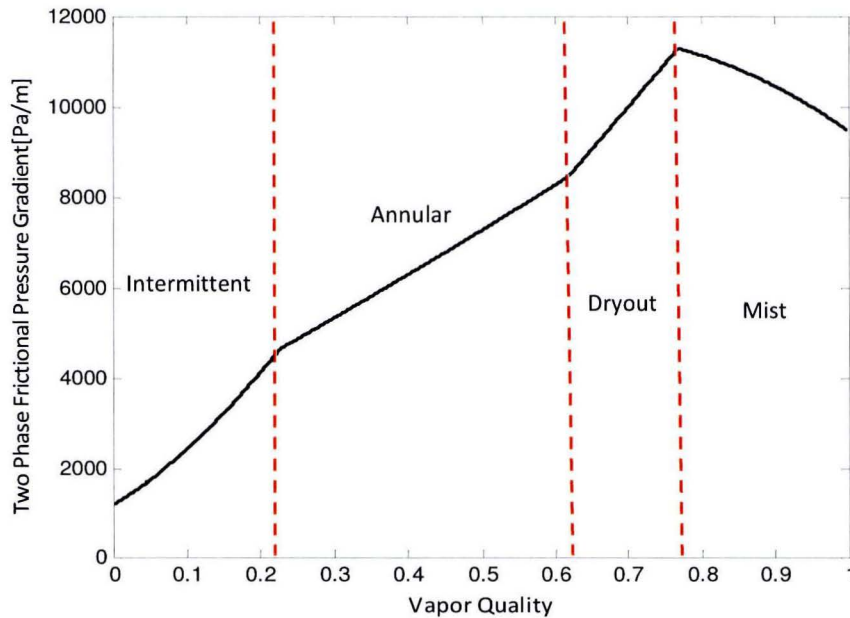
Figure 5.4. Frictional Pressure Gradient of CO_2 by Cheng et al. [29] at *q*=20 kW/m², *G*=300 kg/m²s, *D_h*=1.5mm

5.2   Flow Visualization Experiments and Results

An experimental study of flow visualization inside of square channel geometry with a side dimension of 1.5 mm is performed for an adiabatic case at different mass fluxes. The same test set- up explained in Section 3.2 is used with the exception that evaporator section is replaced by visualization section with an optical access and no heat is supplied to visualization section. A high speed camera is installed vertically to the test section to observe the flow patterns. The light source is located just before the lenses of high speed camera. Shooting distance of the camera and light intensity is adjusted to capture the clearest image of the fluid. Since the flow visualization is performed from the top view of the test section, the variations of the flow patterns in the direction of channel depth cannot be observed. Therefore, flow patterns are observed in the directions of channel length and width. The tests are performed at adiabatic conditions where the flow visualization section is placed after the preheater. The inlet quality of the observation section is adjusted with preheater. The experimental set-up is shown in Figure 5.5:
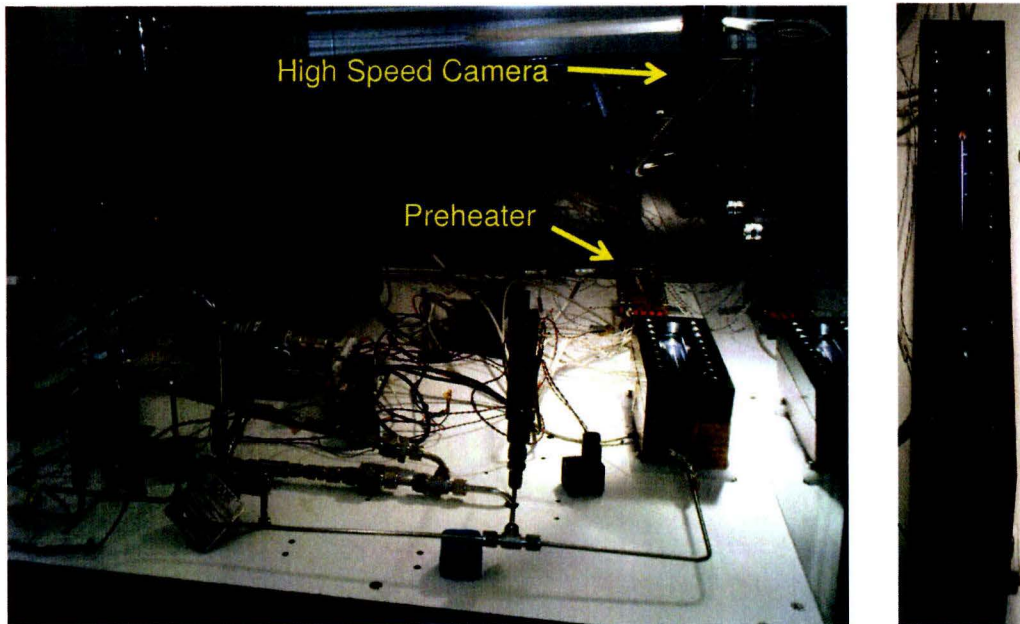
Figure 5.5 Flow Visualization Test Set-Up and Visualization Test Sample

The uncertainty in the vapor quality is estimated via an uncertainty analysis as explained in Section 4.2.8. and maximum uncertainty is found as ±3.5% of the vapor quality. The heat loss is measured by comparing the electrical heat input with actual heat transfer to the fluid in terms of the enthalpy difference between the sub-cooled inlet and outlet fluid of CO_2. The mass flux is held constant while the input power is varied through the desired range. The images are acquired at 3000-4000 fps after the system has reached steady state conditions. The visible light and dark regions surround the flow channel. Changes in image capture rate, ambient light and exposure time may have some affect on the appearance of the channel and its surroundings. For each flow rate, the qualities from 0 to 0.9 are observed. At adiabatic conditions, bubble, intermittent, annular and mist flow regimes are detected. Combination of slug and plug flow is named as intermittent flow during the evaluation of the flow observations by considering the definition of Cheng et al [29]. Annular flow is assumed to be the regime when no bubbles were observed and some wavelike form appeared in the flow. The visualization results for annular flows were not all much clear. At the lowest mass velocity case, 100 kg/m^{2}s, the fluctuations were observed in the flow due to approaching lowest pump capacity. Flow visualization of 47 test conditions and their results are given in Table 5.1 with the corresponding flow structures shown from Figure 5.6 to Figure 5.9. In all these figures, CO_2 flow is from left to right.

Table 5.1 Experimental Conditions and Results at Adiabatic Conditions

G (kg/m^{2}s)	Liquid and Vapor Reynolds Numbers	Vapor Quality	Flow Regime
100	Re$_l$: 2145;1906;1668;1430;1191;953;715;476;238 Re$_v$: 798;1596;2394;3192;3990;4789;5587;6385;7183	0.1-0.3 0.4-0.5 0.6-0.9	Slug Flow Plug Flow Annular Flow
200	Re$_l$: 4290;3813;3336;2860;2383;1906;1430;953;476 Re$_v$: 1596;3192;4789;6385;7981;9578;11174;12771;14367	0.1-0.2 0.3-0.4 0.5-0.8 0.9	Bubbly/Plug Flow Plug/Annular Flow Annular Flow Mist Flow
400	Re$_l$: 8580;7626;6673;5720;4766;3813;2860;1906; 953 Re$_v$: 3192;6385;9578;12771;15963;19156;22349;25542;28735;31927	0.1 0.2 0.3-0.7 0.8-0.9	Bubble Flow Bubble/Annular Annular Mist Flow
600	Re$_l$: 12870,2;11440,1;10010,1;8580,1;7150,1;5720,1;4290;2860;1430 Re$_v$: 4789;9578;14367;19156;23945;28735;33524;38313;43102	0.1 0.2 0.3-0.6 0.7 0.8-0.9	Bubble Flow Bubble/Annular Annular Annular/Mist Mist
800	Re$_l$: 17160;15253;13346;11440;9533;7626;5720;3813;1906 Re$_v$: 6385;12771;19156;25542;31927;38313;44698;51084;57470	0.1 0.2-0.5 0.6-0.9	Bubble Flow Annular Flow Annular/Mist Flow
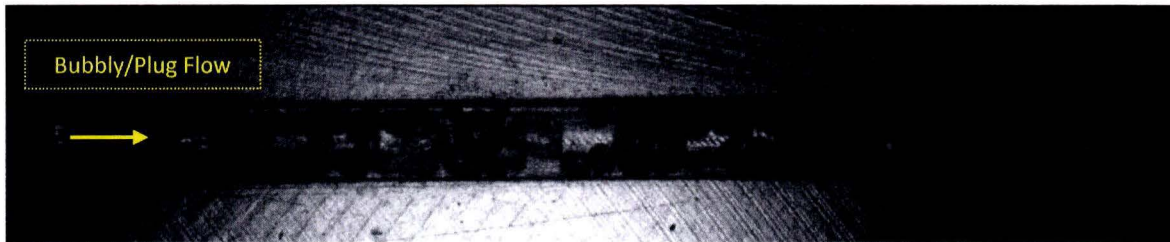
Figure 5.6. Bubbly/ Plug Flow Pattern at $q=0$, $G=200$ kg/m^{2}s, $x=0.1$
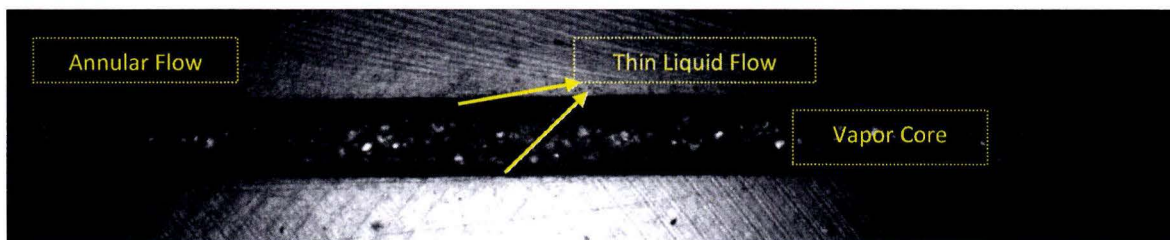
Figure 5.7. Annular Flow Pattern at $q=0$, $G=200$ kg/m^{2}s, $x=0.7$
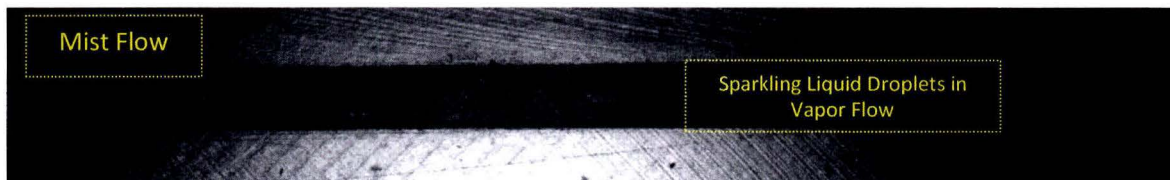
Figure 5.8. Mist Flow Pattern at $q=0$, $G=400$ kg/m^{2}s, $x=0.9$
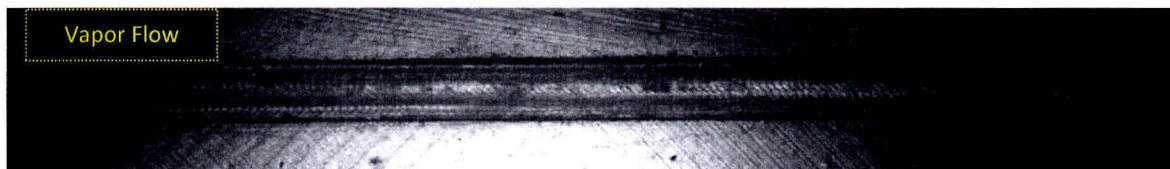
Figure 5.9. Vapor Flow at $q=0$, $G=600$ kg/m^{2}s, $x=1.0$

The flow patterns observed in the flow visualization tests are plotted in Figure 5.10, on the flow pattern map developed by Cheng et al. [29]. The boundaries drawn on a map as lines should be viewed as broad transition regions from one well defined flow pattern to another. In the model of Cheng et al. [29], slug to intermittent, intermittent to annular transitions are affected by the following set of physical parameters: mass velocity, vapor quality, and selected fluid saturation properties of liquid viscosity, surface tension and liquid density. These parameters can be grouped together in two non-dimensional

numbers, the liquid Reynolds number and the liquid only Weber number, expressed by the following definitions:

$$Re_l = \frac{G(1-x)D}{\mu_l} \tag{5.1}$$

$$We_{lo} = \frac{G^2 D}{\rho_l \sigma} \tag{5.2}$$

Liquid Reynolds number accounts for the inertia to dissipative forces ratio which can be considered a measure of liquid turbulence that can contribute to break up of the interface during intermittent flow; liquid only Weber number representing the inertia to surface tension ratio can be related to the amplitude of the liquid waves which can block the passage of the vapor phase during slug flow. The mass velocity influence on transition from slug to intermittent flow is small so that it does not shown on the flow pattern map.
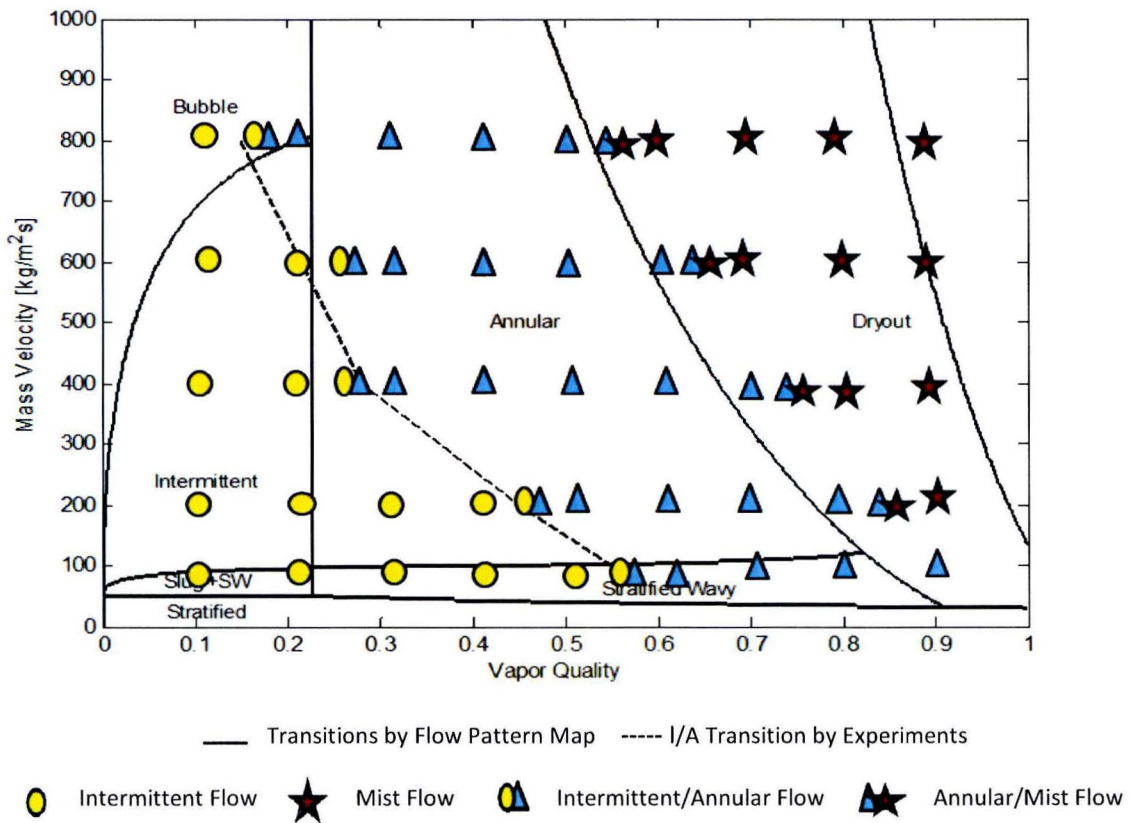
Figure 5.10 Experimental Flow Pattern Observations on CO$_2$ Flow Pattern Map by Cheng et al. [29]

It is observed that transition boundaries at mass velocities higher than the 400 kg/m^{2}s are difficult to distinguish. This is mainly because the both liquid and vapor phases become more turbulent and flow becomes more chaotic as the mass flow rate increases. The Reynolds numbers of liquid and vapor

phases at each vapor qualities are listed in Table 5.1, and turbulence and laminar flow statues of the both phases can be seen in that table. In the map of Cheng et al. [29], transition from intermittent to annular region is defined at a constant value of the Lockhart-Martinelli parameter, corresponding to a constant value of vapor quality, $x_{I/A}$. According to flow observation results, this transition depends on the mass velocity, and is not a constant line as the map predicted. The transition from intermittent to annular region occurs at higher vapor qualities for low mass velocities; at lower vapor qualities for high mass velocities. The fitted line is shown in Figure 5.10. The early transition at higher mass velocities associated with liquid droplet entrainment. Liquid droplet entrainment into the vapor core increases with a rise of mass flux due to a higher vapor velocity. The vapor region at the channel center increases with a rise of mass flux, while the liquid film thickness at the sides of the test section becomes smaller which brings the flow into annular flow condition. The similar results are also shown by Mastrullo et al. [29] for CO_2 saturation temperature of 12 °C at diabatic conditons of 5 kW/m^2 and 20 kW/m^2. In the flow observation, direct transition from annular to mist flow regime is observed without dryout region that is shown on the flow pattern map. In order to observe dryout, wall temperature measurements are needed at diabatic flow conditions. However, the flow visualization sample did not have any place for wall temperature measurements. In addition, the visualization block had heat leaking problems to sides preventing the flow to bring the desired test conditions. Therefore, diabatic condition tests to observe the annular to dryout and dryout to mist flow transitions are planned as a future work.

This page is intentionally left blank.

6 TEST RESULTS

This chapter is devoted to represent experimental results with influence of test parameters and comparison of experimental results with some common two-phase heat transfer correlations. It is observed that boiling heat transfer coefficients of CO_2 varies significantly before and after the dryout quality. When the CO_2 evaporates in the channel, the liquid film becomes thinner and thinner until the vapor quality reaches a critical value, dryout vapor quality, where the liquid film breaks down. At that time, the direct contact area of the vapor on the channel wall increases and heat transfer coefficient reduces sharply. An example can be seen in Figure 6.1. The onset of dryout is estimated by recording the temperature evolution during the scanning of the two-phase region. For instance, Figure 6.2 presents an example of temperature evolution during the whole scanning process for the case shown in Figure 6.1. The wall temperature starts to increase which indicates the onset of dryout at vapor quality of 0.91. This phenomenon reflects itself as the wall temperature increase.
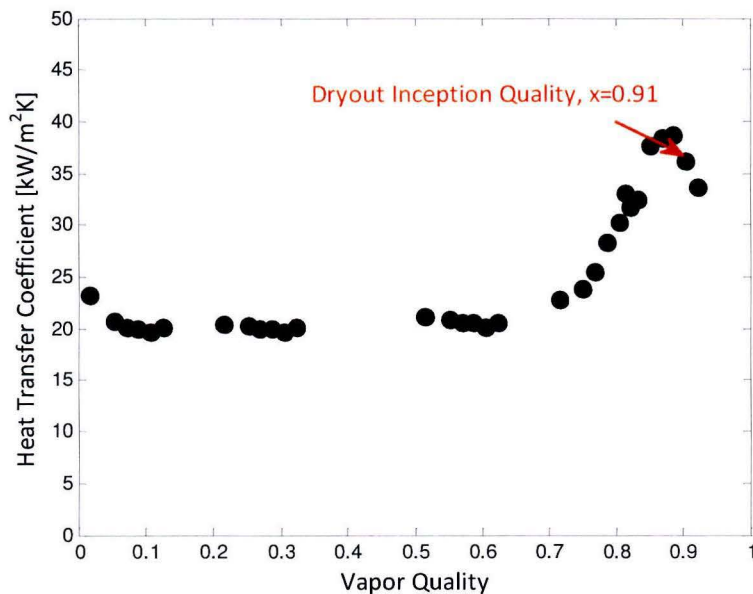
Figure 6.1 Reflection of Dryout Occurrence on the Heat Transfer Coefficient at *q*=38 kW/m², *G*= 300 kg/m²s, *D*ₕ=1.5 mm, *T*ₛₐₜ=22 °C
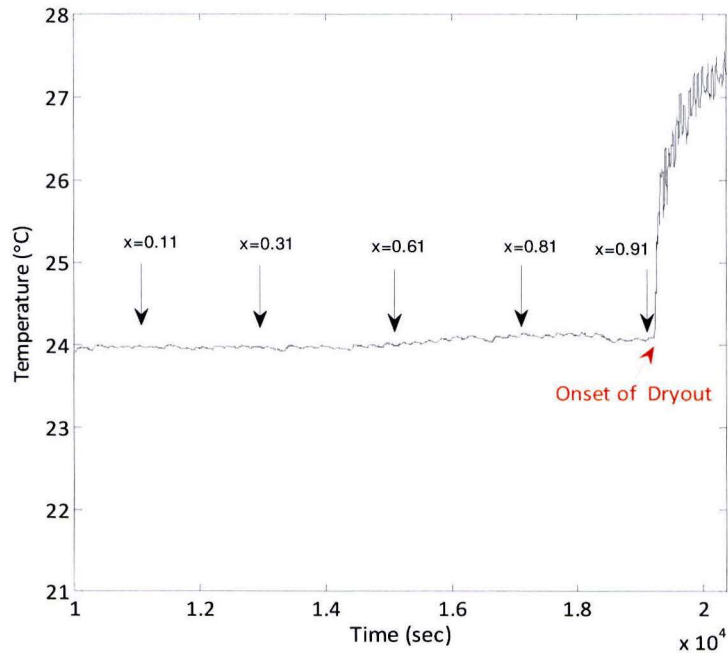
Figure 6.2 Wall Temperature Profile of the Thermistor for the Case in Figure 6.1

From the experimental results, it is found that CO_2 two-phase heat transfer coefficient generally increases slightly or stays the same with increasing vapor quality until the dryout condition. Once the dryout quality is reached, the heat transfer coefficient decreases sharply. Therefore, it is necessary to develop two different heat transfer correlations separately before and after the critical vapor quality. Building a model to capture these complicated trends requires characterizing the heat transfer at each region individually. In this study, pre-dryout heat transfer characteristics are explored and analyzed.

In general heat transfer correlations, the local heat transfer coefficient is considered to be the net effect of the two mechanisms: nucleate boiling and convective boiling. When the nucleate boiling is dominant, heat transfer is strongly dependent on heat flux but a weakly dependent on vapor quality. In convective boiling regime, the heat transfer coefficient is almost independent of heat flux, but it is strongly affected by the mass flow rate and vapor quality. According to Webb and Gupte [31], the classification of the different models can be done according to the manner of interactions between the nucleate and convective boiling mechanisms:

- Intensification model: $h = N h_{cb}$
  The general form of the intensification model is based on an enhancement factor applied to Dittus-Boelter single phase (liquid phase) heat transfer coefficient as given in Equation 8.1. This model assumes that heat transfer is primarily due to single-phase convection and a modification is used to represent enhancement due to nucleate boiling.

46

- Superposition model: $h = h_{\text{cb}} + h_{\text{nb}}$

  The general form of superposition model is based on the assumption that two-phase heat transfer coefficient results from the linear contribution of the nucleate boiling heat transfer and convective boiling heat transfer.

- Asymptotic model order of n: $h^n = h_{\text{cb}}^n + h_{\text{nb}}^n$

  The general form of asymptotic model is based on the combination of nucleate boiling and forced convection heat transfers in power law form. For n equal to 1, the form becomes that of the superposition model. In asymptotic models, the value approaches asymptotically to the larger of the two terms when n is greater than 1. For example, a large convective component and a small nucleate boiling component, the total two-phase heat transfer coefficient is made up almost entirely of the convective boiling component; for a nucleate boiling dominated situation, the total two-phase heat transfer coefficient is made up almost entirely by the nucleate boiling component.

Two-phase heat transfer models based on the classification given above are shown in Section 6.4. The comparisons of experimental data with those equations are presented and predictability of those correlations is analyzed as will be explained in Section 6.4.

6.1   Influence of Mass Flux

Figure 6.4 through Figure 6.7 depict the evolution of the heat transfer coefficient as a function of the vapor quality for tested mass fluxes at some heat flux conditions. Additional test results are provided in Section 10.2 of Appendix. Experimental results indicate that mass flux effect on the heat transfer coefficient is not strongly dominant. It can be seen that local heat transfer coefficients cluster to each other at nearly all mass flux conditions. The effect of mass flux can be analyzed in separated two sections, before dryout quality and after dryout quality, namely. Before the dryout region, the mass flux has less effect on the heat transfer coefficient. As the mass flux increases, the CO_2 heat transfer coefficient varies only a small amount (i.e. around 15%) at moderate heat fluxes such as from Figure 6.6 to Figure 10.3. Therefore, it can be said that the influence of mass flux on heat transfer coefficient is less dominant with the increase of heat flux.

In the pre-dryout regions, heat transfer coefficient increases just before the dryout point and that behavior is usually attributed to an enhancement of convective boiling heat transfer contribution which can be clearly seen in Figure 6.4. This is due to the fact that the enhancement factor increases as the vapor quality approaches to moderate level before dryout. Some of the enhancement factor models can be found in Table 6.1. When the heat transfer mechanism is not dominated by the nucleate boiling, this enhancement is realized as an increase in heat transfer coefficient before dryout quality. This case is mostly observed at low and moderate heat fluxes till a certain mass flux condition. After a certain mass flux (transition mass flux), the enhancement of the heat transfer coefficient with mass flux disappears. In all the tests, it turns out that heat transfer coefficient drops some amount after the transition mass flux.

However, that decrease of heat transfer coefficient is not distinct. In the study of Yun and Kim [33], mass flux effect on heat transfer coefficient is found to be significant when the liquid Weber number is less than 100. They defined the liquid Weber number based on superficial liquid velocity and it is given as

$$We_{ls} = \frac{\rho_L j_L^2 D_h}{\sigma}$$ (6.1)

Where j_L is the superficial liquid velocity and can be defined as

$$j_l = \frac{G(1-x)}{\rho_L(1-\epsilon)}$$ (6.2)

Where ϵ is the void fraction and it is given by Rouhani-Axelsson drift flux as

$$\epsilon = \frac{x}{\rho_v}\left[(1 + 0.12(1-x))\left(\frac{x}{\rho_v} + \frac{1-x}{\rho_L}\right) + \frac{1.18(1-x)[g\sigma(\rho_L - \rho_v)]^{1/4}}{G\rho_L^{1/2}}\right]^{-1}$$ (6.3)

In contrary to the result of Yun and Kim [33], Choi et al. [30] reported the insignificant effect of mass flux on heat transfer coefficient which is also the case of this study. This can be due to the fact that liquid Weber number varies between 342 (for 0.5 mm channel at 700 kg/m²s mass flux) and 8391 (for 1.5 mm channel at 2000 kg/m²s) before dryout qualities of 0.6 and 0.4, respectively. Those liquid Weber numbers support the findings of Yun and Kim [33] for this study.

In terms of dryout occurrence, two different trends of the dryout quality have been observed experimentally: decrease of dryout quality with mass velocity and increase of dryout quality with mass velocity. It is reported by Revellin et al. [32] that the first trend is detected for refrigerants and CO_2 whereas the second trend is seen only for CO_2 at high mass velocities. Some mass velocities are plotted against dryout vapor qualities at some experimental conditions in Figure 6.3. It is usually observed the higher mass flux causes dryout to become earlier although it is not influencing dryout strongly (i.e. test conditions of q=40 kW/m², D_h=1.5 mm; q=90 kW/m², D_h=1.5 mm; q=130 kW/m², D_h=1.5 in Figure 6.3). This result can be explained such that the high mass flux results in higher flow velocity that causes a higher liquid entrainment and that may cause dryout to become earlier. On the other hand, the second trend (increase of dryout quality with mass velocity) is seen at the high CO_2 mass velocities test conditions of q=75 kW/m², D_h=1.5 mm and q=100 kW/m², D_h=0.5 mm. The change of the trend is attributed to changes in the liquid film flow regimes by Revellin et al. [32]. Indeed, the mass velocity where the trend changes is called transition mass velocity at which the flow passes from laminar to transition ($G_{transition}$). The laminar film dryout describes the decrease of the dryout vapor quality with mass flux in their model. The transition film dryout is characterized by an increase of the dryout vapor quality with mass flux. They developed a criterion that can predict this transition mass velocity based on the liquid Reynolds number of the liquid film. Details of their method and some examples of this trend for CO_2 can be found in Section 10.3 of Appendix. Moreover, in the theoretical model of Revellin et al. [32], dryout vapor quality is predicted by dryout prediction correlation by Jeong [12] which does not agree with the current experimental data as it will be discussed in Chapter 7. All in all, model validation requires more experimental data and modification of the laminar-to-transition mass velocity equation of Revellin et al. [32]. Since the second trend is observed a few times and the effect on dryout vapor

quality is not pronounced, it is not taken into account during dryout correlation development part in Chapter 7.
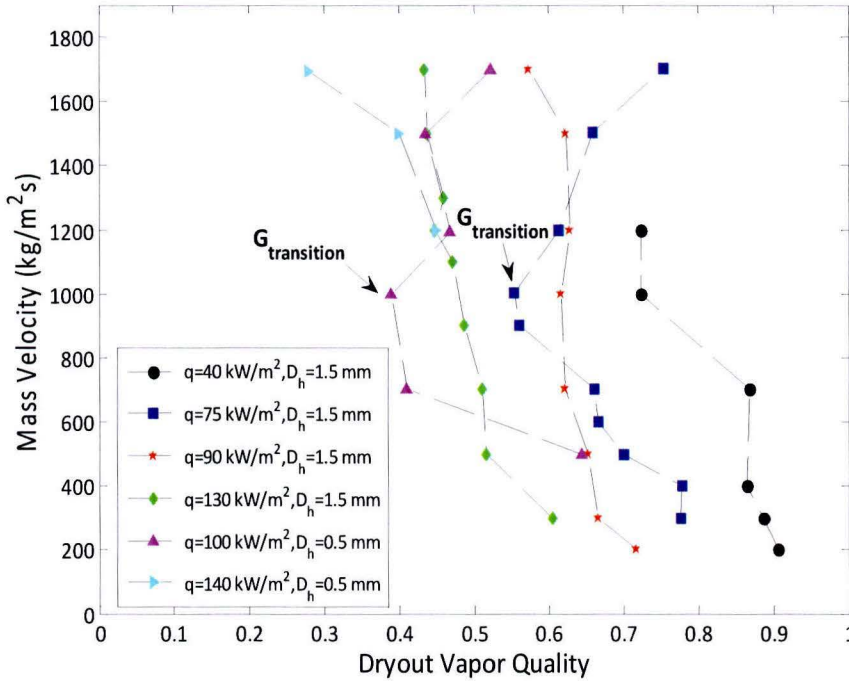
Figure 6.3 Experimental Mass Velocities vs. Dryout Vapor Quality at Some Test Conditions

After the dryout region, the heat transfer coefficient slowly decreases as the vapor quality increases. In those post dryout regions, mass flux effect is not strongly dominated on the heat transfer coefficient. However, it is still possible to observe that the higher the mass flux, the higher the heat transfer coefficient is. That can be seen in Figure 6.5 and Figure 6.6. At high post dryout vapor qualities (around 0.8-0.9) the low heat transfer coefficient slightly increases till vapor quality of 1.0. This observation is pronounced for higher mass velocities in Figure 6.5 and Figure 6.6. This trend is also observed in the CO_2 flow boiling study of Yun and Kim [33]. They reported that this tendency become more significant when the tube diameter is small, mass flux is very high and the surface tension of the fluid is very small. The reason is attributed to increase of liquid droplet concentration due to the collision of liquid droplets in the vapor core. The collision rates increase with a higher mass flux, smaller surface tension and smaller diameter. Therefore, due to a higher collision rated of liquid droplets to the wall, the heat transfer coefficient enhances slightly after dryout. The theory of this phenomenon is reported by Hewitt [34] and more detailed explanations can be found in the original paper.

49
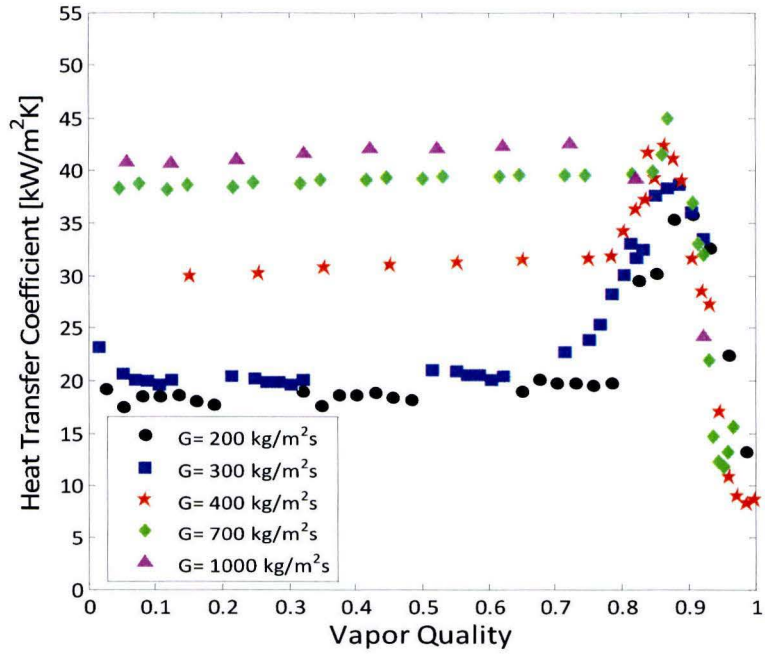
Figure 6.4 Heat Transfer Coefficient at q=40kW/m^2, T_{sat}=22 °C, D_h=1.5 mm
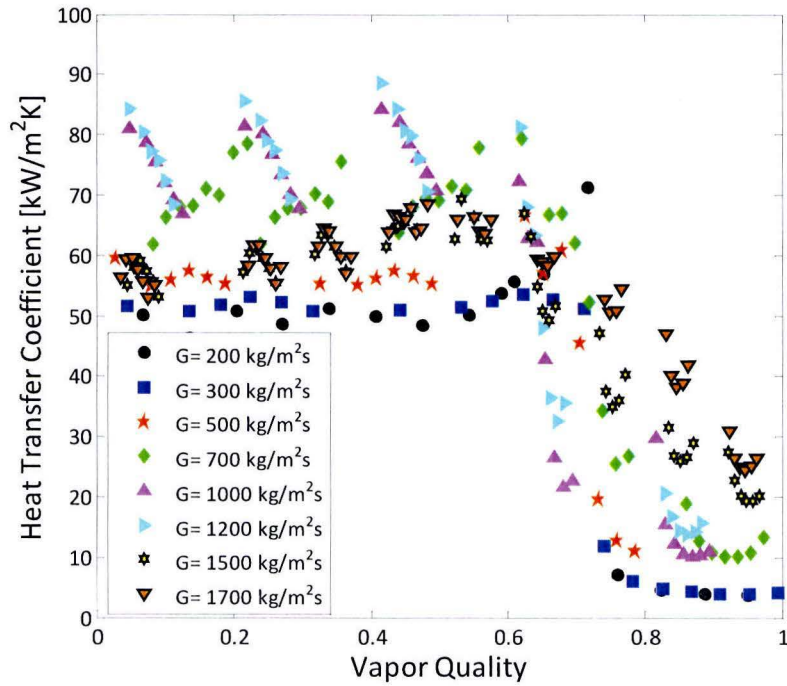
Figure 6.5 Heat Transfer Coefficient at q=90 kW/m^2, T_{sat}=22 °C, D_h=1.5 mm
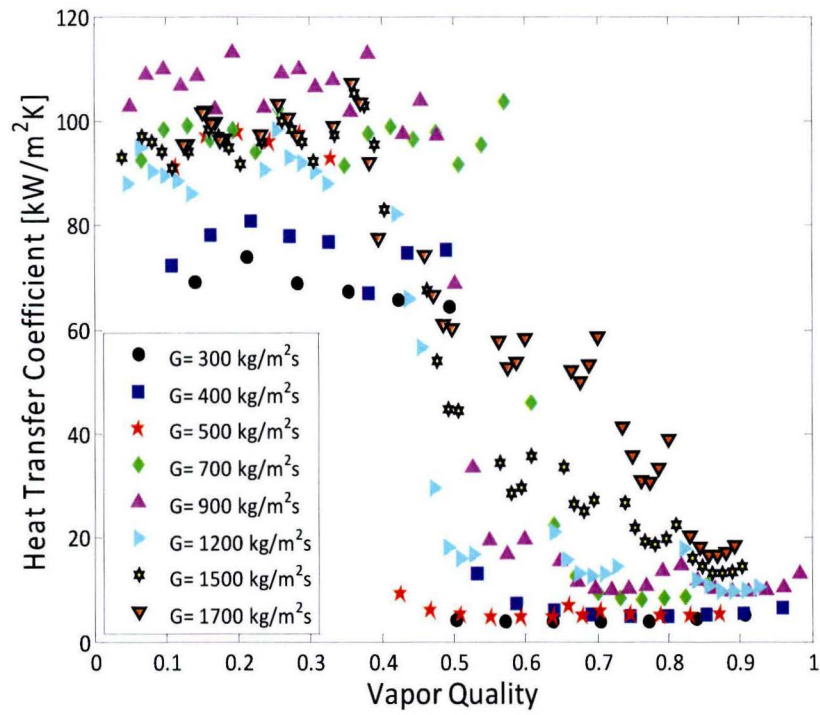
Figure 6.6 Heat Transfer Coefficient at q=130 kW/m^2, T_{sat}=22 °C, D_h=1.5 mm
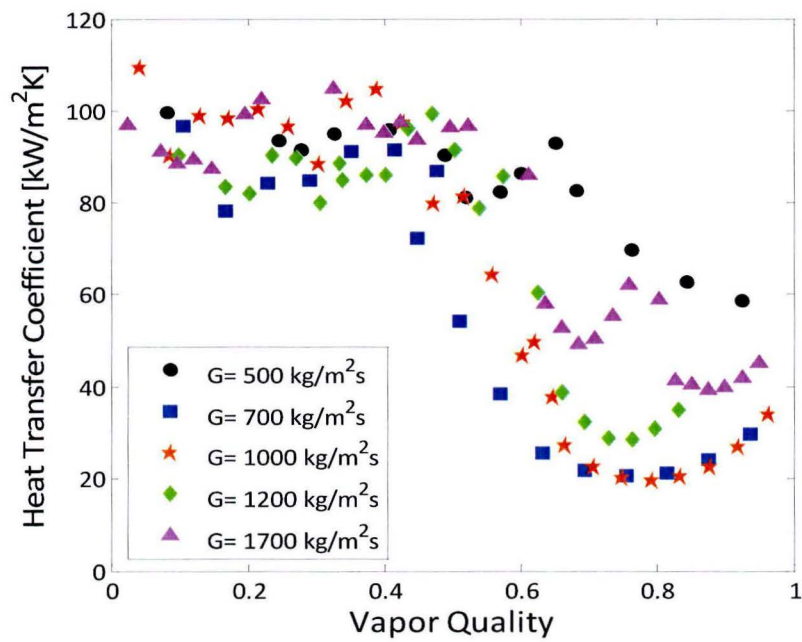
Figure 6.7 Heat Transfer Coefficient at q=100 kW/m^2, T_{sat}=22 °C, D_h=0.5 mm

In conclusion, two-phase heat transfer mechanism of CO_2 is not dominated by mass flux although explanatory answers are provided to small changes of heat transfer coefficient with mass flux. This fact implies that convective boiling contribution of CO_2 is not dominant. The convective boiling equation is usually expressed by Dittus-Boelter type [35] or modified Dittus-Boelter type (i.e. in Cheng et al. [14]) heat transfer equation in most of the two-phase heat transfer models. It is sometimes referred as the liquid only heat transfer coefficient, h_l. The original Dittus-Boelter equation [35] is given as:

$$h_{\text{Dittus-Boelter}} = 0.023 \frac{k_1}{D_h} \text{Re}_l^{0.8} \text{Pr}_l^{0.4} \tag{6.4}$$

An enhancement factor, F or E, is often introduced as a multiplication factor of convective boiling. That factor is modeled with different approaches by researchers and combination of non-dimensional numbers with the vapor quality. The liquid fraction flowing in the channel, $G(1-x)$, is included in the convective boiling contribution in the enhancement factors or in the Reynolds number of Equation 6.4. Then, the general form of convective boiling is given as

$$h_{\text{cb}} = E h_{\text{Dittus-Boelter}} \tag{6.5}$$

Available enhancement factor models are different from each other and they are taken into account within their original two-phase heat transfer models during the comparison of experimental data with those models in Section 6.4. For simplicity, only Dittus-Boelter equation [35] will be taken as convective boiling term without considering enhancement factors. In Figure 6.8, the ratio of original Dittus-Boelter equation [35] to all experimental data is plotted along the vapor quality to find out the dominancy of the convective boiling contribution. The low ratio of the convective boiling to test results confirms the little contribution of convective boiling heat transfer coefficient to the total heat transfer coefficient. The reason of small convective boiling contribution can be explained by the physical properties of CO_2. The flow tends to boil easily because of low surface tension of CO_2 at 22 °C saturation temperature (i.e. at high reduced pressure). As a result, convective boiling cannot occur since it requires a temperature gradient in the fluid. In addition, thermal conductivity of CO_2 is lower at high saturation temperatures which results in lower contribution of convective boiling to total heat transfer.
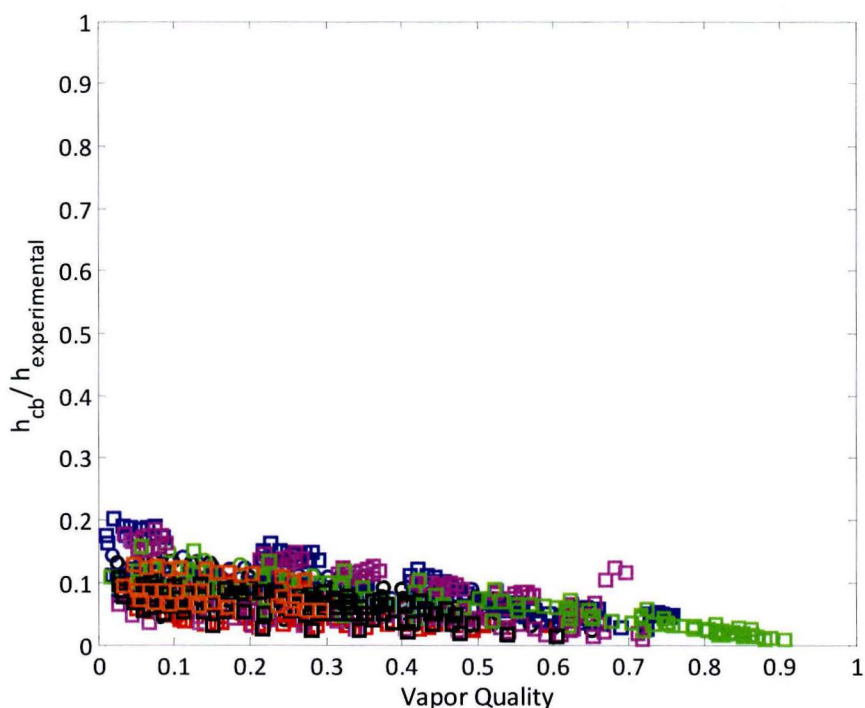
Figure 6.8 Comparison of Experimental Heat Transfer Coefficient with Convective Boiling Correlation

6.2   Influence of Heat Flux

The effect of heat flux on the heat transfer coefficient is shown from Figure 6.9 to Figure 6.12. Experimental results indicate that heat flux has a strong effect on heat transfer coefficient before critical vapor quality.

In the pre-dryout region, the heat transfer coefficient increases with the increase of heat flux because the higher heat flux creates more nucleation points and enhances the nucleate boiling inside the channel. However, higher heat flux causes early dryout with a reduction of heat transfer coefficient. The similar trend is also observed in CO_2 two-phase heat transfer studies of Oh et al. [36], Choi et al. [30] and Pettersen [23]. Although the increase of heat flux enhances pre-dryout heat transfer coefficient, it is not the case for all test conditions. Especially, at very high heat fluxes a certain drop of heat transfer coefficient is observed. (See Figure 6.10 at 147kW/m^2 heat flux case, Figure 6.11 at 240 kW/m^2 heat flux case). This can be due to increase of vapor fraction in two-phase flow near the channel wall that results in relatively low heat transfer coefficient. High saturation temperature (22 °C) provides a lower surface tension of CO_2. The higher vapor formation is favored at high heat fluxes and at high saturation temperature which may cause dryout patches become larger and result in a relative decrease of heat transfer coefficient.

After dryout vapor quality, the nucleate boiling is suppressed at high vapor quality, wherein the effect of heat flux on the heat transfer coefficient tends to disappear. The heat transfer coefficients are merged together regardless of heat flux, and the effect of heat flux becomes negligible. The reduction of heat transfer coefficient for the higher heat flux occurs at a relatively lower quality; sometimes it is observed that very early dryout occurs around 0.1 vapor qualities at high heat flux test conditions. For example, early dryout can be seen in Figure 6.10 at 200 kW/m^2 heat flux test, in Figure 6.12 at 250 kW/m^2 and 400 kW/m^2 heat fluxes.

The increase of heat transfer coefficients with heat flux infers that nucleate boiling contribution to total heat transfer coefficient is dominant. The reason of high nucleate boiling contribution is mainly due to the physical properties of the CO_2. Especially at higher saturation temperatures, surface tension and liquid to vapor viscosity ratio becomes lower and allow easy break-up of liquid droplets into vapor. Bubble nucleation sites can occur easily and this enhance the nucleate boiling contribution. The detailed discussion is provided in Section 6.3. In addition to observations of test results, the studies of Kew and Cornwell [37], Tran et al. [38], and Petterson [23] provided that the nucleate boiling is predominant heat transfer mechanism in small channels.
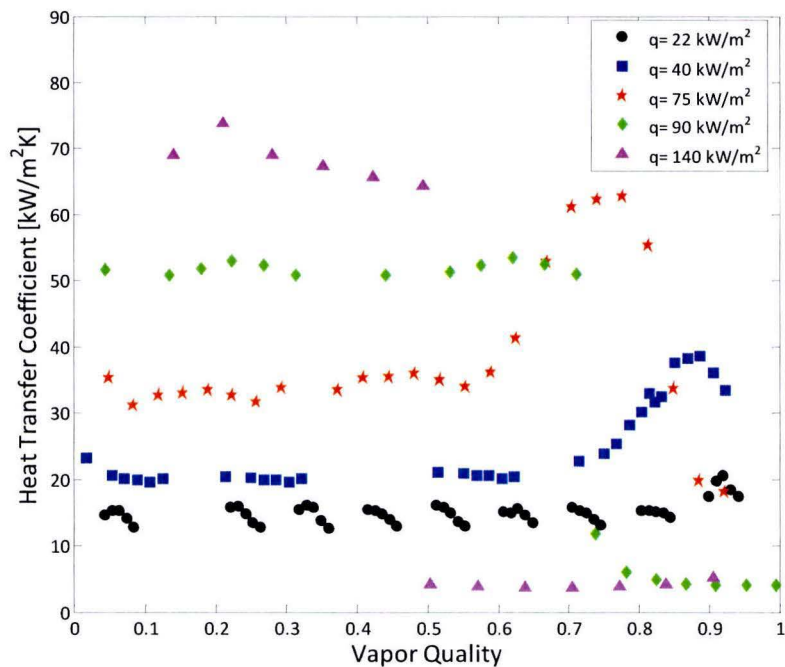
Figure 6.9 Heat Transfer Coefficient at G=300 kg/m^{2}s, T_{sat}=22 °C, D_h=1.5 mm
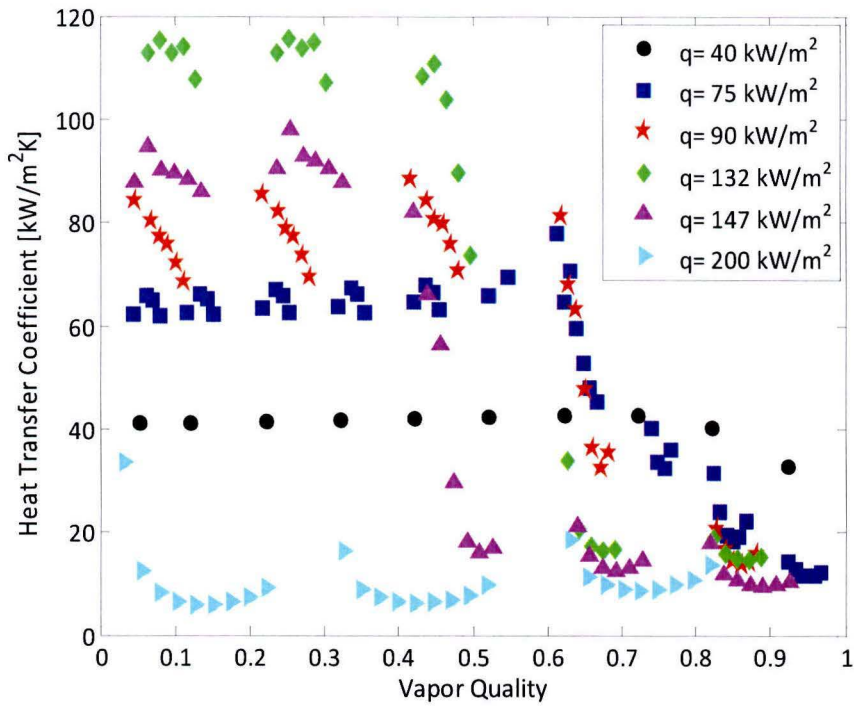
Figure 6.10 Heat Transfer Coefficient at *G*=1200 kg/m²s, *T*sat=22 °C, *D*h=1.5 mm
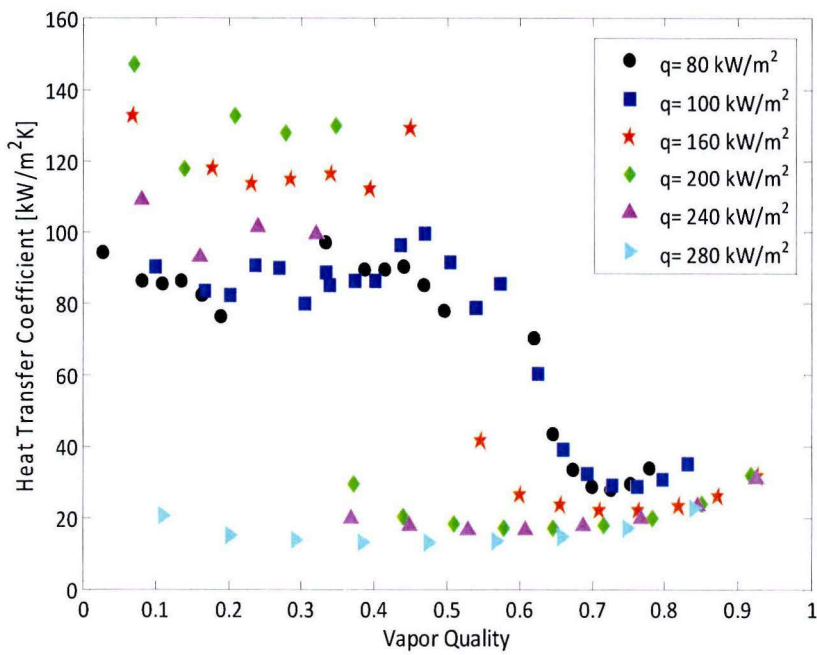
Figure 6.11 Heat Transfer Coefficient at *G*=1200 kg/m²s, *T*sat=22 °C, *D*h=0.5 mm
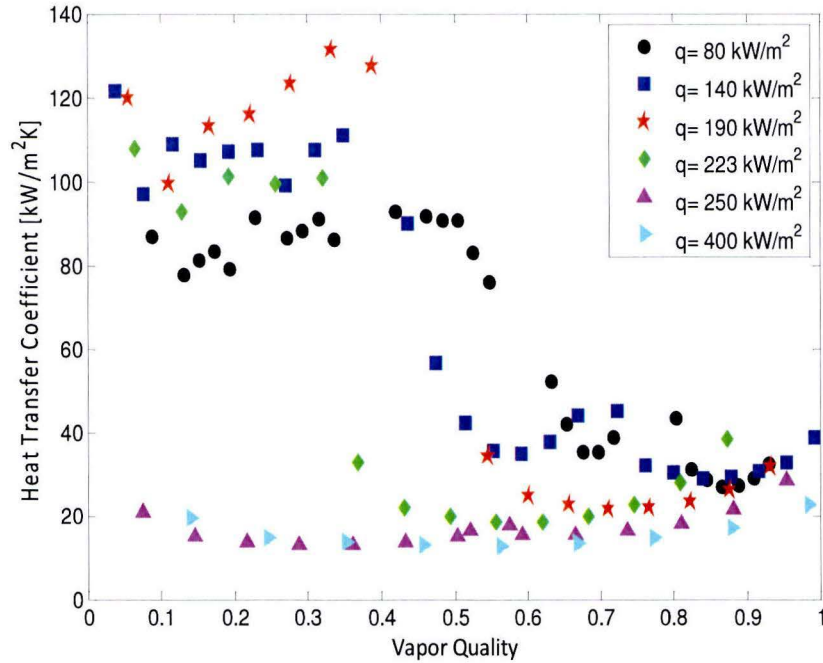
Figure 6.12 Heat Transfer Coefficient at G=1500 kg/m^{2}s, T_{sat}=22 °C, D_h=0.5 mm

The pool boiling correlation of Cooper [39] (i.e. in the study of Gungor and Winterton [40]) or modified Cooper correlation (i.e. in the study of Thome et al. [42]), has been used to calculate the nucleate boiling heat transfer contribution in several previous studies. For a surface roughness of 1.0 μm, the equation of Cooper [39] is given as:

$$h_{\text{Cooper}} = 55 * P_r^{0.12}(-0.4343\ln P_r)^{-0.55}M^{-0.5}q^{0.67} \tag{6.6}$$

As it is seen from the Equation 6.6, it is a function of reduced pressure (P_r) which is the ratio of the saturation pressure to critical pressure, molecular weight (M) and heat flux (q). The correlation covers reduced pressures from 0.001 to 0.9 and molecular weights from 2 to 200 g/mol. The suppression factor, S, is introduced as a multiplication factor for nucleate boiling contribution. The suppression factor is modeled based non-dimensional numbers such as Re$_l$, Bo, Martinelli parameter etc. The modeling approach is not the same in available studies. For example, in the model of Gungor and Winterton [40], the suppression factor is a function of enhancement factor (E) and Re$_l$ where enhancement factor includes Boiling number and Martinelli parameter. On the other hand, in the model of Liu and Winterton [43], the suppression factor is a function of a factor of enhancement factor (contains Prandtl number, vapor quality, density ratio of liquid to vapor) and Boiling number. Those formulations can be found in Table 6.1. It can be said that nucleate boiling is calculated from the pool boiling with a modification factor and can be given as

$$h_{\text{nb}} = Sh_{\text{Cooper}} \tag{6.7}$$

For illustration, Cooper correlation [39] is used to show the nucleate boiling contribution without any suppression factor. The reason of not including suppression factor lies under the fact that the suppression factor models are different from each model and do not have common non-dimensional numbers. Therefore, it is wise to see the pool boiling effect without considering complex and uncommon suppression factors for simplicity. The suppression factor of each correlation is included within the analyses when experimental data is compared to existing two-phase heat transfer models in Section 6.4. The ratio of Cooper`s prediction to experimental data is plotted along the vapor quality and results are shown in Figure 6.13. All the experimental data is predicted with a mean average error of 21.72% and mean relative error of -2.21%. The results indicate that nucleate boiling contribution is dominant compared to convective boiling contribution. According to Cooper`s nucleate boiling correlation [39], the nucleate boiling heat transfer coefficient is a function of reduced pressure as it is seen from Equation 6.6. The reduced pressure is dependent on saturation temperature such a way that the increase of saturation temperature results in enhanced reduced pressure. This means nucleate boiling heat transfer contribution is augmented at high saturation temperatures. Indeed, the saturation temperature of 22 °C for CO_2 is quite high since the critical temperature of CO_2 is only 31.1 °C. Therefore, it is not surprising to observe nucleate boiling heat transfer domination over convective boiling heat transfer. Some over and under predictions are present within the same heat flux conditions of different mass fluxes as seen in Figure 6.13. These differences will be explained in Section 6.4.
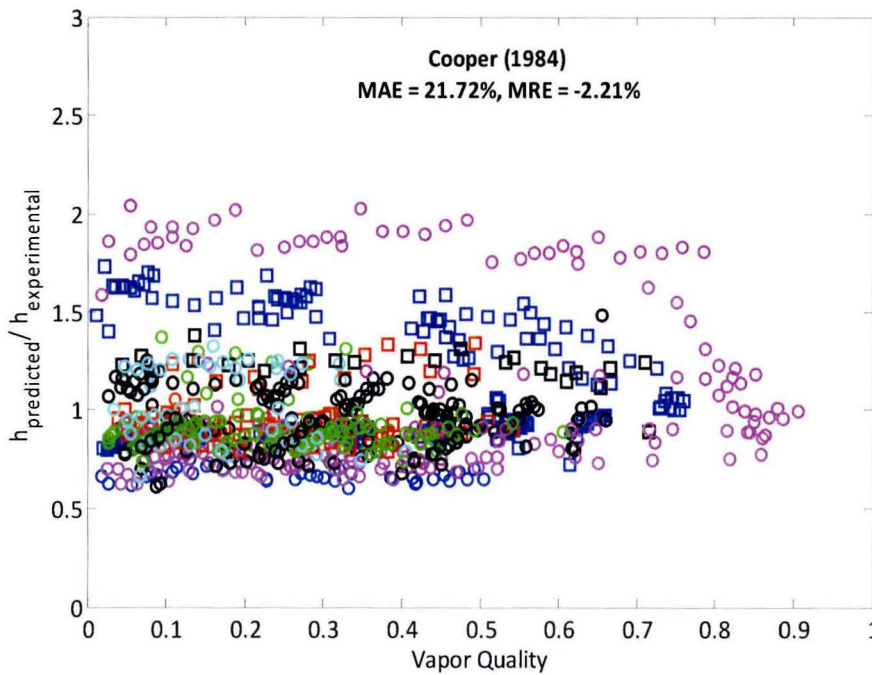
Figure 6.13 Comparison of Experimental Heat Transfer Coefficient with Cooper's Pool Boiling Correlation [39]

6.3 The Effect of Channel Hydraulic Diameter

The effect of hydraulic diameter on two-phase heat transfer coefficient is illustrated from Figure 6.14 to Figure 6.16. Generally, it is observed that smaller hydraulic diameter leads to a higher two-phase heat transfer coefficient as explained below.

At the low quality region, smaller tube diameter shows higher two-phase heat transfer coefficient. This is due to the fact that the nucleate boiling suppression factor and convective boiling heat transfer coefficient are enhanced with smaller diameter. This can be checked from heat transfer equations of Cheng et al. [14] in Table 6.1. For example, Maqbool et al. [44] reports that the higher heat transfer coefficient in small diameter may be due to the thinner liquid film inside the wall which can enhance the heat transfer compared to the larger diameter channel. In addition, it is observed that the dryout quality is lower for the smaller diameter tube. This can be explained by smaller liquid thickness of 0.5 mm sample compared to 1.5 mm sample. The smaller liquid thickness may lead to early dryout patches to arrive since the liquid film break-up easily. Higher CO_2 two-phase heat transfer coefficient of smaller diameter and early dryout cases are also reported by Choi et al. [30] and Yun and Kim [45].

Even though the small effect of tube diameter on CO_2 heat transfer could be explained by nucleate boiling effects, this explanation is not sufficient to clarify the high heat transfer coefficient at smaller diameters. For instance, some other differences can exist between the two samples besides the hydraulic diameter of the channels. A possible difference is the surface conditions because the nucleate boiling contribution to flow boiling heat transfer can be influenced by different surface conditions. For example, the pool boiling heat transfer coefficients increase with the increase of surface roughness according to pool boiling correlations presented by Gorenflo [46]. Therefore, more detailed surface conditions are needed to investigate the channel diameter effect.

The post dryout heat transfer coefficients are still higher for smaller hydraulic diameter case but with a less pronounced enhancement compared to pre-dryout heat transfer values. This is illustrated in Figure 6.16. A limited literature study is available for CO_2 post-dryout heat transfer coefficients. The most recent post dryout heat transfer correlation is given by Cheng et al. [42] as:

$$h_{\text{mist}} = 2 * 10^{-8} \text{Re}_{\text{H}}^{1.97} \text{Pr}_{\text{V}}^{1.06} Y^{-1.83} \left(\frac{k_{\text{V}}}{D_{\text{eq}}} \right) \tag{6.8}$$

Where the homogeneous Reynolds number Re_{H} and the correction factor Y are calculated as follows:

$$\text{Re}_{\text{H}} = \frac{G D_{\text{eq}}}{\mu_{\text{V}}} \left[x + \frac{\rho_{\text{V}}}{\rho_{\text{L}}} (1 - x) \right] \tag{6.9}$$

$$Y = 1 - 0.1 \left[\left(\frac{\rho_{\text{L}}}{\rho_{\text{V}}} - 1 \right) (1 - x) \right]^{0.4} \tag{6.10}$$

According this equation, the larger diameter should have higher heat transfer coefficient in the region of mist flow pattern. However, in the current experimental results, mostly smaller diameter has higher heat transfer coefficient than the larger diameter. This might be due to surface roughness effects as explained previously. Moreover, the flow pattern should be validated before making comparison with experimental data and correlation by Cheng et al. [42].
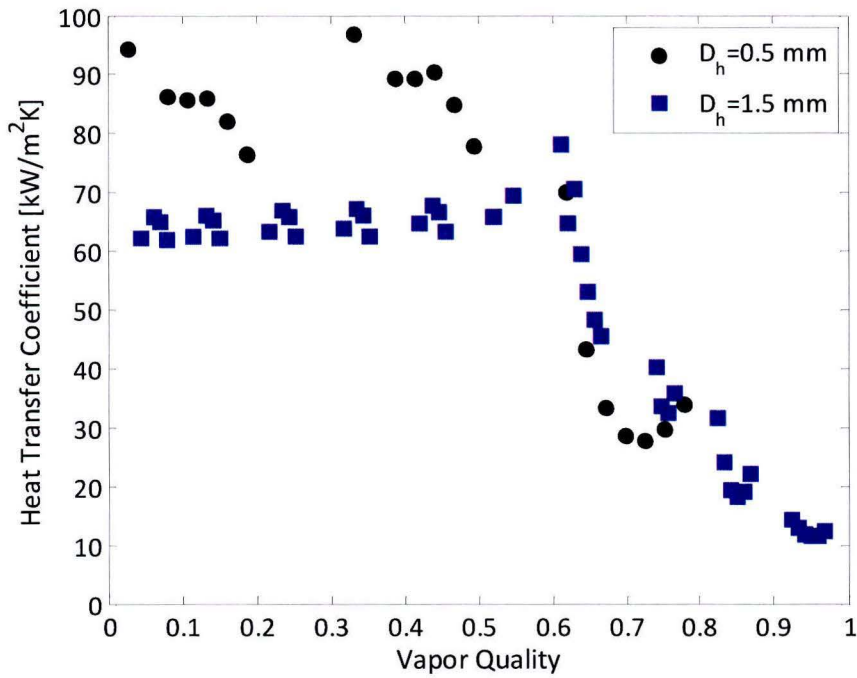
Figure 6.14 Heat Transfer Coefficient at G=1200 kg/m^{2}s, q=75 kW/m^2
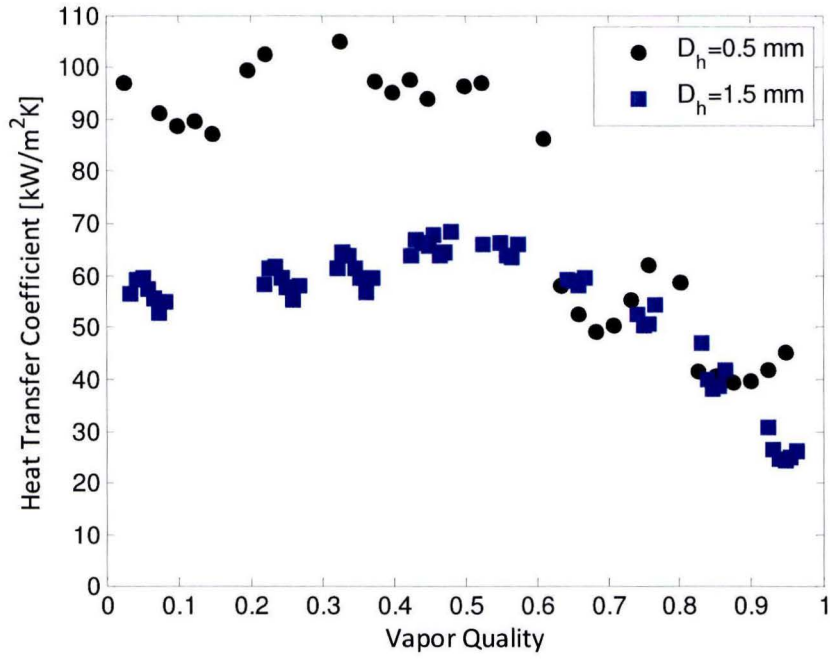
Figure 6.15 Heat Transfer Coefficient at *G*=1700 kg/m²s, *q*=90 kW/m²
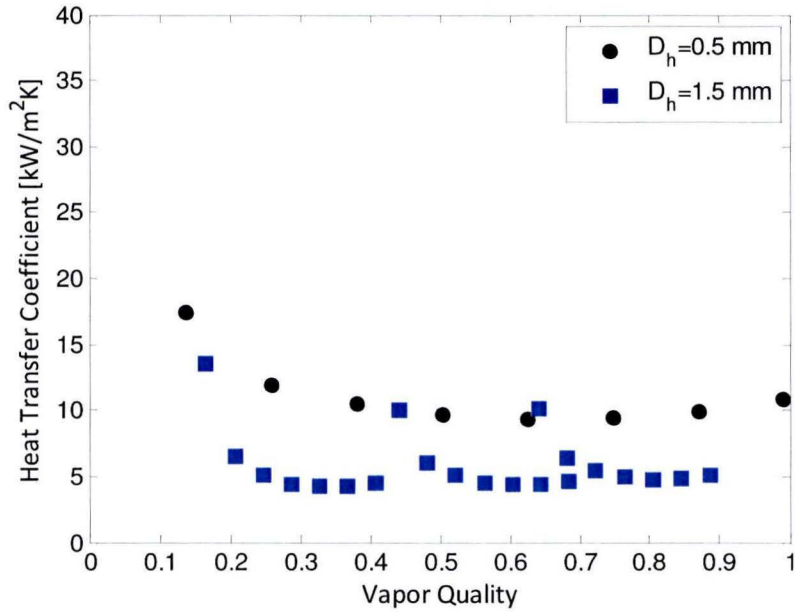
Figure 6.16 Heat Transfer Coefficient at *G*=500 kg/m²s, *q*=150 kW/m²

6.4   Comparison of Pre-Dryout Experimental Results with Existing Prediction Methods

Several empirical correlations are selected from open literature to estimate the best correlation for predicting the current experimental data. The trends of the correlations for two sets of current experimental data are shown in Figure 6.17 and Figure 6.18. As it is seen, each correlation has different trend and none of them is accurate enough to predict the experimental data. All of these correlations are given in Table 6.1 with their corresponding formulas. Most of the correlations are originally developed for conventional refrigerants at temperatures higher than -30 °C. Among those studies, the correlation of Yoon et al. [10] and Cheng et al. [14] are developed for only CO_2. The correlation of Yoon et al. [10] is not included in comparisons since the model uses critical vapor quality prediction before processing with the heat transfer correlations. This equation is left to be analyzed during critical vapor quality prediction in Chapter 7. Indeed, it is shown that critical vapor quality is over-predicted with an order of magnitude difference which leads to poor predictions of heat transfer coefficients. The detailed explanations related to critical vapor quality prediction of Yoon et al. [10] can be found in Chapter 7. The correlation of Cheng et al. [14] is based on a heat transfer model associated with flow patterns and it is not purely empirical.
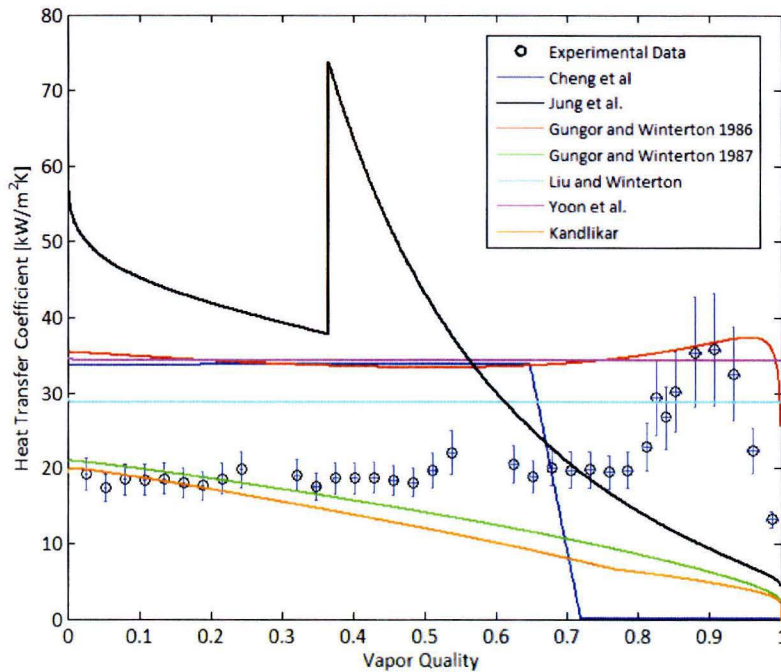
Figure 6.17 Comparison of Two- Phase Heat Transfer Correlations with Experimental Data at q=40 kW/m², G=200 kg/m²s, D_h=1.5 mm
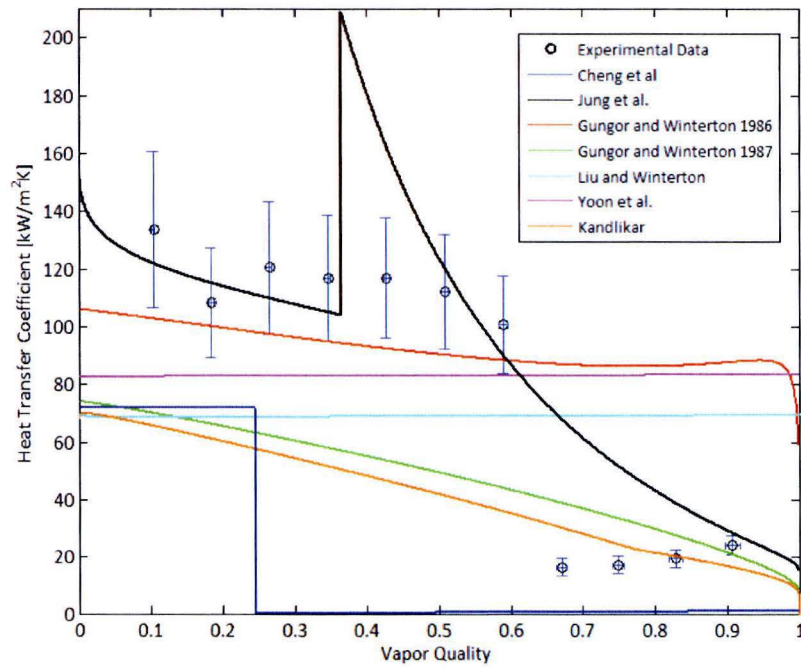
Figure 6.18 Comparison of Two- Phase Heat Transfer Correlations with Experimental Data at *q*=140 kW/m², *G*=700 kg/m²s, *D*ₕ=0.5 mm

Table 6.1 Some Two-Phase Heat Transfer Correlations in Open Literature

Gungor and Winterton ([40]-[41])	$h_{tp} = Eh_l + Sh_{nb}$ $S = 1/(1 + 1.15 \times 10^{-6} E^2 Re_l^{1.17})$ $E = 1 + 2.4 \times 10^4 Bo^{1.16} + 1.37 \times (1/X_{tt})^{0.86}$ $X_{tt} = \left(\frac{\mu_l}{\mu_v}\right)^{1/8} \left(\frac{1-x}{x}\right)^{7/8} \left(\frac{\rho_v}{\rho_l}\right)^{1/2}$, $h_l = 0.023 \frac{k_l}{D_h} Re_l^{0.8} Pr_l^{0.4}$, $Re_l = \frac{(1-x)GD_h}{\mu_l}$, $Pr_l = \frac{c_{pl}\mu_l}{k_l}$, $Bo = \frac{q}{Gh_{lv}}$ $h_{nb} = 55 * P_r^{0.12}(-0.4343 \ln P_r)^{-0.55} M^{-0.5} q^{0.67}$ Gungor & Winterton 1987: $h_{tp}^* = E^* \times h_l$, $E^* = 1 + 3000 Bo^{0.86} + 1.12 \left(\frac{x}{1-x}\right)^{0.75} \left(\frac{\rho_l}{\rho_v}\right)^{0.41}$
Jung et al. [51]	$h_{tp} = Eh_l + Sh_{nb}$ $h_{nb} = 207 \left(\frac{k_l}{b_d}\right) \left(\frac{qb_d}{k_f T_{sat}}\right)^{0.745} \left(\frac{\rho_v}{\rho_l}\right)^{0.581} Pr_l^{0.533}$ $b_d = 0.0146 \times 35 \times (2\sigma/g(\rho_l - \rho_v))^{0.5}$, $E = 2.37(0.29 + 1/X_{tt})^{0.85}$ When $X_{tt} < 1$, $S = 4048 X_{tt}^{1.22} Bo^{1.13}$ When $1 \leq X_{tt} \leq 5$, $S = 2 - 0.1 X_{tt}^{-0.28} Bo^{-0.33}$
Kandlikar [50]	$h_{cb} = (1.1360 Co^{-0.9} + 667.2 Bo^{0.7} F_{fl}) h_l$ $h_{nb} = (0.668 Co^{-0.2} + 1058 Bo^{0.7} F_{fl}) h_l$; h_{tp} is the larger of h_{cb} and h_{nb} $Co = \sqrt{\dfrac{\sigma}{(D_h)^2 g(\rho_l - \rho_v)}}$
Liu and Winterton [43]	$h_{tp} = \sqrt{(Fh_l)^2 + (Sh_{nb})^2}$ $F = \left(1 + x Pr_l (\frac{\rho_l}{\rho_v} - 1)\right)^{0.35}$ $S = (1 + 0.055 F^{0.1} Re_l^{0.16})^{-1}$
Yoon et al. [10]	$x_{cr} = 0.0012 Re_l^{2.79} (1000 Bo)^{0.06} Bd^{-4.76}$ When $x < x_{cr}$, $h_{tp} = \sqrt{(Eh_l)^2 + (Sh_{nb})^2}$ $S = 1/(1 + 1.62 \times 10^{-6} E^{0.69} Re_l^{1.11})$, $E = \left[1 + 9.36 \times 10^3 x Pr_l \left(\frac{\rho_l}{\rho_v}\right) - 1\right]^{0.11}$ When $x < x_{cr}$, $h_{tp} = (\theta_{dry} \times h_v + (2\pi - \theta_{dry}) Eh_l)/2\pi$ $E = 1 + 3000 Bo^{0.86} + 1.12(x/(1-x))^{0.75} (\rho_l/\rho_v)^{0.41}$, $\theta_{dry}/2\pi = 36.23 \times Re^{3.47} Bo^{4.84} Bd^{-0.27} (1/X_{tt})^{2.6}$, $Bd = \frac{(\rho_l - \rho_v)g D_h^2}{\sigma}$
Cheng et al. [14]	$h_{tp} = \frac{\theta_{dry} h_{vapor} + (2\pi - \theta_{dry}) h_{wet}}{2\pi}$, $h_{vapor} = 0.023 (Re_V)^{0.8} (Pr_V)^{0.4} \frac{k_V}{D_{eq}}$, $h_{wet} = \left[(Sh_{nb,CO_2})^3 + h_{cb}^3\right]^{1/3}$ $h_{nb} = 131 P_r^{-0.0063} (-\log_{10} P_r)^{-0.55} M^{-0.5} q^{0.58}$, $h_{cb} = 0.0133 Re_\delta^{0.69} Pr_L^{0.4} \frac{k_L}{\delta}$, $Re_\delta = \frac{4G(1-x)\delta}{\mu_L(1-\epsilon)}$, $Re_V = \frac{GD_{eq}}{\mu_V} \frac{x}{\epsilon}$ If $x < x_{IA}$, $S = 1$; If $x \geq x_{IA}$, $S = 1 - 1.14 \left[\frac{D_{eq}}{0.0073}\right]^2 \left[1 - \frac{\delta}{\delta_{IA}}\right]^{2.2}$, $\delta = \frac{D_{eq}}{2} - \left[\left(\frac{D_{eq}}{2}\right)^2 - \frac{2A_L}{(2\pi - \theta_{dry})}\right]^{1/2}$ $x_{IA} = \left[1.8^{(1/0.875)} \left(\frac{\rho_V}{\rho_L}\right)^{-1/1.75} \left(\frac{\mu_L}{\mu_V}\right)^{-1/7} + 1\right]^{-1}$, In annular, intermittent and bubbly flows, $\theta_{dry} = 0$

First, the early dryout experimental data (before vapor quality of 0.2) are disregarded from database since those data represent the post dryout heat transfer coefficients. Then, the ratios of the predicted heat transfer coefficient to the experimental pre-dryout heat transfer coefficient are plotted along the vapor qualities. Afterwards, a statistical analysis is made to select the best prediction equation that catches the trends of experimental data. It should be noted that the surface roughness is not considered during the comparisons since most of the correlations are developed with a fixed surface roughness (1 μm). In addition, the errors due to flow conditions at the test section entry region, such sharp bends or flow disturbances and fluctuations are not quantified and may partly be responsible for the differences between existing correlations and experimental conditions.

Figure 6.19-Figure 6.23 show the comparison of the experimental data with theory and illustrate the deviation trends and statistical analysis. Table 6.2 lists statistical analysis of some test conditions as well as overall statistical results with the mean average error and the mean relative error values. Before commenting on the comparison of the test data with two-phase heat transfer correlations, it is reminded that nucleate boiling contribution is much larger than the corresponding convective boiling contribution for the current test conditions as it is investigated in Section 6.1 and Section 6.2. Therefore, it is expected that the two-phase heat transfer model that has the largest contribution in nucleate boiling part will show better prediction results.

The correlations of Kandlikar [50], Gungor and Winterton [40] and Jung et al. [51] show a decreasing tendency of heat transfer coefficient with respect to quality. Prediction analyses of correlations show that equations by Kandlikar [50] and Gungor and Winterton [40] mostly underpredict the experimental data. The reason of underprediction of the test results is due to the fact that those models are based on the intensification of the liquid heat transfer mechanism with a modification factor. However, it is already shown that convective boiling contribution that is based on liquid heat transfer mechanism has little contribution to two-phase heat transfer of this study. Therefore, intensification type models suggest smaller two-phase heat transfer values than the test results. It is seen in Figure 6.23 that the model of Jung et al. [51] mostly overpredicts the current test data. In addition, superposition type Jung et al. [51] model has over-predictions at moderate vapor qualities for some test cases. Indeed, the suppression factor (S) of correlation by Jung et al. [51] contributes to a high deviation with the current experimental data at moderate vapor qualities. This is due to the fact that the jump in the suppression factor with the vapor quality leads to an extremely high nucleate boiling contribution. For instance suppression factor jumps from 1 to 2.5 at $q=240kW/m^2$, $G=1200$ kg/m^{2}s, $D_h= 0.5$ mm at vapor quality of 0.36. The deviation trends of those correlation from experimental data reflects itself as high numbers of mean average error and mean relative error. Apparently, superposition model of Jung et al. [51] and intensification models of Kandlikar [50] and Gungor and Winterton [40] are not good enough to catch the trends of current experimental data as explained above. Among the two-phase heat transfer correlations implemented so far, the correlation of Cheng et al. [14] and correlation of Liu and Winterton [43] take into account the nucleate boiling and convective boiling contribution together with an asymptotic approach.

They illustrate the good statistical results and similar trends of prediction over the pre-dryout vapor quality. The main reason of good predictions is due to dominancy of nucleate boiling term that is based

64

on Cooper's nucleate boiling equation in both equations. Actually, the nucleate boiling heat transfer is particularly modified for CO_2 from the original Cooper's pool boiling correlation [39] in the two-phase heat transfer model of Cheng et al. [14]. That modification can be seen in Equation 6.6.[49]

$$h_{nb,CO_2} = 0.71 h_{nb,Cooper} + 3970 \qquad (6.11)$$

The correlation of Cheng et al. [14] has relatively better statistical results compared to the model of Liu and Winterton [43]. The main difference between Liu and Winterton correlation [43] and Cheng et al. correlation [14] is that Liu and Winterton correlation [43] is based on a database with much more refrigerants that have different physical properties than CO_2 while Cheng et al. correlation [14] is unique for CO_2. Moreover, Cheng et al. [14] database includes some test conditions close to current study. (i.e. includes 20 °C saturation data of CO_2) and catches the drop of heat transfer coefficient at critical vapor quality. It has also room for improvement in dryout quality prediction and post dryout heat transfer coefficient predictions. On the other hand, Liu and Winterton correlation [43] does not catch the drops of heat transfer coefficient with increase of vapor quality as seen in Figure 6.17 and Figure 6.18. As a final remark, it should be emphasized that improving the model of Cheng et al. [14] requires much more effort since that model is based on flow pattern identification and detailed void fraction and liquid film thickness estimations. In contrast, Liu and Winterton model [43] can be modified by correlating the enhancement and nucleate boiling suppression factors with non-linear regression method which requires less effort to do so.

In conclusion, asymptotic models show better predictions than superposition and intensification models. Among the implemented correlations, the correlation by Cheng et al. [14] is found out to be the best correlation in terms of catching the trends of experimental two-phase heat transfer coefficient and taking into account both convective heat transfer and nucleate boiling heat transfer contribution with the best statistics. Yet, it still needs to be modified for the current database since the original database is limited up to certain saturation temperature, mass flux and heat flux conditions. Further improvements of the model require modifying nucleate boiling suppression factor and convective boiling enhancement factor. For example, the value of nucleate boiling suppression factor is dependent on the intermittent to annular vapor quality as can be seen in Cheng et al. [14] model of Table 6.1. In the original equation that quality is fixed and only dependent on saturation temperature. From the flow visualization study in Chapter 5, it is found out that intermittent to annular vapor quality is not the same as the original equation and changing with mass flux as it can be seen in Figure 5.10. One of the things that are left as a future study is to modify intermittent to annular critical quality to improve nucleate boiling suppression factor. Then a regression analysis can be performed to find the coefficients of suppression equation to predict the current heat transfer coefficient. Furthermore, it is not clear for some studies which are included in their database that the existence of a mal-distribution and large pressure fluctuation in multi-tubes are taken into account during two-phase heat transfer coefficient calculation. Because, large fluctuations may yield the differences of heat transfer coefficients between microchannels and single tubes even though the tests are conducted at similar operating conditions.
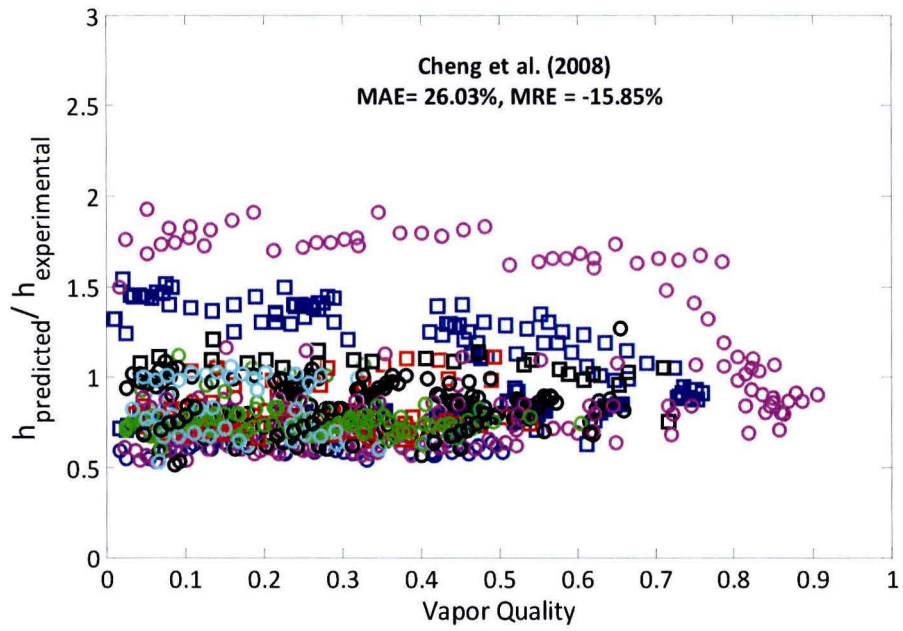
Figure 6.19 Comparison of Experimental Heat Transfer Coefficient with Correlation of Cheng et al. [14]
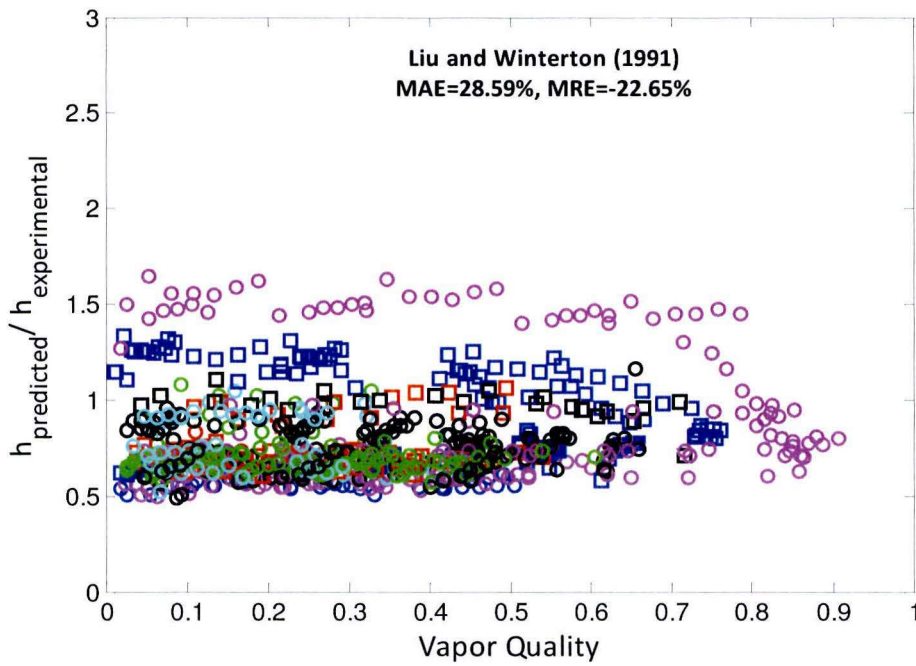
Figure 6.20 Comparison of Experimental Heat Transfer Coefficient with Correlation of Liu and Winterton [43]
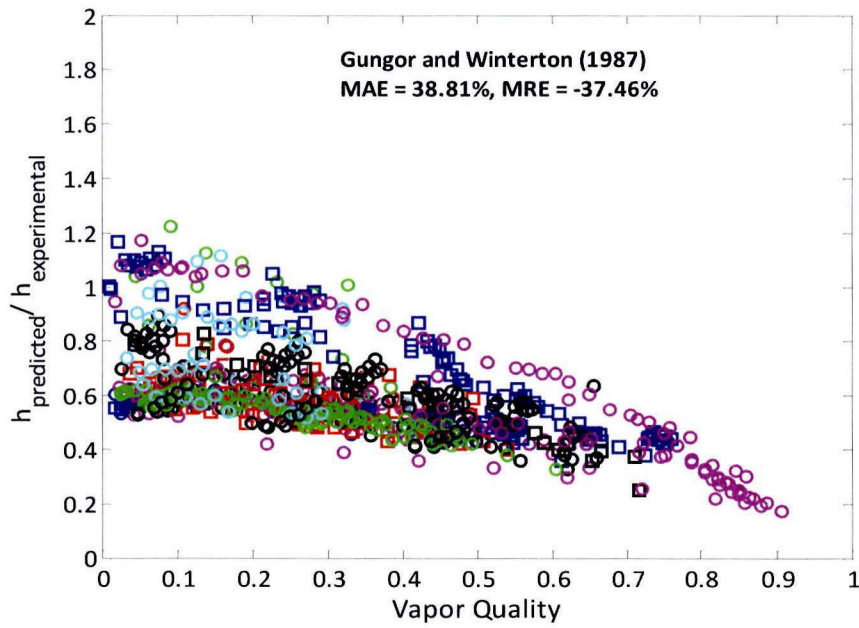
Figure 6.21 Comparison of Experimental Heat Transfer Coefficient with Correlation of Gungor and Winterton [40]
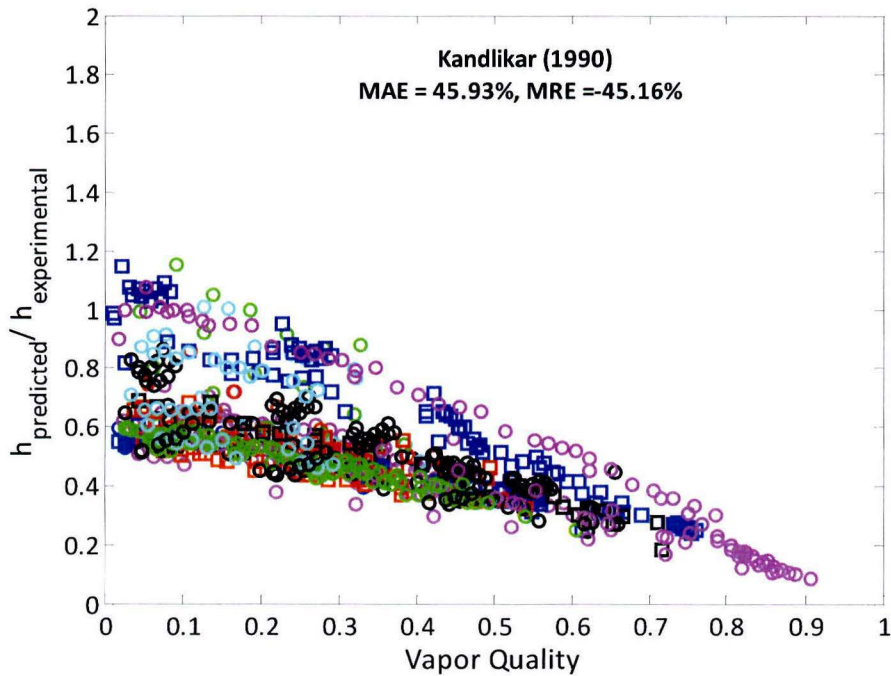
Figure 6.22 Comparison of Experimental Heat Transfer Coefficient with Correlation of Kandlikar [50]
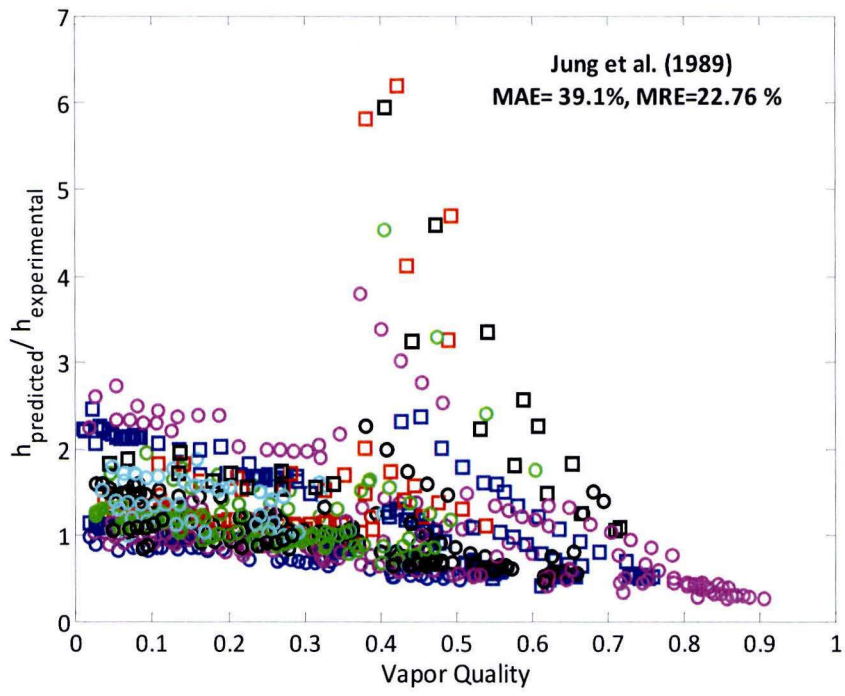
Figure 6.23 Comparison of Experimental Heat Transfer Coefficient with Correlation Jung et al. [51]

Table 6.2 Mean Average and Mean Relative Deviation between Available Correlations and Experimental Data

Test Conditions			Cooper [39]		Cheng et al. [14]		Liu & Winterton [43]		Gungor &Winterton [40]		Kandlikar [50]		Jung et al. [51]	
q	G	D_h	MAE	MRE	MAE	MRE	MAE	MRE	MAE	MRE	MAE	MRE	MAE	MRE
(kW/m²)	(kg/m²)	(mm)	(%)	(%)	(%)	(%)	(%)	(%)	(%)	(%)	(%)	(%)	(%)	(%)
40	200	1.5	76.89	76.86	66.53	65.02	46.19	42.55	32.28	-27.61	40.22	-39.63	108.16	83.56
75	900	1.5	42.24	40.11	31.18	24.34	20.14	9.45	21.87	-18.35	29.60	-27.70	59.71	43.16
90	200	1.5	23.70	21.87	10.93	5.66	6.63	-2.22	43.94	-43.94	55.20	-55.20	154.74	154.74
130	1300	1.5	13.67	-13.67	26.89	-26.89	33.79	-33.79	45.43	-45.43	50.56	-50.57	12.17	2.56
140	700	1.5	10.54	-10.54	25.11	-25.11	30.75	-30.75	49.63	-49.63	56.37	-56.37	33.43	33.43
200	1700	1.5	2.82	-1.94	19.95	-19.95	25.96	-25.96	30.98	-30.98	35.50	-35.50	34.82	34.82
80	1200	0.5	32.72	-32.72	40.11	-40.11	44.71	-44.71	46.55	-46.55	51.61	-51.61	24.42	-24.42
100	500	0.5	24.66	-24.66	34.56	-34.56	38.64	-38.64	54.94	-54.94	62.23	-62.23	16.54	-3.75
100	1200	0.5	22.32	-22.32	32.27	-32.27	36.62	-36.62	41.36	-41.36	48.39	-48.39	14.27	-14.27
140	900	0.5	29.69	-29.69	40.71	-40.71	43.56	-43.56	46.15	-46.15	51.70	-51.70	14.15	-0.97
200	1500	0.5	12.58	-11.06	26.98	-26.98	29.27	-29.27	27.43	-27.43	34.20	-34.20	21.62	20.47
240	1200	0.5	22.25	22.25	4.82	-1.80	5.39	-3.11	5.90	0.2474	11.09	-11.06	71.25	71.25
Overall Experimental Data (n= 60)			21.72	-2.21	26.03	-15.85	28.59	-22.65	38.81	-37.46	45.93	-45.16	39.1	22.76

$$Error,\ \varepsilon_n = \left(\frac{x_{predicted,n} - x_{experimental,n}}{x_{experimental,n}}\right)\ ;\quad Mean\ Relative\ error\ (MRE),\ \bar{\varepsilon} = \frac{1}{N}\sum_{n=1}^{N}\varepsilon_n\ ;\quad Mean\ absolute\ error\ (MAE),\ |\bar{\varepsilon}| = \frac{1}{N}\sum_{n=1}^{N}|\varepsilon_n|$$

This page is intentionally left blank.

7 NEW DRYOUT PREDICTION CORRELATION DEVELOPMENT

The determination of the critical quality is essential in order to develop a heat transfer coefficient correlation since the heat transfer curve trends show two different characteristics before and after the critical quality. Those two regions can be modeled separately and the two separate correlations can be superposed to capture the general trend of the heat transfer coefficient variation.

Dryout conditions are dependent on mass flux, heat flux, hydraulic diameter and saturation temperature. In the present dryout data, saturation temperature effect is not significant since all the measurements are done around 22 °C evaporation temperature. The experimental results in Section 6.2 show that increasing the heat flux reduces the critical vapor quality. Although mass flux effect is not as dominant as heat flux effect, it has still an influence on the dryout vapor quality. At e few test conditions, it is seen that increase of the mass flux slightly reduces the dryout quality until a transition mass flux (See Figure 6.3). After the transition mass flux, critical vapor quality increases with the rise of mass flux especially at high heat fluxes. It is explained in the study of Yun and Kim [5] that as the mass flux increases beyond a transition mass flux, more liquid droplet entrainment occurs. However, excessive liquid droplets in the vapor core also increase liquid droplet deposition to liquid film layer and dryout patch regions. These trends improve the probabilities that the dryout patches are rewetted and dryout of liquid film is prevented. Since mass flux effect on dryout is not pronounced (See Chapter 6, Figure 6.3) so that the increasing trend of the dryout quality with mass flux is not taken into account during correlation development. It is usually observed that smaller diameter (0.5 mm) channel has earlier dryout quality than the large diameter channel (1.5 mm) (i.e. Figure 6.14 and Figure 6.15). This can be explained by thinner liquid film thickness of the smaller diameter channel that favors the early dryout condition such a way that more active nucleate boiling causes dryout patches to appear earlier. Choi et al. [30] also reported similar results. In this chapter, existing dryout correlations are compared with the experimental dryout qualities. Then, a new correlation is proposed based on a modification of the model by Cheng et al. [14] as explained below.

7.1 Comparison of Experimental Data with Dryout Correlations

During a correlation development, all dryout experimental data are plotted against dryout prediction data by several correlations that are summarized in Table 7.1. The details of those equations can be found in Chapter 2. Ducoulombier et al. [17] suggests using Cheng [14] type correlation for high saturation temperatures and high heat flux test conditions. Present experimental data consist of much higher saturation temperature and heat flux conditions than their experimental conditions. For that reason, the dryout inception equation of Ducoulombier et al. [17] is taken as Cheng [14] type correlation. In the analysis, the experimental dryout qualities less than 0.1 are not included since the actual dryout point is doubtful due to very early dryout inception.

Table 7.1 CO$_2$ Dryout Prediction Models

Dryout Prediction Models	Formula	Database of the Model	Remarks
Yoon et al. [10]	$$x_{\text{dryout}} = 0.0012\text{Re}_{\text{lo}}^{2.79}(1000\text{Bo})^{0.06}\text{Bd}^{-4.76}$$ $$\text{Bd} = \frac{(\rho_l - \rho_v)gD_h^2}{\sigma}$$ $$\text{Re}_{\text{lo}} = \frac{GD_h}{\mu_l} \quad \text{Bo} = \frac{q}{h_{\text{lv}}G}$$	T_{sat} : -4 to 20 °C D=7.53 mm G=200 to 530 kg/m^{2}s q = 12 to 20 kW/m^2	Only for CO$_2$ Empirical Based Model
Jeong and Park [12]	$$x_{\text{dryout}} = 6.2\text{Re}_{\text{lo}}^{-0.5}\text{Bo}^{-0.2}\text{Bd}^{-0.45}$$	T_{sat} : 5 and 10 °C D=0.8 mm G=400 to 800 kg/m^{2}s q = 12 to 18 kW/m^2	Correlation based on Yoon [10]
Tang et al. [13]	$$x_{\text{dryout}} = 1.297\text{Re}_l^{-0.242}\text{Bo}^{-0.107}\text{Bd}^{0.00095}\left(\frac{\rho_v}{\rho_l}\right)^{0.000090}\left(\frac{\mu_l}{\mu_v}\right)^{1.122}$$	T_{sat} : 1 to 15 °C D=1.7 mm G=100 to 600 kg/m^{2}s q = 1.67 to 8.33 kW/m^2	Correlation based on Yoon [10], with added density and viscosity ratios
Cheng et al. [14]	$$x_{\text{di}} = 0.58\exp\left[0.52 - 0.236\text{We}_v^{0.17}\text{Fr}_{v,\text{Mori}}^{0.17}\left(\frac{\rho_v}{\rho_l}\right)^{0.25}\left(\frac{q}{q_{\text{crit}}}\right)^{0.27}\right]$$ $$We_v = \frac{G^2 D_{\text{eq}}}{\rho_v \sigma}$$ $$\text{Fr}_{v,\text{Mori}} = \frac{G^2}{\rho_v(\rho_l - \rho_v)gD_{\text{eq}}}$$ $$q_{\text{crit}} = 0.131\rho_v^{0.5}h_{\text{lv}}[g\sigma(\rho_l - \rho_v)]^{0.25} \text{ by Kutateladze [16]}$$	T_{sat} : -28 to 25°C D=0.6 to 10 mm G=50 to 1500 kg/m^{2}s q = 1.8 to 46 kW/m^2	Only for CO$_2$ Flow Pattern Based Model
Ducoulombier et al. [17]	$$x_{\text{di}} = 1 - 338\text{Bo}^{0.703}P_r^{1.43} \quad (1)$$ $$x_{\text{di}} = 0.58\exp\left[0.52 - 0.236\text{We}_v^{0.17}\text{Fr}_{v,\text{Mori}}^{0.17}\left(\frac{\rho_v}{\rho_l}\right)^{0.25}\left(\frac{q}{q_{\text{crit}}}\right)^{0.27}\right] \quad (2)$$	T_{sat} : -10,-5 and 0°C D=0.529 mm G=200 to 1200 kg/m^{2}s q = 10 to 30 kW/m^2	(1) -10,-5 and 0°C(10kW/m^2) (2) 0°C (30 kW/m^2)
Mastrullo et al. [18]	$$x_{\text{pred}} = 1 - \left(c_0 q^{c_1} G^{(2c_2-c_1-1)}D_{\text{eq}}^{(c_2-1)}(d_0 + d_1 P_r + d_2 P_r^2)P_r^{c_3}\right)$$	T_{sat} : 7 and 12 °C D=6 mm G=150 to 500 kg/m^{2}s q = 5 to 20 kW/m^2	Only for CO$_2$ Regression coefficients are given in Chapter 2

First, the applicability of the equations that are shown in Table 7.1 is studied. The correlations are estimated in terms of mean absolute deviation, mean average deviation and standard deviation. The definitions can be found in Section 10.4 of Appendix.

Table 7.2 depicts the statistical comparison of the available correlations to the experimental data. Generally, the correlations shown in Table 7.1 underpredicted the experimental data as shown in Figure 7.1-Figure 7.3. The correlations given by Yoon [10] and Tang [13] give order of difference in magnitude in predictions and they cannot capture the trends of change in the dryout quality with heat flux and mass fluxes. Therefore, they are assigned as poor prediction equations for the current experimental database. The correlations by Mastrullo et al. [18], Cheng et al. [14] and Jeong et al. [12] relatively give good statistical results, but Mastrullo et al. [18] cannot capture the dryout quality change with mass flux. Overall, Cheng et al. [14] come out best in terms of having good statistical results and catching the dryout trends with changing heat flux and mass flux. In addition, the model of Cheng et al. [14] is not purely empirical and it has a physical approach to explain the relationship between flow patterns, heat transfer coefficient and pressure drop. Moreover, it allows modifying the original heat transfer coefficient and frictional pressure drop equations for current experimental data. Therefore, it is chosen as the basic equation that is to be developed.

Table 7.2 Statistical Analysis of the Dryout Quality Predictions from the Selected Methods

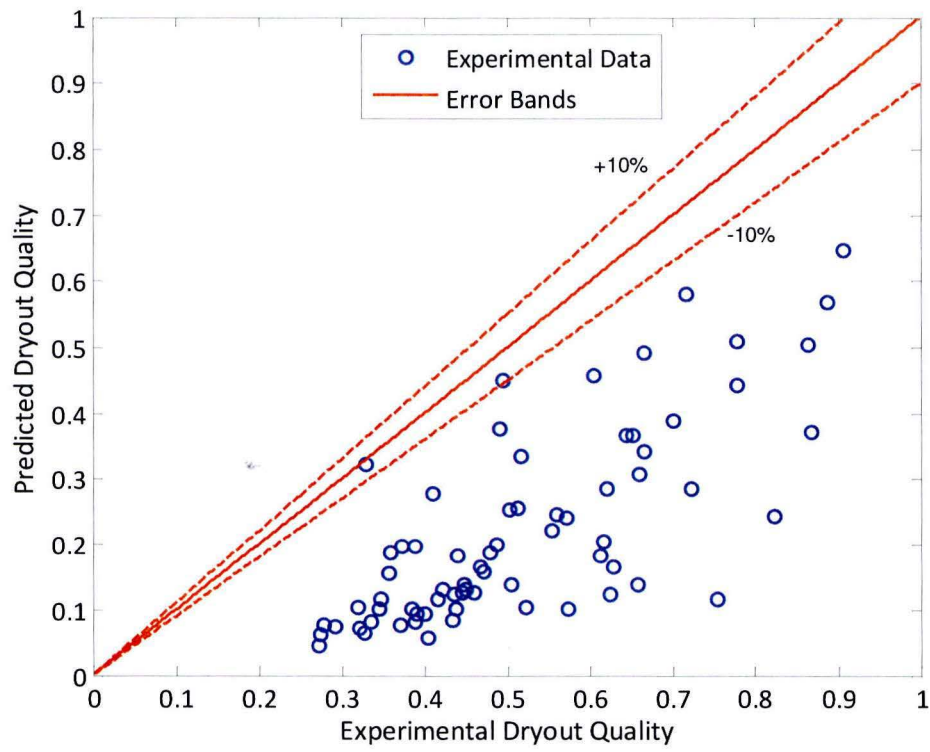| Prediction Method	Mean Relative Error (%)	Mean Absolute Error (%)	Standard Deviation (%)
Yoon et al. [10]	4.1×10^9	4.1×10^9	4.1×10^9
Jeong and Park [12]	-71.96	71.96	124.80
Cheng et al. [14]	-59.53	59.53	112.49
Mastrullo et al. [18]	-109.47	118.31	162.067
Tang et al. [13]	1.6×10^{10}	1.6×10^{10}	1.6×10^{10}

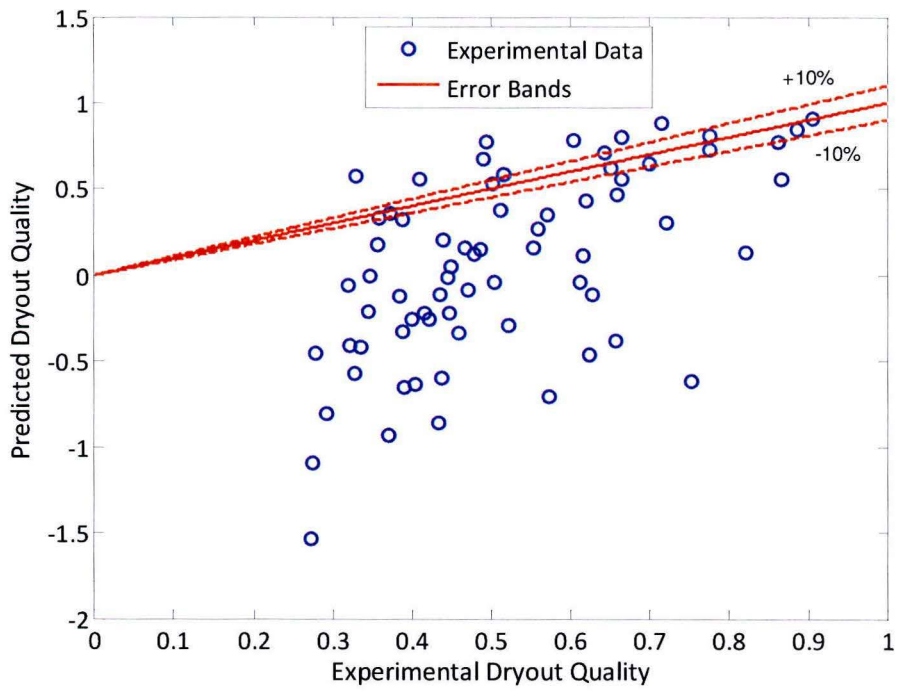**Figure 7.1 Dryout Prediction by Cheng et al. [14]**

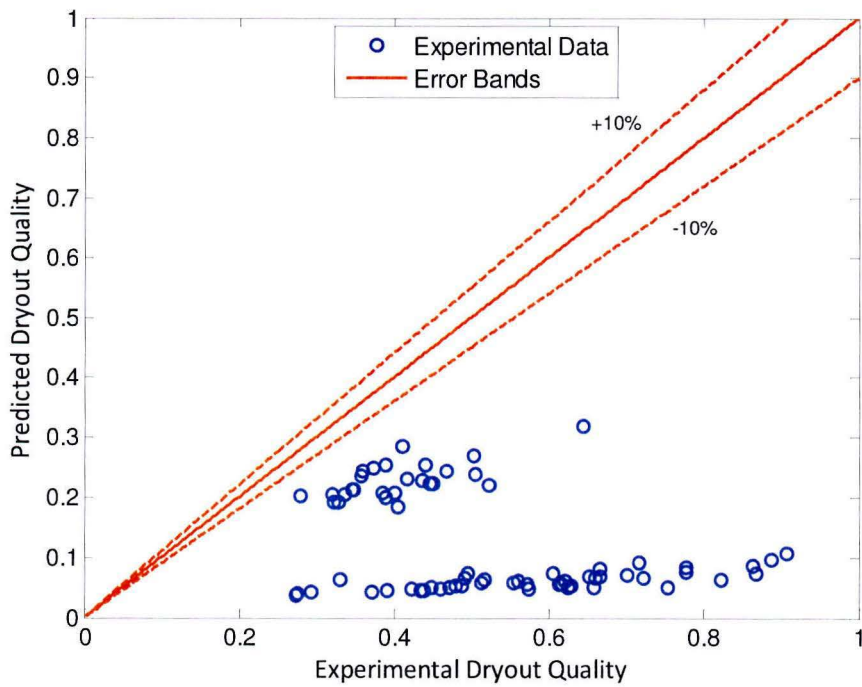**Figure 7.2 Dryout Prediction by Mastrullo et al. [18]**

Figure 7.3 Dryout Prediction by Jeong et al. [12]

7.2 New Correlation Development

Dryout model of Cheng et al. [14] describes the relation between dryout vapor quality, mass flux and heat flux quite well among the available models, as stated previously. The diameter effect is not taken into account in the original equation by Cheng et al. [14] (See Table 7.1). In order to account for the diameter effect, the coefficients of Weber and Froude number in the original equation should be modified such a way that increase of diameter should result in late dryout as it is seen from the test results. It means final coefficient of hydraulic diameter in combined non-dimensional Weber and Froude numbers should be positive to satisfy this relationship. In the present investigation, heat flux seems to be the governing parameter of dryout quality estimation as stated previously. In particular, increasing the heat flux, the dryout inception quality tends to decrease. In the equation of Cheng et al. [14], the critical heat flux equation is taken as the original critical heat flux equation of Kutateladze [16] (see Table 7.1). It is important to note that the accuracy of the dryout predictions is affected by this critical heat flux equation. That equation is a general prediction method developed for a wide range of refrigerants and it is not validated for CO_2. During correlation development, it is left as the original critical heat flux equation since critical heat flux prediction is not the task of this work and requires another experimental study focusing CO_2 critical heat flux determination. It is important to mention that the original dryout prediction model is an adapted version of Wojtan et al. [27] which is also based on Mori et al.`s study [15]. The history of the correlation development can be found in Section 10.9 of Appendix. It is seen that first two coefficients are never changed starting from Mori et al [15]. Although the reason is not stated in their paper, it is found out that the small changes in first two coefficients results in poor predictions. Therefore, they are left as unchanged during the regression analysis. The third coefficient is remained almost the same (change from 0.235 to 0.236) during the adaptation of Cheng et al. [14]. It means that coefficient does not play a role depending on the refrigerant type. The power factor of Weber number is also left the same when the correlation is adapted from Wojtan et al.`s [27] study to Cheng et al.`s study [14]. The reason of this unchanged is not stated in their paper. It is observed that the change of power coefficient of Weber number results in ill-conditioned system and cause the power coefficient of Froude number to be around zero. Due to this reason, the power coefficient of Weber number is left as the original coefficient following the same procedure as Cheng et al. [14]. The power factor of vapor to liquid density ratio $\frac{\rho_v}{\rho_l}$ should change depending on the saturation temperature limits. For example, the higher saturation temperature results in an early dryout due to easy breaking of liquid-vapor interface. And, it can be seen from Figure 1.4 that vapor to liquid density ratio is proportional to saturation temperature. This means that coefficient is to be positive to be consistent with the physics. Cheng et al. [14] left the coefficient unchanged when they are adapted the equation to CO_2 dryout prediction. Their database is valid from -28 °C to 25 °C including the saturation temperature of 22 °C of this study. Therefore, there is no need to adapt that coefficient either. In summary, two main modifications can be done on the original equation. The first modification is to encounter the higher heat fluxes in the equation since the original equation is valid till 46 kW/m^2 and experiments are up to 400 kW/m^2. Mainly, that modification is related to the non-dimensional $\frac{q}{q_{crit}}$ term. The other important factor is to encounter the diameter effect on dryout quality since the original

model is lack of diameter effect. It can be seen that coefficients of hydraulic diameter term in Weber and Froude numbers cancel out each other and no effect of hydraulic diameter is encountered in the original model (See Table 7.1). In addition, it is seen that increase of the mass flux leads to a decrease in the dryout quality till a certain mass flux, then the effect is vice versa. The reverse effect is observed less frequently compared to the first case. Moreover, the mass flux effect is not playing an important role on dryout quality within the current database. Therefore, the trend of original equation can be kept the same by keeping the final coefficient of mass flux positive in non-dimensional Weber and Froude numbers. The equation of Cheng et al. [14] is given in the form of:

$$x_{\mathrm{di}} = c_0 \exp\left[c_1 - c_2 \mathrm{We}_v^{c_3} \mathrm{Fr}_{v,\mathrm{Mori}}^{c_4} \left(\frac{\rho_v}{\rho_l}\right)^{c_5} \left(\frac{q}{q_{\mathrm{crit}}}\right)^{c_6}\right] \tag{7.1}$$

The coefficients of the original equation are listed in Table 7.3. This equation is modified by a nonlinear curve fitting analysis to predict the experimental dryout points taking into account the experimental observations as stated above. Non-linear least square regression is performed in Matlab. The program uses Levenberg-Marquardt algorithm as an iterative method to find the optimum solution. Variation in the initial values did not give significant changes in the results. The regression coefficients, adjusted coefficients of determination, R^2, and the statistics of original equation related to all experimental dataset are reported in Table 7.3. In Figure 7.4, a comparison of previous prediction [14] and new prediction is shown. Overall, 72% of the experimental data is predicted within ±15% error bands. It can be seen that the new equation for the dryout inception predicts the experimental data better than the method of Cheng et al. [14]. Generally, high mass flux cases of dryout points are missed out by the new equation. All the experimental dryout points and estimated dryout points with corresponding test conditions can be seen in Section 10.5 of Appendix.

Another important issue is to assure the validity of the annular flow at diabatic conditions. According to flow pattern map of Cheng et al. [14], the two phase flow structure is expected to be annular flow before dryout starts. From the experimental results, it is shown that heat transfer mechanism is nucleate boiling dominated and it is expected to have constant bubble formation at the wall. The findings of this study and expectation from the flow pattern of Cheng et al. [14] suggest that the flow patterns should have bubbly and annular flow together. This can be examined with high speed camera visualizations. The bubbly-annular flow structures are observed by Yun and Kim [24] in their CO_2 flow visualization study and corresponding images can be found in their publication.

It is also observed that the dryout inception quality increases with increase of mass flux after transition mass velocity. This behavior should be investigated with more experimental data since physical mechanism changes after transition mass velocity. Therefore, more extensive studies at high mass flux conditions need to be done for more precise dryout prediction considering transition mass fluxes of CO_2.

Table 7.3. Statistics of Non-Linear Regression Related to Dryout Vapor Quality Data

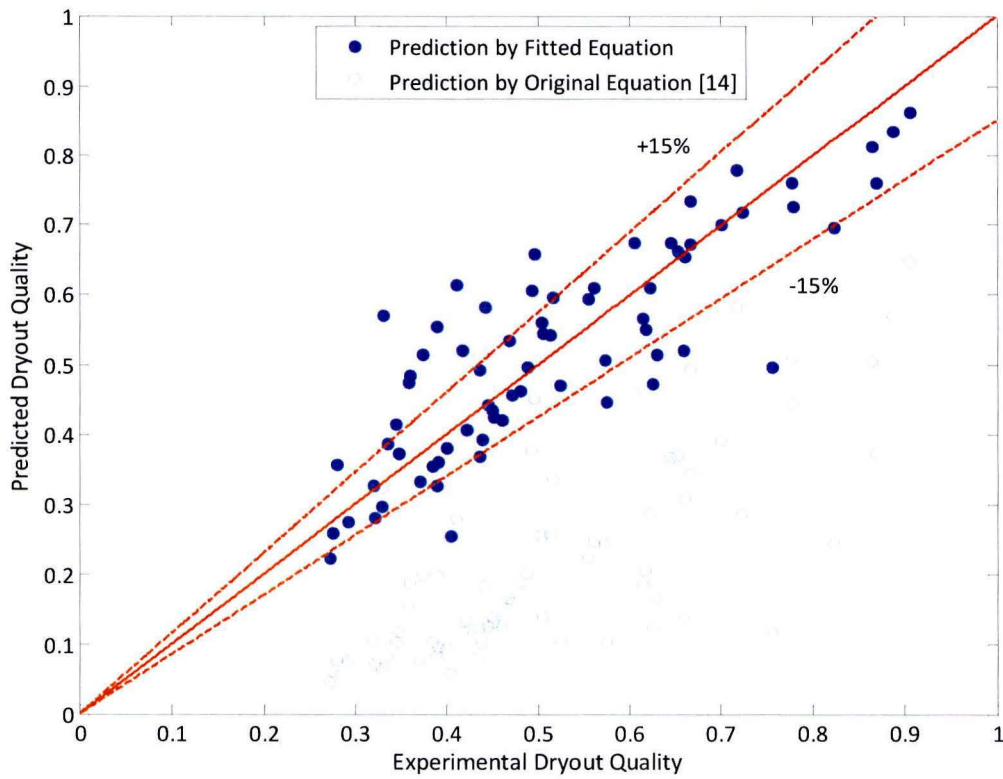| Changes in Dryout Prediction Equation	Regression Parameters							Statistics		
	c_0	c_1	c_2	c_3	c_4	c_5	c_6	MAE(%)	MRE(%)	R^2
New Fitted Coefficients	0.58	0.52	0.236	0.17	0.11	0.25	0.71	14.09	2.54	0.71
Old coefficients according to Cheng et al. [14]	0.58	0.52	0.236	0.17	0.17	0.25	0.27	59.53	-59.53	

Figure 7.4 Statistical Comparison between Experimental Dryout Quality and Predicted Dryout Quality

8   CONCLUSIONS AND FUTURE WORK

8.1   Conclusions and Remarks

A series of experiments has been carried out to characterize the two-phase heat transfer coefficient of CO_2 with a various mass flux, heat flux, and channel diameter conditions at 22 °C saturation temperature.   A database has been established containing around 2100 heat transfer coefficient measurement points. A correlation for dryout vapor quality prediction has been proposed based on experimental database. The following conclusions are derived from the experimental results:

➢   It has been observed that two-phase heat transfer coefficient is nucleate boiling dominated and strongly depends on the heat flux before dryout vapor quality. Although higher heat flux leads to an enhancement of activation of nucleation sites, it results in early dryout. Before critical vapor quality, the Cheng et al. [14] type two-phase heat transfer coefficient is the most appropriate prediction method for this regime.

➢   The mass flux effect is mostly found to be insignificant on the two-phase heat transfer coefficient. However, it is seen that the mass flux effect can play a role at low heat flux test conditions. At low heat fluxes, the higher mass flux leads to a higher Reynolds number thus a higher convective heat transfer contribution. In overall, this effect is not pronounced before the critical vapor quality since nucleate boiling drives the total two-phase heat transfer coefficient.

➢   Generally, reduction in channel diameter results in the increase of two-phase heat transfer coefficient. However, in some experiments, the two-phase heat transfer coefficients of both channel diameters do not differ significantly.

➢   Dryout vapor qualities are predicted by the modification of Cheng et al. [14] type dryout prediction equation. A non-linear regression analysis is performed to find the new coefficients of the dryout prediction equation. 72% of the experimental data is predicted within ±15% errors. The power coefficient of normalized heat flux term is extended to a higher value and diameter effect on dryout quality is encountered in the new equation different than the original equation.

➢   At adiabatic case, flow pattern transitions are investigated and a comparison is made with the CO_2 flow pattern map of Cheng et al. [14]. It is found out that intermittent to annular transition is dependent on mass flux and not a constant line as the flow pattern suggests.

➢   In the present study, the heat flux distribution around the microchannel is not perfectly uniform because the heat is only applied from the bottom side of the test block. Actually, heat transfer coefficient is dependent on heat flux conditions and therefore it is different at location of the microchannel. In reality, when using the available correlations in literature, one should take into account the non-uniformity effect of heat flux since most of the correlations are developed with uniform heating conditions.

➢   The measured pressure drop increases as mass flux increases. On the other hand, increase of the mass flux does not enhance heat transfer coefficient significantly as it is observed from the

experimental results. Therefore, the optimum evaporator design based on this experimental database would have low mass flux within the possible mass flux candidates and avoid poor post dryout heat transfer coefficients with the new dryout prediction equation.

8.2   Future Work and Recommendations

➤ Further studies in this area should extend the flow observations to diabatic cases and visualize the flow patterns at the diabatic conditions to check the validity of the CO_2 flow pattern map and nucleate boiling dominancy by observing the vapor bubble initiations. In addition, new flow visualization section shall allow observing the interface of the liquid and vapor phases to clarify the flow structures.

➤ Although the pressure drops are measured, frictional pressure drops are not reduced from total pressure drop. The future study may correlate the two-phase frictional pressure drops of CO_2.

➤ At the beginning of the tests, surface roughnesses of the test channels have been measured. However, the surface of the channel had to be etched and cleaned after the melting of the soldering on top of the channel. Therefore, the roughness values probably changed. The new roughness measurements can be done and the effect of surface roughness on the heat transfer coefficient can be investigated.

➤ The effects of flow conditions at the inlet of the test section and manifold design have an influence on pressure drop and flow instabilities. In future, those effects should be studied when the tests are done with multichannel evaporators.

➤ Investigation of post dryout heat transfer coefficients of current experimental data is left as a future work. The analysis can be done by differentiating the post dryout heat transfer coefficient data into transition and fully dryout regions. The effects of test conditions (i.e. mass flux, heat flux and channel diameter) can be investigated and existing models for post dryout heat transfer coefficients can be verified for the current database.

➤ One of the methods to enhance the two-phase flow heat transfer coefficients is to use micro finned structures inside the microchannels. It is reported by Thome [52], that heat transfer enhancement ratios are as high as three to four times at low mass velocity flows and partial dryout can be delayed by using fins inside of the microchannels. For example, Koyama et al. [53] showed that two-phase heat transfer coefficient of CO_2 is increased by 50%-100% in 9.52mm tube diameter, and 70%-110% in a 5 mm tube. It is reported that microfin tubes can be produced from about to 0.1 to 0.4 mm in the form of helix fins by drawing a plain copper tube over a mandrel [52]. Also, it is found out that microfins exist till size of 200 µm in literature [54], [55]. The future evaporator may have microfins and new tests can be performed to understand the effect of microfins on heat transfer coefficient and dryout prediction equation.

➤ Future work should extend the test conditions to wider operation conditions in terms of scientific point of view. Because, two-phase CO_2 heat transfer coefficient data in literature are very limited. For example, higher and lower saturation temperatures shall be tested to

investigate the saturation temperature effects on pre-dryout heat transfer coefficient and dryout prediction equation.

Finally, it can be said that choosing the appropriate models and correlations for two-phase heat transfer and pressure drop is essential in order to design the compact heat exchangers. This experimental study of CO_2 flow boiling will assist in understanding the two-phase heat transfer characteristics and estimating the dryout vapor qualities for future micro-evaporator in the actuator cooling system of ASML Next Generation Lithography Machines. Moreover, there is a strong need for collecting new experimental data on the flow boiling heat transfer of CO_2 at high saturation temperatures in open literature which is partly succeeded in this thesis.

This page is intentionally left blank.

9 REFERENCES

[1] A. Pearson, Carbon Dioxide-new uses for an old refrigerant, International Journal of Refrigeration 28 (2005), pp. 1140-1148.

[2] H.J.Van Gerner, Heat Transport on the Next Generation Stage, Vol. NLR-CR-2010-060. Eindhoven: ASML Company Secret. Owner: NLR+Partners.

[3] E.W. Lemmon, M.O. Mc Linden, M.L. Huber, NIST Standard Reference Database 23, Version 8.0, REFPROP (2007).

[4] E. Hihara, S. Tanaka, Boiling heat transfer of carbon dioxide in horizontal tubes in: Proceedings of 4th IIR-Gustav Lorentzen Conference, Purdue University (2000), pp. 279–284.

[5] R. Yun, Y. Kim, Critical quality prediction for saturated flow boiling of CO_2 in horizontal small diameter tubes, International Journal of Heat and Mass Transfer 46.14 (2003), pp. 2527-535.

[6] T. Fujita, T. Ueda, Heat Transfer to falling liquid films and film breakdown-I subcooled liquid film, International Journal of Heat Mass Transfer 21 (1978), pp. 97-108.

[7] J. Pettersen, R. Rieberer, S.T. Munkejord, Heat transfer and pressure drop characteristics of evaporating carbon dioxide in microchannel tubes, in: Proceedings of 4th IIR-Gustav Lorentzen Conference, Purdue University (2000), pp. 107–114.

[8] S.Y. Ahmad, Fluid to fluid modeling of critical heat flux: A compensated distortion model, International Journal of Heat Mass Transfer 16 (1973), pp. 641–662.

[9] L.L. Levitan, F.P. Lantsman, Investigating burnout with flow of steam–water mixture in a round tube, Thermal Engineering (USSR) 22 (1) (1975), pp. 102–105 (English trans.)

[10] S.H. Yoon, E.S. Cho, Y.W. Hwang, M.S. Kim, K. Min, Y. Kim, Characteristics of evaporative heat transfer and pressure drop of carbon dioxide and correlation development, International Journal of Refrigeration 27 (2004), pp. 111-119.

[11] S.H. Yoon, E.S. Cho, Y.W. Hwang, M.S. Kim, K. Min, Y. Kim, Errata to Characteristics of evaporative heat transfer and pressure drop of carbon dioxide and correlation development [International Journal of Refrigeration 27 (2004), pp. 111-117] , International Journal of Refrigeration 27 (2004), pp. 1008.

[12] Jeong, S.,Park,D., Evaporative heat transfer of CO_2 in a smooth and a grooved multi-channel microtube, in: 5th International Conference on Heat Transfer, Fluid Mechanics and Thermodynamics, Sun City, South Africa (2005).

[13] X.M. Wu, Y.J. Tang, J.C. Min, P.X. Jiang, Characteristics of flow boiling heat transfer of sub-critical CO_2 in mini-channels with micro-fins, Proceedings of the International Refrigeration and Air Conditioning Conference at Purdue, USA (2008).

[14] L. Cheng, New Prediction Methods for CO_2 Evaporation inside Tubes: Part II—An Updated general flow boiling heat transfer model based on flow patterns, International Journal of Heat and Mass Transfer 51.1-2 (2008), pp.125-35.

[15] H. Mori, S. Yoshida, K. Ohishi, Y. Kokimoto, Dryout quality and post dryout heat transfer coefficient in horizontal evaporator tubes, in: Proceedings of the 3rd European Thermal Sciences Conference (2000), pp. 839–844.

[16] S.S. Kutateladze, On the transition to film boiling under natural convection, Kotloturbostroenie (3) (1948), pp. 10–12.

[17] M. Ducoulombier, S. Colasson, J. Bonjour, Carbon dioxide flow boiling in a single microchannel – Part II: Heat transfer, Experimental Thermal and Fluid Science 35, Issue 4 (2011), pp. 597-611.

[18] R. Mastrullo, A. W. Mauro, J.R. Thome, D. Toto and G. P. Vanoli, Flow pattern maps for convective boiling of CO_2 and R410A in a horizontal smooth tube: Experiments and new correlations analyzing the effect of the reduced pressure, International Journal Of Heat And Mass Transfer 55 (2012), pp. 1519-1528.

[19] H. Muller-Steinhagen, K. Heck, A simple friction pressure drop correlation for two-phase flow in pipes, Chemical Engineering Process 20 (1986), pp. 297-308.

[20] Incropera, F.P., Dewitt, D.P., Bergman, T.L, Lavine, A.S., Introduction to Heat Transfer, 5th Edition, John Wiley & Sons, 2007.

[21] R.J.Moffat, Using uncertainty analysis in the planning of an experiment, Journal of Fluids Engineering 107 (1985), pp.173–178.

[22] J.G. Collier, J.R. Thome, Convective boiling and condensation, Oxford University Press, Oxford (1994).

[23] J. Pettersen, Flow vaporization of CO_2 in microchannel tubes, Doctor technicae thesis, Norwegian University of Science and Technology (2002).

[24] R. Yun, Y. Kim, Flow regimes for horizontal two-phase flow of CO_2 in a heated narrow rectangular channel, International Journal of Multiphase Flow 30 (2004), pp. 1259–1270.

[25] Park, C. Y. and P. S. Hrnjak, Flow Boiling Heat Transfer, Pressure Drop, and Flow Pattern for CO_2 in a 3.5 mm Horizontal Smooth Tube, Journal of Heat Transfer 131 (2009).

[26] J. Weisman, D. Duncan, J. Gibson, and T. Crawford, Effect of fluid properties and pipe diameter on two phase flow patterns in horizontal lines, International Journal of Multiphase Flow 5 (1979), pp. 437–462.

[27] L. Wojtan, T. Ursenbacher, and J.R. Thome, Investigating of flow boiling in horizontal tubes: Part I–A new adiabatic two-phase flow pattern map, International Journal of Heat Mass Transfer 48 (2005), pp. 2955–2969.

[28] R. Mastrullo, A.W. Mauro, J.R. Thome, D. Toto, G.P. Vanoli, Flow pattern maps for convective boiling of CO_2 and R410A in a horizontal smooth tube: Experiments and new correlations analyzing the effect of the reduced pressure, International Journal of Heat and Mass Transfer, Volume 55, Issues 5–6 (2012), pp. 1519-1528.

[29] Lixin Cheng, Gherhardt Ribatski, Jesús Moreno Quibén, John R. Thome, New prediction methods for CO_2 evaporation inside tubes: Part I – A two-phase flow pattern map and a flow pattern based phenomenological model for two-phase flow frictional pressure drops, International Journal of Heat and Mass Transfer, Volume 51, Issues 1–2 (2008), pp. 111-124.

[30] Kwang-Il Choi, A.S. Pamitran, Chun-Young Oh, Jong-Taek Oh, Boiling heat transfer of R-22, R-134a, and CO_2 in horizontal smooth minichannels, International Journal of Refrigeration, Volume 30, Issue 8 (2007), pp. 1336-1346.

[31] R.L. Webb, and N.S. Gupte, Heat Transfer Engineering 13 (3), pp.58-81.

[32] R. Revellin, P. Haberschill, J. Bonjour, J.R. Thome, Conditions of liquid film dryout during saturated flow boiling in microchannels, Journal of Chemical Engineering Science 63 (2008), pp. 5795-5801.

[33] Rin Yun, Yongchan Kim, Min Soo Kim, Flow boiling heat transfer of carbon dioxide in horizontal mini tubes, International Journal of Heat and Fluid Flow, Volume 26, Issue 5 (2005), pp. 801-809.

[34] G.F. Hewitt, Pressure Drop in: Hetsroni G. (Ed.), Handbook of Multiphase System. Hemisphere Publishing Corporation, Washington DC (1985), pp. 44-75.

[35] F. W. Dittus and L. Ml K. Boelter, Heat transfer in automobile radiators of the tubular type, Publications in Engineering 2 (1930), pp. 443.

[36] Hoo-Kyu Oh, Hak-Geun Ku, Geon-Sang Roh, Chang-Hyo Son, Seung-Jun Park, Flow boiling heat transfer characteristics of carbon dioxide in a horizontal tube, Applied Thermal Engineering, Volume 28, Issues 8–9 (2008), pp. 1022-1030.

[37] P.A. Kew, K. Cornwell, Correlations for the prediction of boiling heat transfer in small-diameter channels, Applied Thermal Engineering 17 (1997), pp. 705-715.

[38] T.N. Tran, M.W. Wambsganss, D.M. France, Small circular and rectangular-channel boiling with two refrigerants, International Journal of Multiphase Flow 22 (1996), pp. 485-498.

[39] M.G. Cooper, Heat flow rates in saturated nucleate pool boiling – a wide ranging examination using reduced properties, Advanced Heat Transfer 16 (1984), pp. 157–239.

[40] K.E. Gungor, R.H.S. Winterton, A general correlation for flow boiling in tubes and annuli, International Journal of Heat Mass Transfer 29, Issue 3 (1986), pp. 315–358.

[41] K.E. Gungor and R.H.S. Winterton, Simplified General Correlation for Flow Saturated Boiling and Comparisons of Correlations with Data, Chemical Engineering Research and Design 65 (1987), pp. 148-156.

[42] Lixin Cheng, Gherhardt Ribatski, Leszek Wojtan, John R. Thome, New flow boiling heat transfer model and flow pattern map for carbon dioxide evaporating inside horizontal tubes, International Journal of Heat and Mass Transfer, Volume 49, Issues 21–22 (2006), pp. 4082-4094.

[43] Z. Liu, R.H.S. Winterton, A general correlation for saturated and subcooled flow boiling in tubes and annuli, based on a nucleate pool boiling equation, International Journal of Heat Mass Transfer 34 (1991) , pp. 2759–2766.

[44] M.H. Maqbool, B. Palm, R. Khodabandeh, Boiling heat transfer of ammonia in vertical smooth mini channels: Experimental results and predictions, International Journal of Thermal Sciences, Volume 54 (2012), pp. 13-21.

[45] Rin Yun, Yongchan Kim, Min Soo Kim, Convective boiling heat transfer characteristics of CO_2 in microchannels, International Journal of Heat and Mass Transfer, Volume 48 (2005), pp. 235-242.

[46] D. Gorenflo, Pool Boiling: VDI-Heat Atlas, VDI, Dusseldorf (1993).

[47] N. Kattan, J.R. Thome, D. Favrat, Flow boiling in horizontal tubes. Part 1. Development of a diabatic two-phase flow pattern map, Journal of Heat Transfer 120 (1998), pp. 140–147.

[48] N. Kattan, J.R. Thome, D. Favrat, Flow boiling in horizontal tubes. Part 2. New heat transfer data for five refrigerants, Journal of Heat Transfer 120 (1998), pp. 148–155.

[49] N. Kattan, J.R. Thome, D. Favrat, Flow boiling in horizontal tubes. Part 3. Development of a new heat transfer model based on flow patterns, Journal of Heat Transfer 120 (1998), pp. 156–165.

[50] S.G. Kandlikar, A general correlation for saturated two-phase flow boiling heat transfer inside horizontal and vertical tubes, Journal of Heat Transfer 112 (1990), pp. 219-228.

[51] Jung, D. S., McLinden, M., Radermacher, R., Didion, D., A study of flow boiling heat transfer with refrigerant mixtures, International Journal of Mass Transfer 32 (1989), pp.1751-1764.

[52] J.R. Thome, Engineering Databook III, Wolverine Tube, Inc, Huntsville, AL, USA, 2004 [http://www.wlv.com/products/databook/db3/DataBookIII.pdf].

[53] L. Gao, T. Honda, S. Koyama, Experiments on flow boiling heat transfer of almost pure CO_2 and CO_2-oil mixtures in horizontal smooth and microfin tubes, HVAC&R Research 13 (2007), pp.415-425.

[54] S. Krishnamurthy, and Y. Peles. Flow boiling of water in a circular staggered micro-pin fin heat sink, International Journal of Heat and Mass Transfer 51.5-6 (2008), pp.1349-364.

[55] Qu, Weilin, and Abel Siu-Ho. Experimental study of saturated flow boiling heat transfer in an array of staggered micro-pin-fins, International Journal of Heat and Mass Transfer 52.7-8 (2009), pp. 1853-863.

10 APPENDIX

10.1 Individual Contributions of Measurement Parameters to Heat Transfer Coefficient and Vapor Quality Uncertainties

Uncertainties of the measurement devices are examined to find out their contributions to total heat transfer coefficient and vapor quality uncertainties. In order to see relative contribution of each parameter, the uncertainties associated with other parameters are set out to zero. Then, resultant uncertainties of heat transfer coefficient and vapor quality are recorded. The uncertainties related to heat transfer coefficient and vapor qualities are listed with their individual contributions in Table 10.1 and Table 10.2.

Table 10.1 Contribution of Individual Measurement Uncertainties to Heat Transfer Coefficient Uncertainty

Uncertainty Parameters	Individual Uncertainty Contributions to Heat Transfer Coefficient Uncertainty
NTC Temperature Sensors	3.43%
Location of NTC Temperature Sensors	3.5%
Saturation Pressure (P_{sat})	11.07%
Channel Length (L_h)	1.03%
Channel Width (W)	5.27%
Evaporator Power Supply ($P_{evaporator}$)	0.58%

Table 10.2 Contribution of Relative Measurement Uncertainties to Vapor Quality Uncertainty

Uncertainty Parameters	Individual Uncertainty Contributions to Vapor Quality Uncertainty
Cori-Flow Meter	0.13%
Preheater Power Supply ($P_{preheater}$)	0.19%
Saturation Pressure (P_{sat})	0.58%
Distance Between NTC Temperature Sensors	0.004%
Saturation Temperature At Test Section Inlet	0.3%

10.2 Heat Transfer Coefficient and Total Pressure Drop Measurement Results
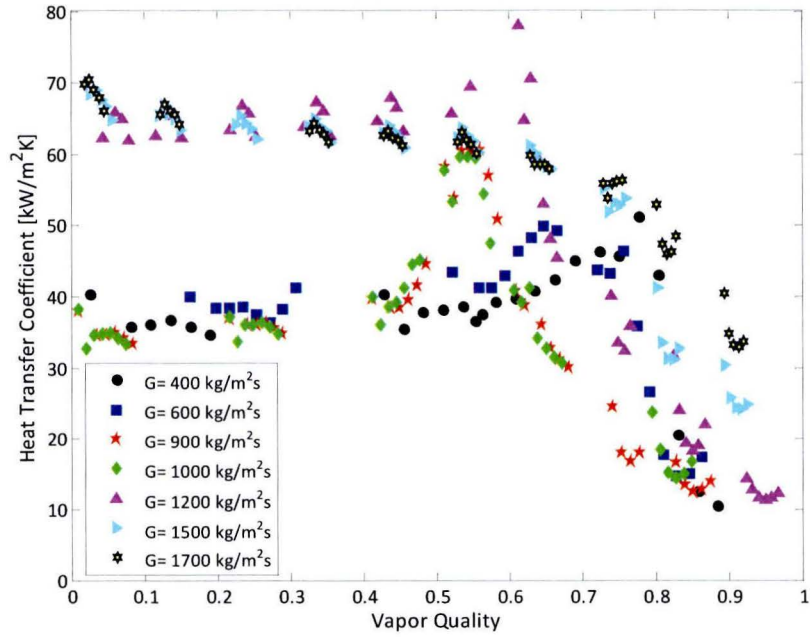
10.2.1 Effect of Mass Flux

Figure 10.1 Heat Transfer Coefficient at q=75 kW/m^2, T_{sat}=22 °C, D_h=1.5 mm
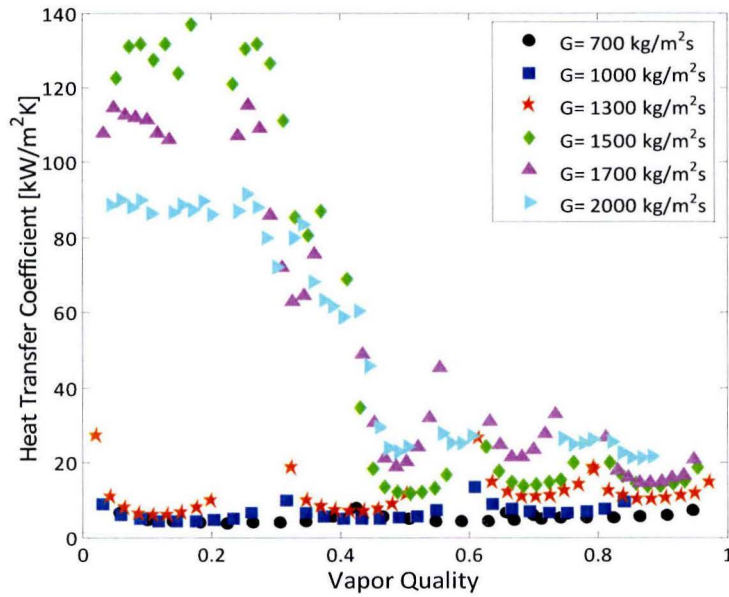
Figure 10.2 Heat Transfer Coefficient at q=200 kW/m^2, T_{sat}=22 °C, D_h=1.5 mm
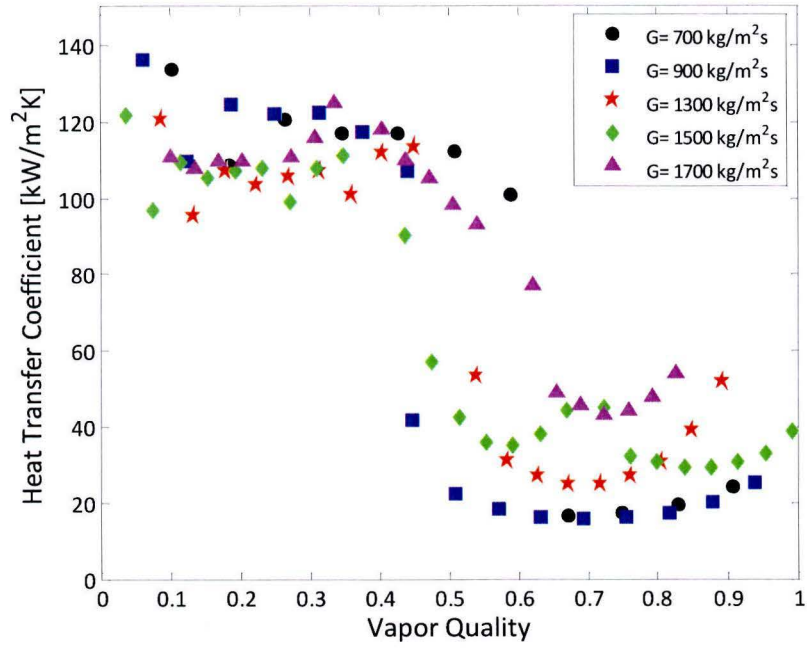
Figure 10.3 Heat Transfer Coefficient at q=140 kW/m², T_{sat}=22 °C, D_h=0.5 mm
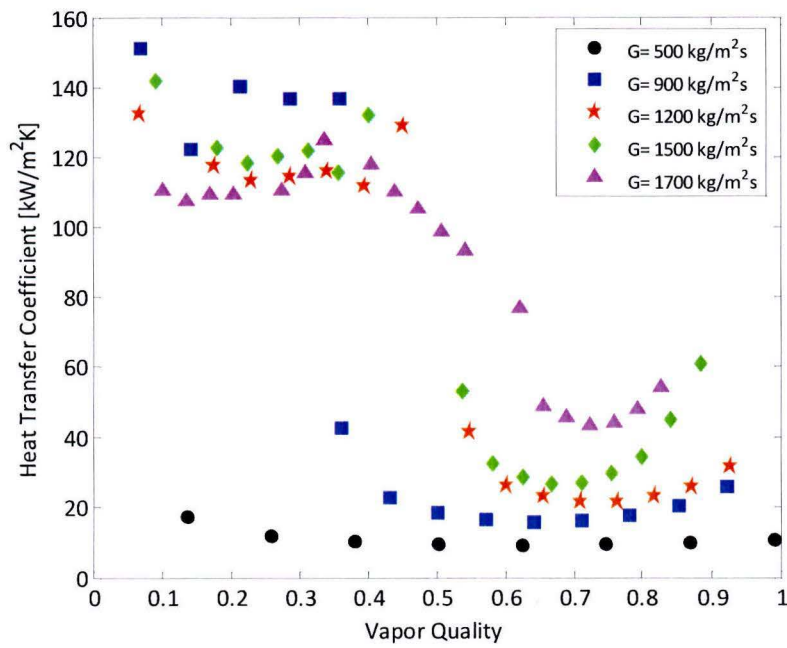
Figure 10.4 Heat Transfer Coefficient at q=185kW/m², T_{sat}=22 °C, D_h=0.5 mm
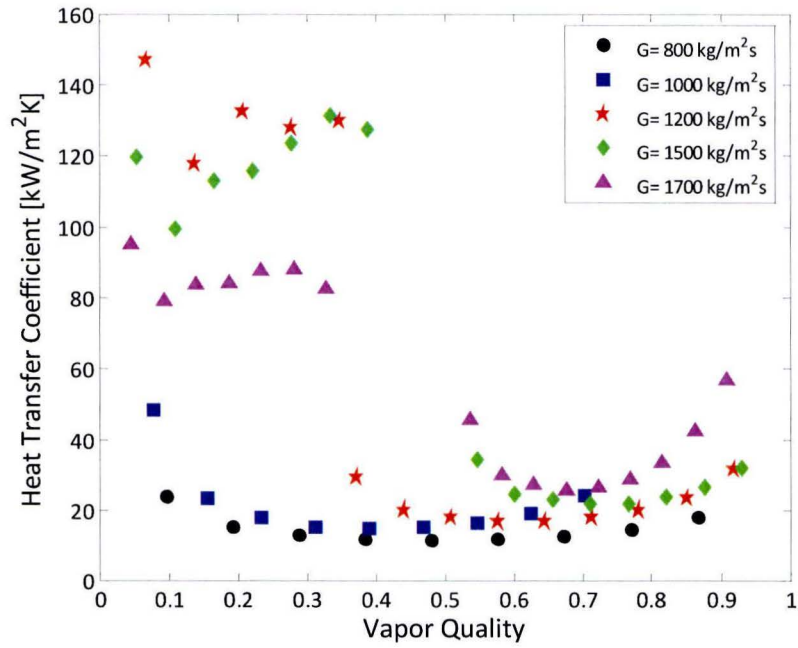
Figure 10.5 Heat Transfer Coefficient at q=200 kW/m^2, T_{sat}=22 °C, D_h=0.5 mm

10.2.2 Effect of Heat Flux
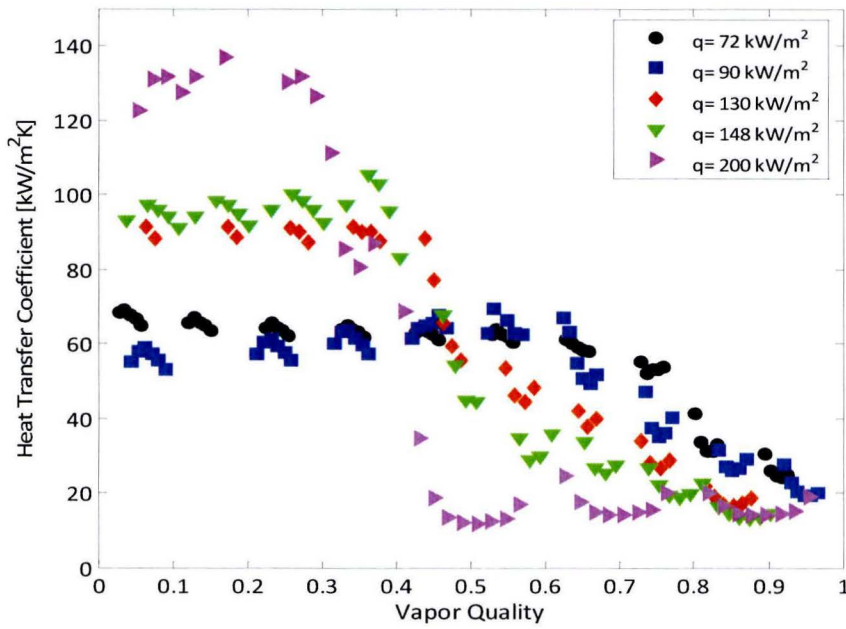
Figure 10.6 Heat Transfer Coefficient at G=1500 kg/m^{2}s, T_{sat}=22 °C, D_h=1.5 mm
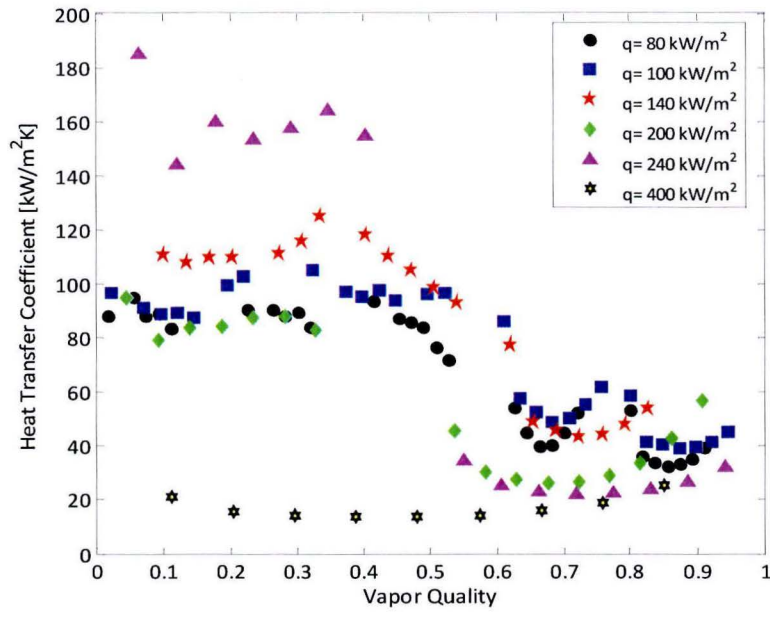
Figure 10.7 Heat Transfer Coefficient at G=1700 kg/m^{2}s, T_{sat}=22 °C, D_h=0.5 mm
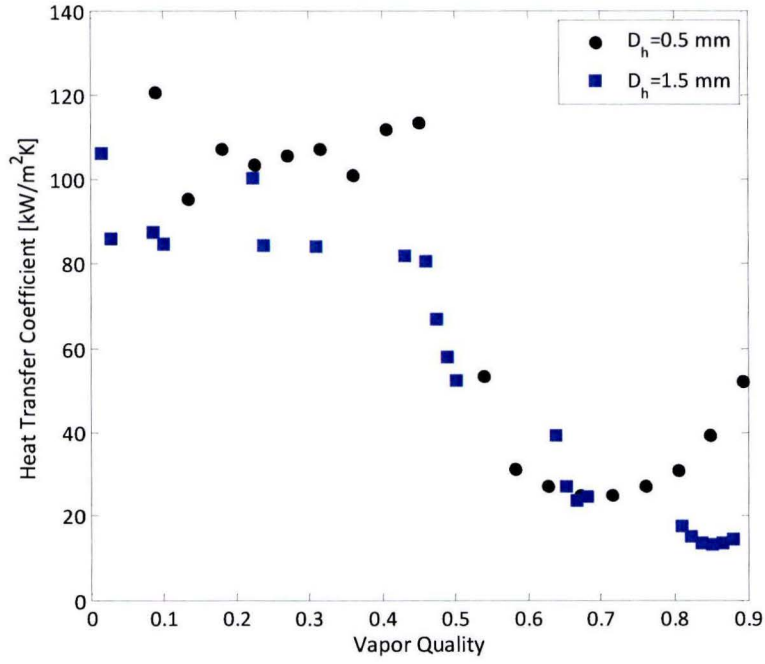
10.2.3 Effect of Hydraulic Diameter

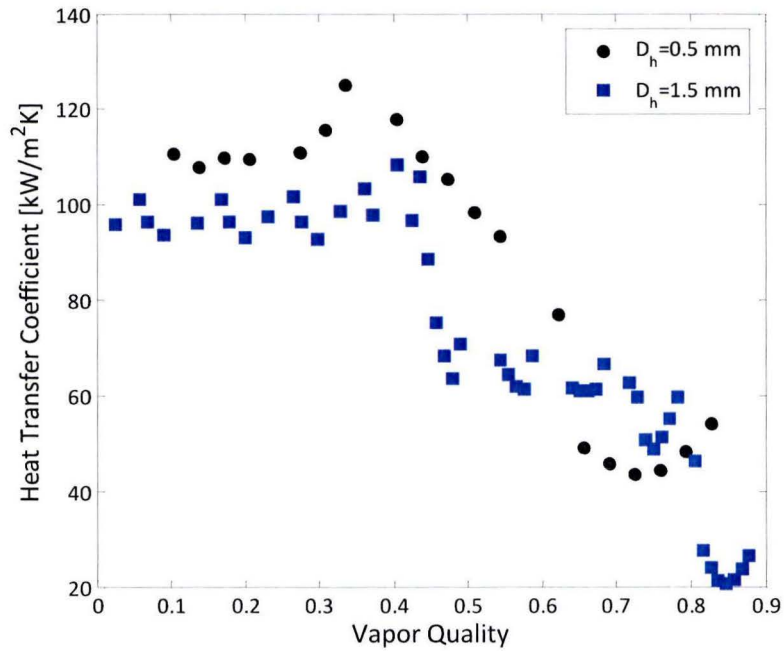**Figure 10.8 Heat Transfer Coefficient at *G*=1300 kg/m²s, *q*=130 kW/m², *T*ₛₐₜ=22 °C**

Figure 10.9 Heat Transfer Coefficient at *G*=1700 kg/m²s, *q*=130 kW/m², *T*ₛₐₜ=22 °C

92
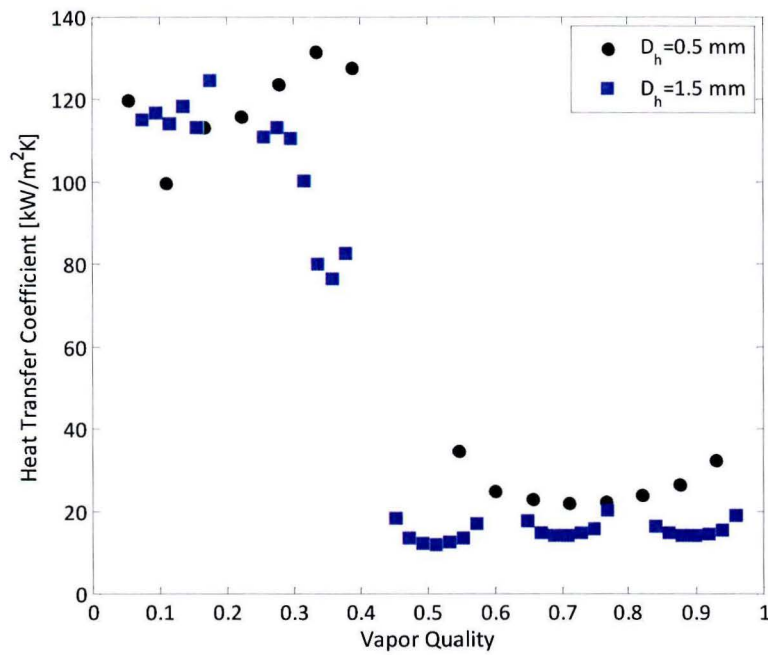
Figure 10.10 Heat Transfer Coefficient at *G*=1500 kg/m²s, *q*=200 kW/m², *T*$_{sat}$=22 °C
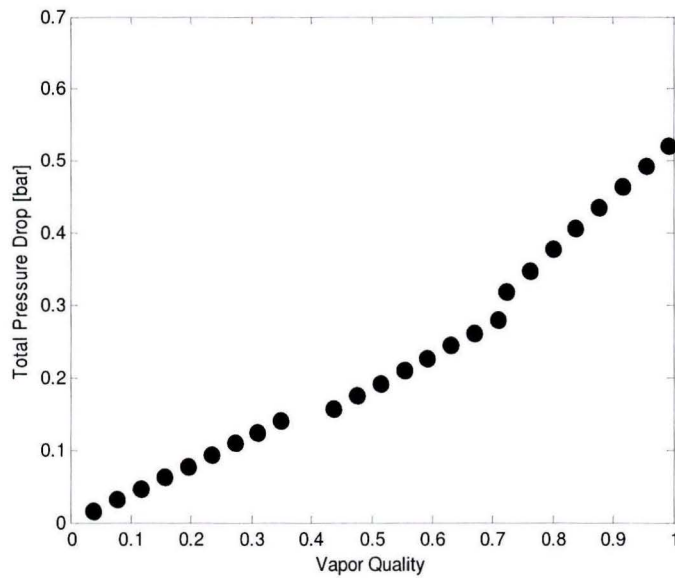
10.2.4 Total Pressure Drop Measurements

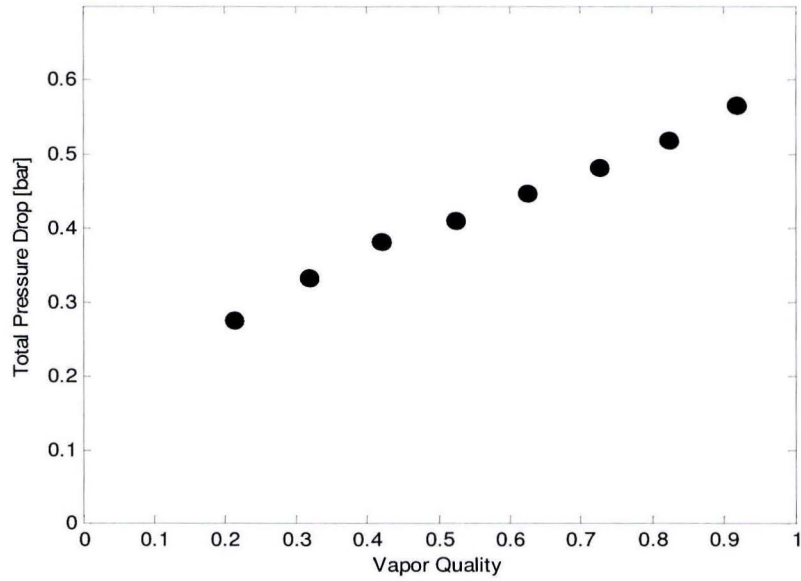**Figure 10.11 Total Pressure Drop at *q*=140 kW/m², *G*=1500 kg/m²s, *D*$_h$=0.5 mm**

Figure 10.12 Total Pressure Drop at q=148 kW/m^2, G=1700 kg/m^{2}s, D_h=1.5 mm
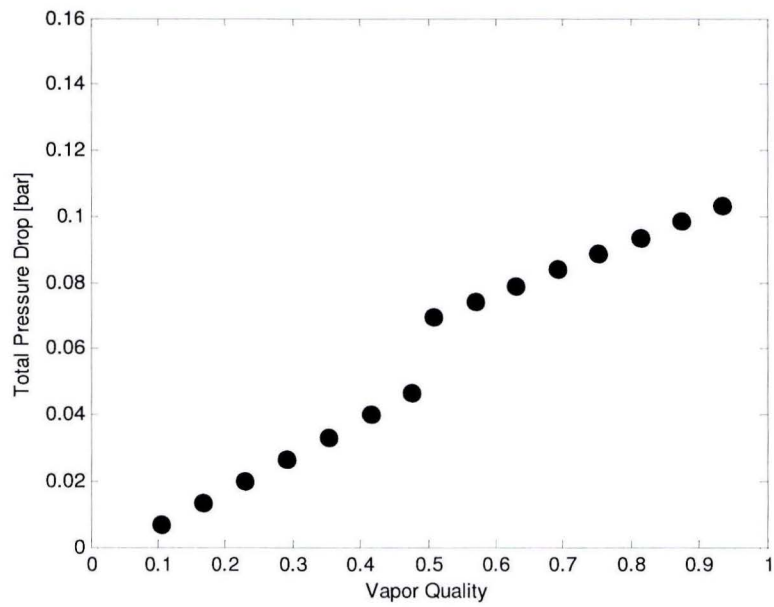
Figure 10.13 Total Pressure Drop at q=100 kW/m^2, G=700 kg/m^{2}s, D_h=0.5 mm

10.3 Theoretical Laminar to Transition Mass Velocity Model of Revellin et al. [32]

Revellin et al. [32] have presented a theoretical model that predicts two different trends of CO_2 saturated flow boiling in dryout quality versus mass velocity. Their model is important in terms of estimating the maximum mass velocity for which the conventional microchannel correlations of dryout predictions can be applied. According to their model, the liquid film passes through two different states: laminar flow ($Re_\delta < \psi = 2300$) and transition flow ($Re_\delta = \psi$). They have omitted the turbulent flow ($Re_\delta > \psi$) since no experimental data are available. The laminar to transition mass velocity refers to the mass velocity at which the flow passes from laminar to transition. The laminar film dryout implies a decrease of the dryout vapor quality with mass velocity while the transition film dryout implies an increase of the dryout quality with mass velocity. A criterion has been proposed to identify the laminar to transition mass velocity for CO_2. The liquid film Reynolds number at dryout condition is defined as:

$$Re_\delta = \frac{GR(1 - x_{dryout})}{\mu_l} \qquad (10.1)$$

where R is the tube radius. At the laminar to transition threshold ($Re_\delta = \psi$), the following equality is obtained:

$$\psi = \frac{GR(1 - x_{dryout})}{\mu_l} \qquad (10.2)$$

Then, they combine dryout vapor quality prediction equation by Jeong [12] is given as

$$x_{dryout} = 6.2 Re_{lo}^{-0.5} Bo^{-0.2} Bd^{-0.45} \qquad (10.3)$$

And they fix the $Bo^{-0.2}$ term to an average value of 6.5. With this simplification, the following equation is solved

$$GR + G^{0.5} b_2 - \psi \mu_l = 0 \qquad (10.4)$$

with

$$b_2 = -46.5 R (\mu_l/D)^{0.5} Bd^{-0.45} \qquad (10.5)$$

Then the solution is provided as

$$G_{transition} = \left[\frac{-b_2 + \sqrt{b_2^2 + 4\psi\mu_l R}}{2R} \right]^2 \qquad (10.6)$$

The dryout vapor quality is influenced by laminar to turbulent transition and it is shown in Figure 10.14. The similar trend that is predicted by their model is observed two times in the current database (See Figure 6.3). However, this model is not numerically accurate to predict the experimental transition mass velocities. For example, the transition mass velocity is 1000 kg/m²s at the test condition of 75 kW/m² in 1.5 mm channel diameter while the model predicts the transition mass velocity as 561 kg/m²s. It may be due to the fact that their model uses the dryout correlation by Jeong et al. [12] which is not a statistically good prediction model for this study (See Figure 7.3 and Table 7.2). Moreover, they suggested collecting and analyzing more experimental data to have a more precise idea of this

phenomenon. For that reason, the decreasing dryout quality with increase of mass velocity is taken as the general trend during the dryout correlation development in Chapter 7.
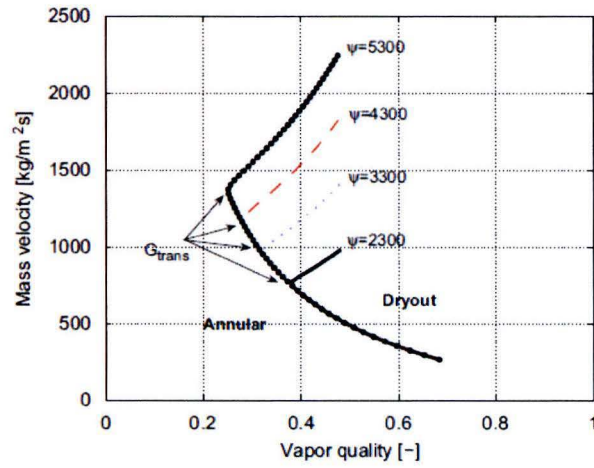
Figure 10.14 Influence of the laminar-to-turbulent transition (ψ) on the dryout vapor quality for CO_2, D=0.8 mm, L=500 mm and T_{sat}=10 °C [32]

10.4 Definitions of Statistical Errors

The statistical errors and standard deviation that are used in Chapter 7 are defined below:

$$Error, \quad \varepsilon_n = \left(\frac{x_{predicted,n} - x_{experimental,n}}{x_{experimental,n}} \right) \qquad (10.7)$$

$$Mean\ absolute\ error\ (MAE), \quad |\bar{\varepsilon}| = \frac{1}{N} \sum_{n=1}^{N} |\varepsilon_n| \qquad (10.8)$$

$$Mean\ absolute\ error\ (MAE), \quad \bar{\varepsilon} = \frac{1}{N} \sum_{n=1}^{N} \varepsilon_n \qquad (10.9)$$

$$Standard\ deviation, \quad \sigma = \sqrt{\frac{1}{N} \sum_{n=1}^{N} (\varepsilon_n - \bar{\varepsilon})^2} \qquad (10.10)$$

10.5 Experimental and Predicted Critical Vapor Qualities At Test Conditions

D_h (mm)	G (kg/m²s)	q (kW/m²)	Experimental Dryout Quality	Predicted Dryout Quality
1.5	200	38	0.906	0.86
1.5	300	38	0.89	0.84
1.5	402	38	0.86	0.81
1.5	700	38	0.86	0.76
1.5	1000	38	0.8	0.72
1.5	1200	38	0.82	0.70
1.5	300	75	0.78	0.76
1.5	400	75	0.74	0.73
1.5	500	74	0.7	0.70
1.5	600	76	0.70	0.67
1.5	700	74	0.66	0.66
1.5	900	76	0.56	0.61
1.5	1001	76	0.55	0.59
1.5	1200	75	0.62	0.57
1.5	1502	77	0.75	0.52
1.5	1703	77	0.79	0.50
1.5	200	89	0.72	0.78
1.5	300	90	0.71	0.73
1.5	500	93	0.62	0.66
1.5	700	93	0.66	0.61
1.5	1000	93	0.62	0.55
1.5	1200	94	0.62	0.52
1.5	1500	94	0.6	0.47
1.5	1700	95	0.56	0.45
1.5	300	130	0.60	0.68
1.5	500	131	0.52	0.60

1.5	700	128	0.49	0.54
1.5	900	128	0.42	0.50
1.5	1100	129	0.47	0.46
1.5	1200	132	0.45	0.43
1.5	1300	130	0.46	0.42
1.5	1500	130	0.44	0.39
1.5	1700	130	0.42	0.37
1.5	300	142	0.49	0.66
1.5	400	149	0.49	0.61
1.5	500	147	0.33	0.57
1.5	700	150	0.57	0.51
1.5	900	148	0.46	0.46
1.5	1200	147	0.38	0.41
1.5	1500	148	0.39	0.36
1.5	1700	149	0.45	0.33
1.5	1497	208	0.30	0.28
1.5	1698	202	0.26	0.26
1.5	1971	209	0.27	0.22
0.5	1200	76	0.44	0.58
0.5	1497	76	0.5	0.54
0.5	1700	76	0.5	0.52
0.5	500	95	0.64	0.68
0.5	700	100	0.41	0.62
0.5	999	100	0.42	0.56
0.5	1195	95	0.46	0.54
0.5	1498	95	0.43	0.49
0.5	1698	94	0.44	0.47
0.5	700	130	0.50	0.56
0.5	900	130	0.37	0.52
0.5	1099	131	0.36	0.48

0.5	1300	131	0.44	0.44
0.5	1500	131	0.34	0.41
0.5	1699	132	0.33	0.39
0.5	901	148	0.36	0.48
0.5	1196	150	0.39	0.43
0.5	1501	150	0.35	0.38
0.5	1692	149	0.31	0.36
0.5	1194	185	0.34	0.37
0.5	1300	186	0.38	0.35
0.5	1496	186	0.38	0.33
0.5	1708	188	0.42	0.30
0.5	1194	223	0.24	0.33
0.5	1505	223	0.31	0.28
0.5	1700	224	0.40	0.26

10.6 Technical Drawings of Test Channels

### 10.6.1 Technical Drawing of 1.5 mm Single Square Channel Geometry
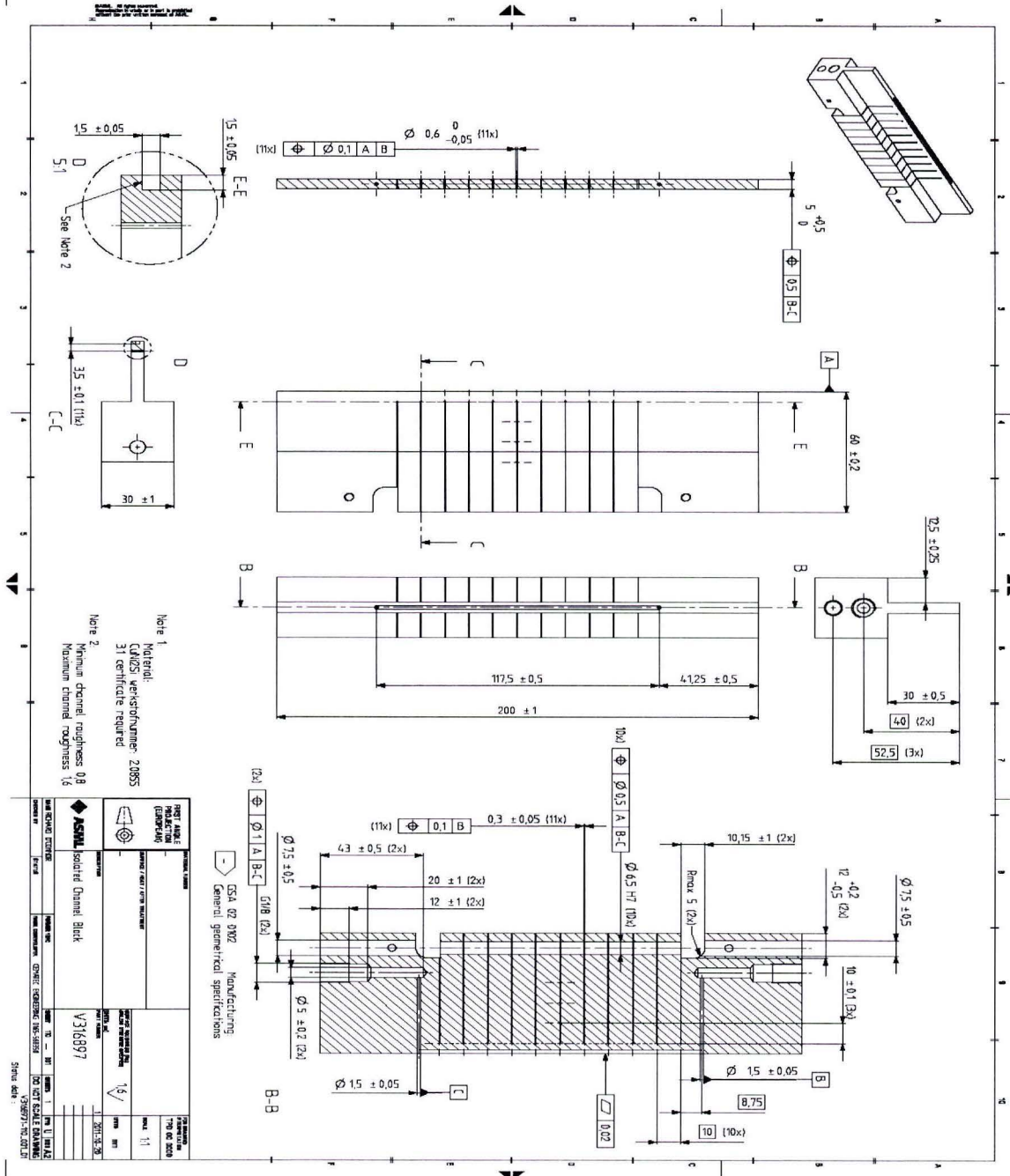
10.6.2 Technical Drawing of 0.5 mm Single Square Channel Geometry
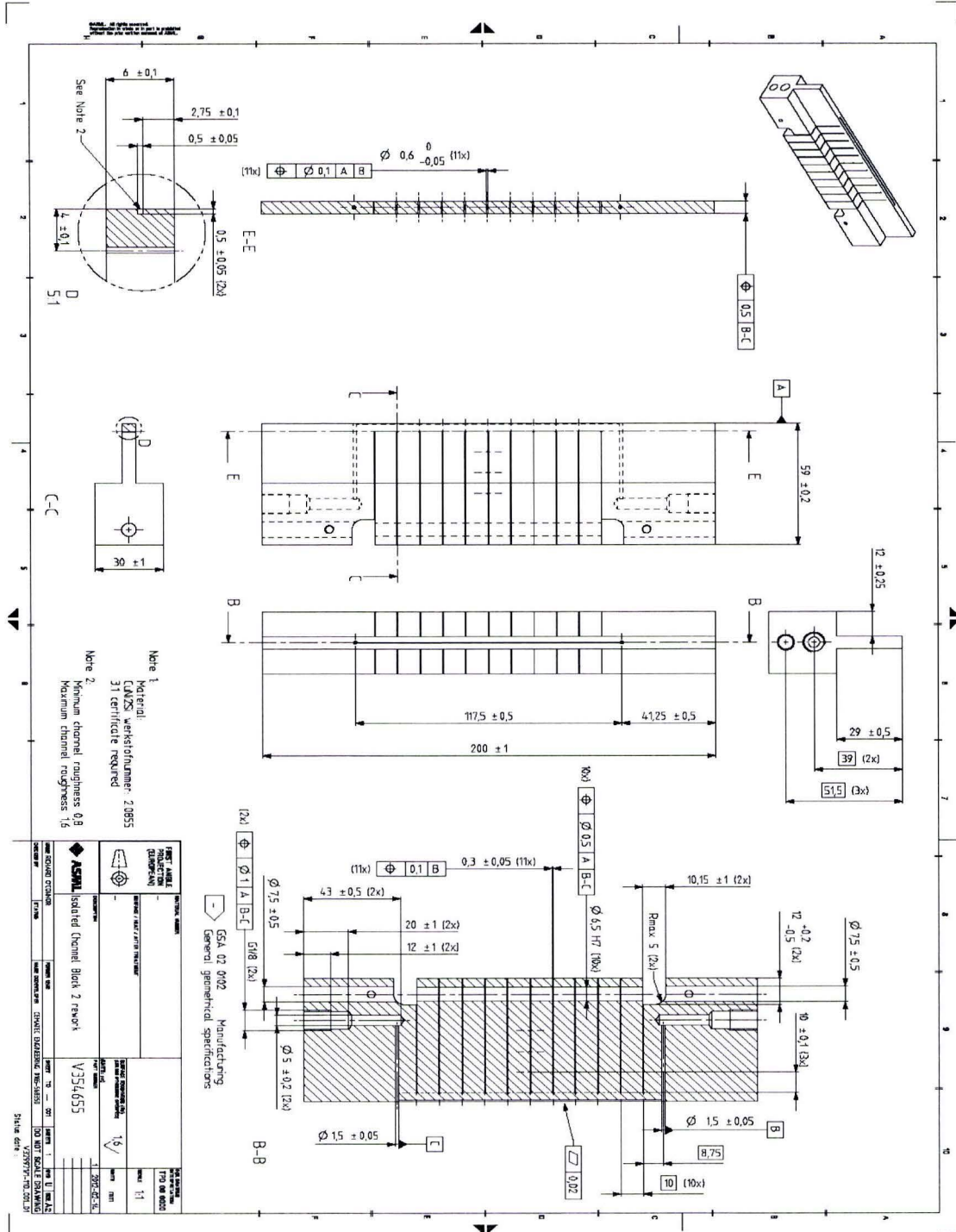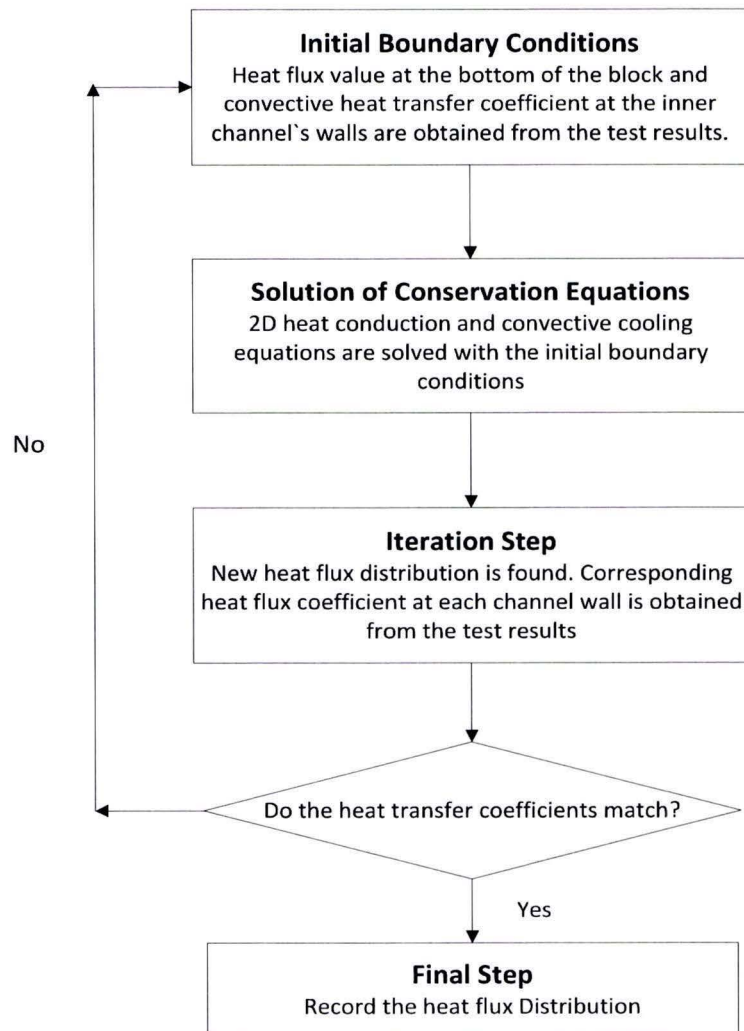
10.7 Surface Roughness Measurements

Surface roughness values multi-channels samples are measured with Sensofar optical image profiler. However, single channels which have the same roughness are used during the tests due to change in the direction of the project. Single channel roughness could not be measured since they were already brazed when the tests had started. For illustration purposes, a magnified image of the channel section and the 3 dimensional surface roughness profile of 1.5 mm multi-channel sample is depicted below:
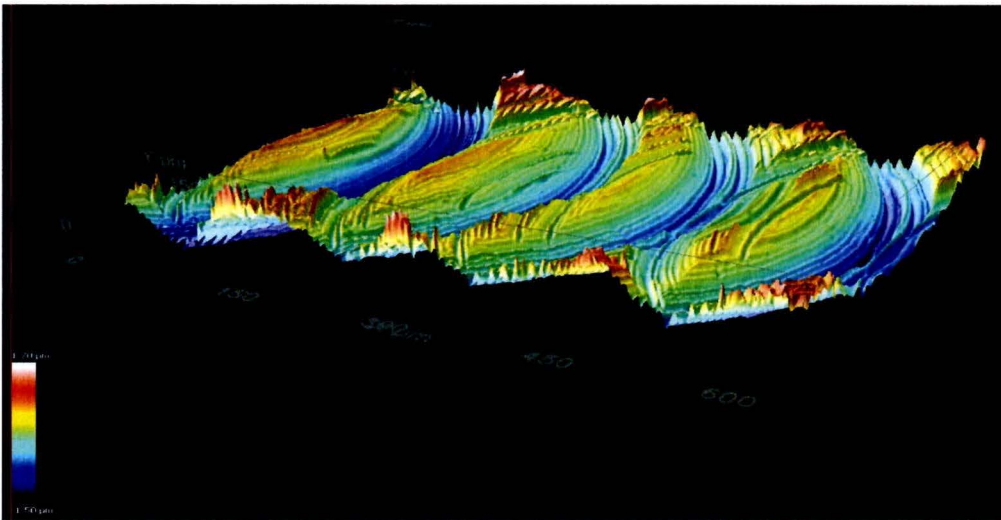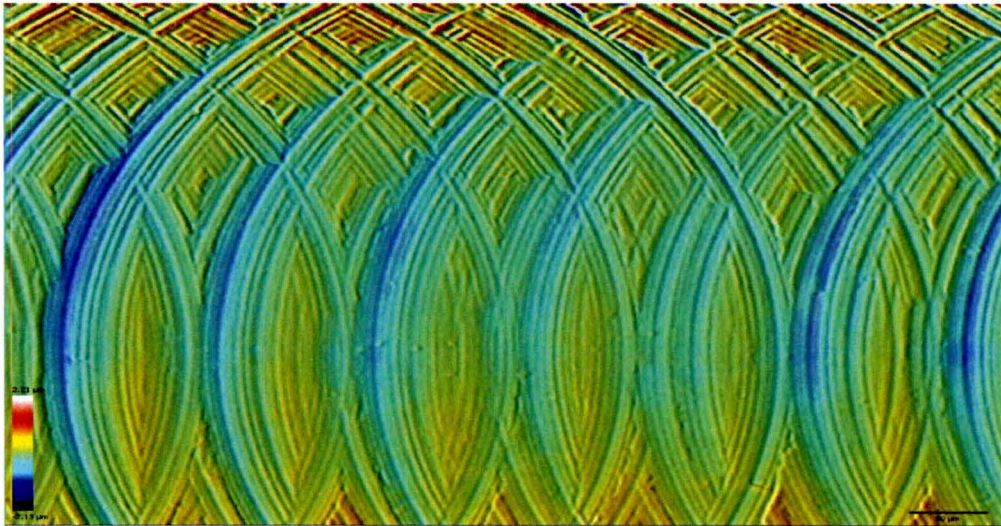
10.15 Surface Roughness Characteristics of 1.5mm Multi-channel Sample with an Arithmetic Roughness of 1.1 μm

10.8 2D Finite Element Analysis of Heat Flux and Temperature Distribution around the 0.5 mm Square Channel Walls

Heat flux distribution around the channel walls is obtained by iterative procedure shown below:

Initial Boundary Conditions
Heat flux value at the bottom of the block and convective heat transfer coefficient at the inner channel`s walls are obtained from the test results.

Solution of Conservation Equations
2D heat conduction and convective cooling equations are solved with the initial boundary conditions

Iteration Step
New heat flux distribution is found. Corresponding heat flux coefficient at each channel wall is obtained from the test results

No

Do the heat transfer coefficents match?

Yes

Final Step
Record the heat flux Distribution

Three iterations are performed to obtain the heat flux distribution shown in Figure 4.3. The results did not change significantly after the second iteration. Due to limited experimental data, new iteration did not performed. Temperature and heat flux distributions are given in Section 10.8.1 and Section 10.8.2.

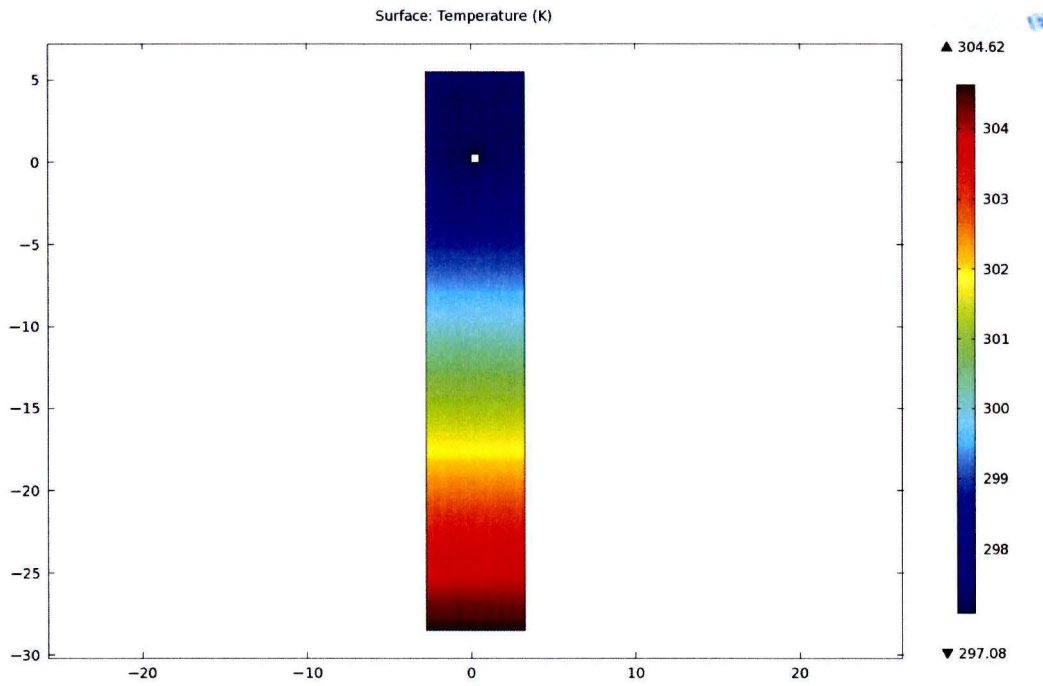## 10.8.1 2D Temperature Distribution

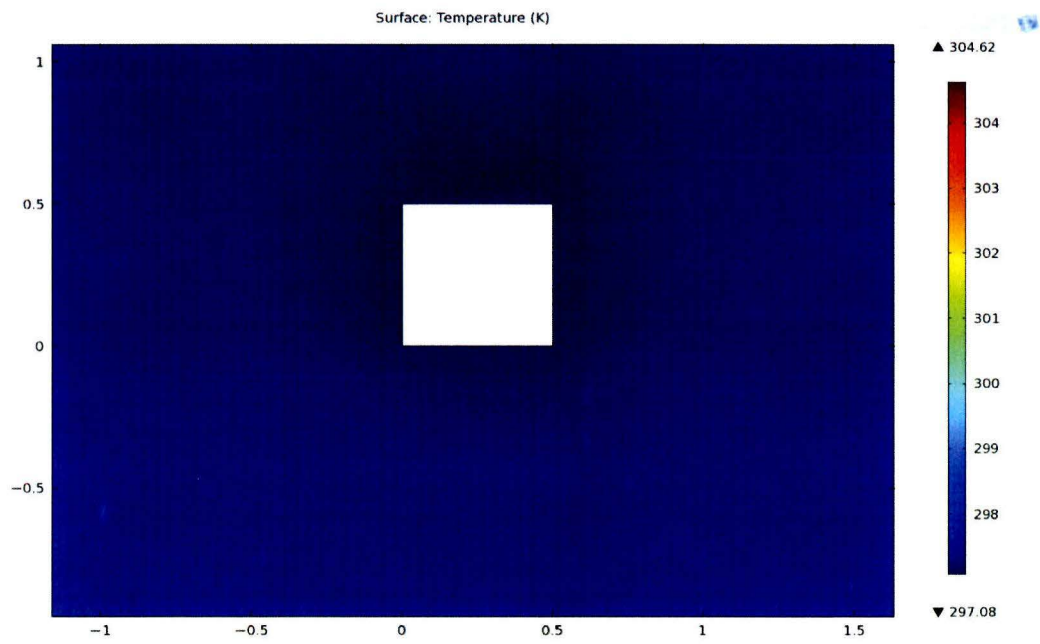**Figure 10.16 2D Temperature Distribution of Upper Part of Channel Block**

Figure 10.17 Zoomed View of Figure 10.16
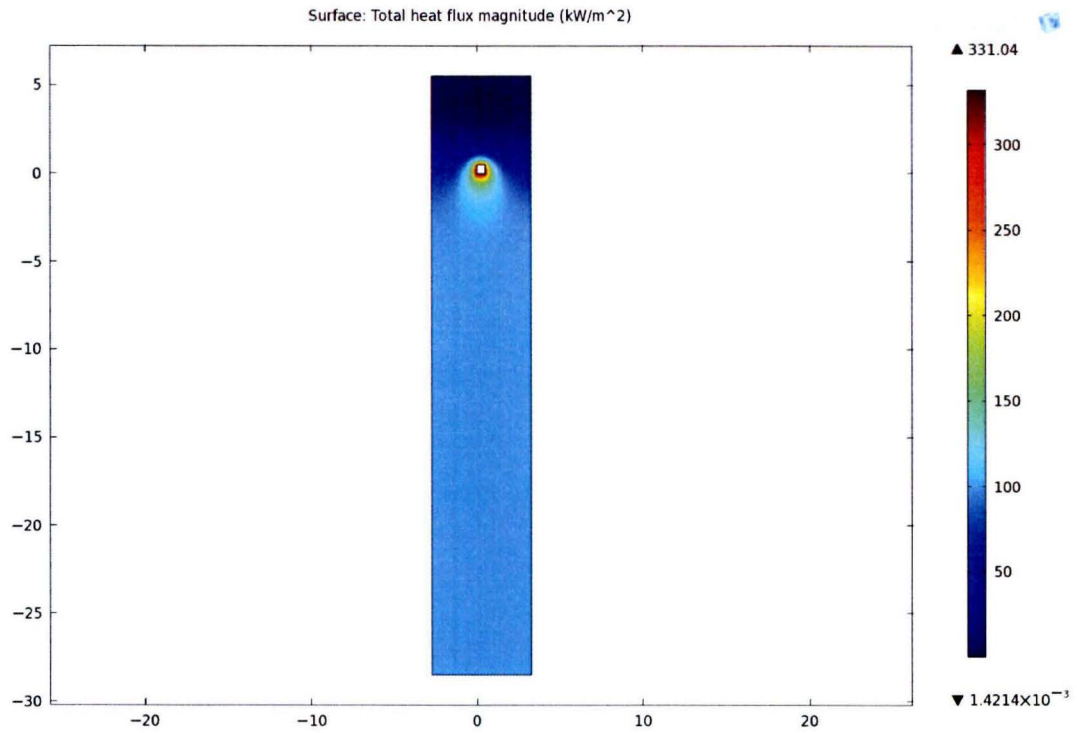
10.8.2 2D Heat Flux Distribution

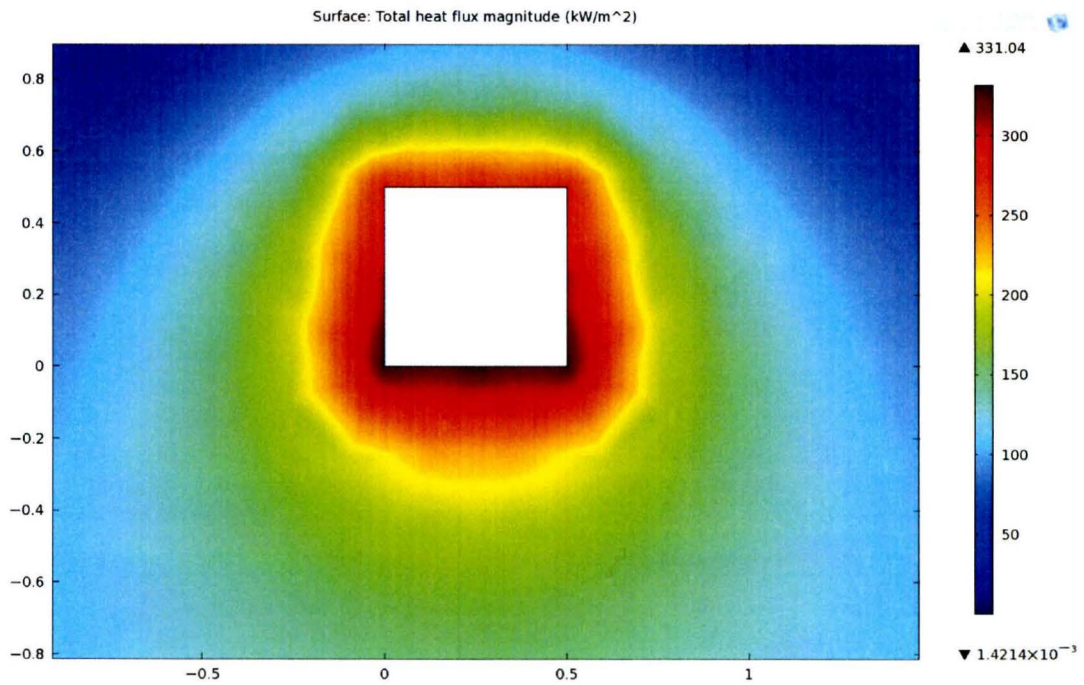**Figure 10.18 2D Heat Flux Distribution of Upper Part of Channel Block**

Figure 10.19 Zoomed View of Figure 10.18

106

10.9 Historical Correlation Development of Cheng et al. [29] Dryout Inception Equation

The dryout correlation that is used to adapt the current database (Equation by Cheng et al. [29], Equation 10.14) originates from the equation by Lavin and Young (1965). After that, Mori et al. [15] observed large deviations compared with their measurements. Then, they defined dryout inception x_{di} and dryout completion x_{de} using three characteristic regimes: $S1, S2$ and $S3$. The best agreement of Wojtan et al. `s [27] experimental data is found with dryout inception and completion equations defined for the regime $S2$. Therefore, here the equation of dryout inception of $S2$ regime is given:

$$x_{di} = 0.58\exp\left[0.52 - 2.1*10^{-5}\mathrm{We}_v^{0.96}\mathrm{Fr}_{v,\mathrm{Mori}}^{-0.02}\left(\frac{\rho_v}{\rho_l}\right)^{-0.08}\right] \tag{10.11}$$

Wojtan, Ursenbacher and Thome [27], modified the Equation 10.11 for their experimental results of R-22 and R410A at evaporation temperatures at 5 °C in 8.0 and 13.84 mm diameter test section for heat fluxes from 17.5 kW/m² up to 57.5 kW/m². The equation of Mori et al. [15] extended by including the heat flux effect using the non-dimensional ratio $\dfrac{q}{q_{\mathrm{crit}}}$ and new empirical factors found based on all experimental points using the least square error method. The new equation is given as:

$$x_{di} = 0.58\exp\left[0.52 - 0.235\mathrm{We}_v^{0.17}\mathrm{Fr}_{v,\mathrm{Mori}}^{0.37}\left(\frac{\rho_v}{\rho_l}\right)^{0.25}\left(\frac{q}{q_{\mathrm{crit}}}\right)^{0.7}\right] \tag{10.12}$$

Cheng, Ribatski, Quiben and Thome [29] adapted Equation 10.12 to fit their CO_2 database. Their database includes tube diameters from 0.6 to 10 mm, mass velocities from 50 to 1500 kg/m²s, heat fluxes from 1.8 to 46 kW/m² and saturation temperatures from -28 to +25 °C. Equation 10.12 remains the same with its non dimensional groups. New empirical factors of Froude number and normalized heat flux terms were obtained since the previous expression did not extrapolate well to reduced pressures far higher than its underlying database. The new equation is given as:

$$x_{di} = 0.58\exp\left[0.52 - 0.236\mathrm{We}_v^{0.17}\mathrm{Fr}_{v,\mathrm{Mori}}^{0.17}\left(\frac{\rho_v}{\rho_l}\right)^{0.25}\left(\frac{q}{q_{\mathrm{crit}}}\right)^{0.27}\right] \tag{10.13}$$

In this study, the coefficients of Froude number and non-dimensional heat flux term have been changed depending on the experimental observations as explained in Chapter 7 and following equation is obtained:

$$x_{di} = 0.58\exp\left[0.52 - 0.236\mathrm{We}_v^{0.17}\mathrm{Fr}_{v,\mathrm{Mori}}^{0.11}\left(\frac{\rho_v}{\rho_l}\right)^{0.25}\left(\frac{q}{q_{\mathrm{crit}}}\right)^{0.70}\right] \tag{10.14}$$